



저작자표시-비영리-변경금지 2.0 대한민국

이용자는 아래의 조건을 따르는 경우에 한하여 자유롭게

- 이 저작물을 복제, 배포, 전송, 전시, 공연 및 방송할 수 있습니다.

다음과 같은 조건을 따라야 합니다:



저작자표시. 귀하는 원저작자를 표시하여야 합니다.



비영리. 귀하는 이 저작물을 영리 목적으로 이용할 수 없습니다.



변경금지. 귀하는 이 저작물을 개작, 변형 또는 가공할 수 없습니다.

- 귀하는, 이 저작물의 재이용이나 배포의 경우, 이 저작물에 적용된 이용허락조건을 명확하게 나타내어야 합니다.
- 저작권자로부터 별도의 허가를 받으면 이러한 조건들은 적용되지 않습니다.

저작권법에 따른 이용자의 권리는 위의 내용에 의하여 영향을 받지 않습니다.

이것은 [이용허락규약\(Legal Code\)](#)을 이해하기 쉽게 요약한 것입니다.

[Disclaimer](#)

Doctor of Philosophy

**NEW FINDING IN FRICTION STIR WELDING (FSW): JOINING
CLAD MATERIAL, LIQUID-REPELLED UNDERSEA FSW, AND
ADHESIVE ASSISTED COMPOSITE MANUFACTURING**



The Graduate School of the University of Ulsan

School of Mechanical Engineering

Soumyabrata Basak

May 2023

**NEW FINDING IN FRICTION STIR WELDING (FSW): JOINING
CLAD MATERIAL, LIQUID-REPELLED UNDERSEA FSW, AND
ADHESIVE ASSISTED COMPOSITE MANUFACTURING**

Supervisor: **Professor Sung-Tae Hong**

A Dissertation

Submitted to the Graduate School of the University of Ulsan

In Partial Fulfillment of the Requirements

for the Degree of

Doctor of Philosophy

by

Soumyabrata Basak

School of Mechanical Engineering

University of Ulsan, Republic of Korea

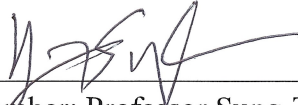
May 2023

**NEW FINDING IN FRICTION STIR WELDING (FSW): JOINING
CLAD MATERIAL, LIQUID-REPELLED UNDERSEA FSW, AND
ADHESIVE ASSISTED COMPOSITE MANUFACTURING**

This certifies that the dissertation of **Soumyabrata Basak** is approved



Committee Chairman: Professor Doo-Man Chun



Committee Member: Professor Sung-Tae Hong



Committee Member: Professor Hoon-Hwe Cho



Committee Member: Dr. Changwook Ji



Committee Member: Professor Jinwoo Lee

School of Mechanical Engineering
University of Ulsan, Republic of Korea

May 2023

Soumyabrata Basak 의

공학박사 학위 논문을 인준함

심사위원

천두만 인



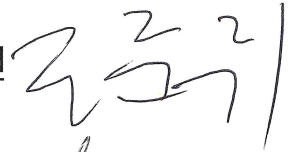
심사위원

홍성태 인



심사위원

조훈휘 인



심사위원

지창욱 인



심사위원

이진우 인



울 산 대 학 교 대 학 원

기계자동차공학과

2023 년 05 월

Dedicated to the research fraternity of solid-state joining and manufacturing

ACKNOWLEDGEMENTS

First, I would like to express my sincere gratitude to my supervisor, Prof. Sung-Tae Hong, for his valuable encouragement and discussions regarding my Ph.D. study and related research. In particular, the conscientious working style has left a deep impression on me and benefited me significantly in my research thinking and activities in the Advanced Engineering Materials (AEM) Laboratory, School of Mechanical Engineering, University of Ulsan.

I particularly wish to thank Prof. Hoon-Hwe Cho and his students at the Hanbat National University for their help and valuable advice on my research. Furthermore, I am pleased to thank the rest of my thesis committee: Dr. Changwook Ji, Prof. Doo-Man Chun, and Prof. Jinwoo Lee, for their insightful comments and encouragement. Also, I would like to acknowledge all my colleagues in the AEM lab for their constant support in my research. I also thank everyone who helped me in one way or another during my Ph.D. period.

Finally, I would like to thank my parents and my wife from the bottom of my heart for their continued encouragement, understanding, and support.

Soumyabrata Basak

Ulsan, Republic of Korea

June 2023

ABSTRACT

With significant demand for greenhouse gas reduction through energy-efficient manufacturing technology, Friction stir welding (FSW), a solid-state joining technology, has been promoted in several aspects of its application. This includes joining advanced light-weight materials, demonstrating its feasibility as an underwater wet welding technique for sub-sea industries, and the ability to produce lightweight metal matrix composites cost-effectively.

In the case of joining advanced material systems, like bi-layer thin clad sheet material, welding is challenging as they are composed of different material layers in a single material system. Fusion welding processes for clad materials often lead to multi-layer delamination and introduce cast microstructures with possible solidification defects. Therefore, the application of FSW to the clad material system will be beneficial to have efficient joint fabrication for advanced vehicles in the automotive industry. Further, material intermixing of the surface cladding layer into the core and the strengthening mechanism of the joint are discussed based on microstructural observation.

Likewise, using FSW as underwater wet welding technique is necessary to avoid the common solidification defects caused by fusion welding processes. However, the most notable of subsequent developments with FSW would be finding a way to divert seawater from the welded region while operating amid the sea. Thus, the newly developed gas pocket-assisted friction stir spot welding (GAFSSW) technique was developed, leading to new ways of reducing or eliminating the absorption of corrosive species (like chlorine) from seawater into the welded area. Furthermore, the quality of the processed region is studied and compared with conventional underwater friction stir spot welding (UFSSW) and FSSW in the air. The current results are consistent with the perspective for the development of UWW technology. This newly developed GAFSSW technique addresses most of the key challenges associated with focused area seawater drainage and solidification defects form in fusion processes.

Producing low-cost light metal matrix composites (MMC) can also be another area of choice where FSW can be applied to improve the efficient green manufacturing of these composites. Several

manufacturing processes have been employed to produce MMC, mainly casting, sintering, powder metallurgy, and other melt-based techniques. However, poor interfacial bonding, reinforcing particle agglomeration, and other common melt defects could be common issues with these traditional processing methods. Hence, friction stir processing (FSP), a solid-state material processing technology developed from the mechanism of FSW, can be an efficient method to produce composite materials. In FSP, tool stirring enables uniform distribution of reinforcements and controls other possible reactions between the matrix and reinforcements to achieve excellent synergy between strength and ductility. Consequently, a detailed study involving the correlation of microstructure and mechanical properties of GO-reinforced AMC prepared by single-pass FSP is much needed to establish this method as an alternative to the existing method.

TABLE OF CONTENT

	Page no.	
ACKNOWLEDGMENTS	i	
ABSTRACT	ii	
TABLE OF CONTENTS	iv	
LIST OF FIGURES	vi	
LIST OF TABLES	xi	
CHAPTER 1	INTRODUCTION	1
1.1	Research motivation	1
1.2	Necessity of this research	3
1.3	Brief introduction of the works	6
	References	8
CHAPTER 2	FRICION STIR LINEAR WELDING OF ALUMINUM-CLAD THIN SHEETS	
2.1	Introduction	11
2.2	Experimental setup	12
2.3	Results and discussion	16
	2.3.1 Process response and optical microscopy	16
	2.3.2 Clad-core intermixing study by EPMA	16
	2.3.3 Precipitation behavior within the SZ by SEM	17
	2.3.4 Microstructural characterization by EBSD	20
	2.3.5 Mechanical properties analysis of the FSW joint	30
2.4	Conclusions	34
	References	35
CHAPTER 3	GAS POCKET-ASSISTED UNDERWATER FRICTION STIR SPOT WELDING	
3.1	Introduction	40
3.2	Materials and experimental procedure	42
3.3	Results and discussions	48
	3.3.1 Process responses and optical microscopy	48
	3.3.2 SEM analysis on the weld top and cross-sections	52
	3.3.3 Microstructural analysis by EBSD	56

	3.3.4 Mechanical properties analysis	61
	3.3.5 Corrosion properties analysis	65
	3.4 Conclusions	70
	References	71
CHAPTER 4	FABRICATION OF ALUMINUM MATRIX COMPOSITES BY FRICTION STIR PROCESSING	
	4.1 Introduction	78
	4.2 Materials and experimental procedures	80
	4.3 Results and discussion	85
	4.3.1 Process responses and optical microscopy	85
	4.3.2 Raman spectroscopy analysis	85
	4.3.3 SIMS analysis on GO survivability in Al matrix	88
	4.3.4 Morphological characterization of GO by TEM	92
	4.3.5 EBSD analysis of the produced AMC	96
	4.3.6 Mechanical properties of the fabricated AMC	102
	4.4 Conclusions	106
	References	107
CHAPTER 5	SUMMARY AND FUTURE WORKS	
	5.1 Research summary	111
	5.2 Future work	115

LIST OF FIGURES

Figure No.	Description	Page No.
1.1	Clad material application in battery electric vehicles (BEV) and the variation of clad material systems possibly used in the automotive industry.	4
1.2	Underwater welding challenges at a glance in present days.	5
2.1	(a) Schematic representation of linear (butt) FSW of Al-clad-Al thin sheets, (b) process parameter optimization of FSW of Al-clad thin sheets.	15
2.2	Force-torque responses during the FSW of Al-clad thin sheets.	18
2.3	(a) Macrograph of the Al-clad Al FSW cross-section. The black rectangles indicate various regions in the BM, TMAZ, and SZ for EBSD, and a white dashed rectangle (A) represents the area for EPMA analysis. (b) Magnified view of the RS of the SZ.	18
2.4	(a) EPMA Si-mapping of the region (A). Magnified images of the sites marked: (b) BM (BT/BB); (c) TMAZ and AS interface; (d-j) various regions of the SZ (R1–R7), respectively.	19
2.5	SEM images of the formation of precipitates in the various regions of the SZ of the Al-clad-Al FSW joint cross-section: (a) the AS (P ₁), (b) middle of the SZ (top, P ₂), (c) the bottom of the SZ (P ₃), and (d) the RS (P ₄).	22
2.6	(a, b) Fe-SEM images of BM (B _T /B _B) and RS of SZ (P ₄) and their corresponding EDS elemental mapping of Al, Si, Mn, and Fe.	23
2.7	Microstructural analysis of Al-clad thin sheet (a-a ₁) BSE image of BM and corresponding EDS line scanning spectrums along the yellow dashed line; EBSD generated (b) IPF map, (c) GBCD map, (d) KAM map, and (e) GOS map of the BM (B _T /B _B).	24

2.8	Microstructural analysis of the TMAZ (AS side) (T) of Al-clad-Al FSW joint using EBSD generated (a) IPF map, (b) GBCD map, (c) KAM map, and (d) GOS map.	27
2.9	BSE images of (a-c) AS (S_1), middle of the SZ (S_2), and RS (S_3) regions of the SZ; (c ₁) corresponding (S_3) element line scanning spectra along the yellow dashed line; EBSD-generated (d-f) IPF maps, and (g-i) GBCD maps for S_1 , S_2 , and S_3 , respectively.	28
2.10	EBSD-generated (a-c) KAM maps, (d-f) GOS maps for the SZ of the Al-clad-Al FSW joint sequentially with AS (S_1), middle of the SZ (S_2), and RS (S_3).	29
2.11	{111} Pole figures acquired from (a) AA4343 (B_T), (b) AA3003 (B_B), (c) TMAZ (T), and (d-f) in the SZ - AS (S_1), middle (S_2), and RS (S_3), respectively for Al-clad-Al FSW joint.	30
2.12	(a) FSW joint cross-section indicating indentation marks under the transparent layer of the microhardness distribution; (b-c) 2D microhardness mapping of the weld cross-section BM to AS and RS to BM; (d) microhardness profile through the mid-thickness of the joint.	31
2.13	(a) Engineering stress vs. engineering strain curves of the BM and the FSW specimen (all-weld) in black (sample fabrication inset); (b) transverse tensile specimen schematic and broken tensile specimen reveals fracture location from the BM.	32
2.14	(a, b) SEM macro-fractography of the broken tensile specimens in the BM and the FSW weld sequentially; (c, d) enlarged views of the regions marked with black rectangles in (a, b).	33
3.1	Schematic view of (a) the tank, (b, c) sample attachment inside the tank for GAFSSW and its actual view with adapter, (d, e) gas tubes attachment with adapter and actual view with its positions, (f) design of the adapter, (g) seawater filling inside the tank, (h, i) final setup of GAFSSW and its actual view represents the entire sample attachment immersed inside the solution.	46

3.2	(a) The complete setup with the tank for GAFSSW, (b) water vortex began initiating gas flow, (c) gas pocket formed and enclosed with the adapter, (d) rotating tool plunged next to the workpiece, (e) tool extracted after welding. The gas pocket was held until the workpiece cooled down, (f) gas flow stopped, and water filled up inside the adapter.	47
3.3	The process parameter optimization ways for GSAFSSW.	48
3.4	(a) Force, (b) torque, (c) temperature profiles for FSSW, UFSSW, and GAFSSW.	50
3.5	Top and bottom surface pictographs of (a, a ₁) FSSW, (b, b ₁) UFSSW, (c, c ₁) GAFSSW.	51
3.6	Optical micrographs of the FSSW, UFSSW, and GAFSSW cross-sections.	51
3.7	SEM image of the top surface of (a) UFSSW, (b) GAFSSW, (c, d) corresponding EDS spectra with elemental compositions.	53
3.8	SEM images of the formation of the precipitate in (a) BM, S ₁ , and S ₂ regions in the SZ of (b, c) FSSW, (d, e) UFSSW, (f, g) GAFSSW.	54
3.9	BSE image of GAFSSW (S ₂) and their corresponding EDS chemical mapping of Mg, Fe, Si, Al, and Mn, respectively.	55
3.10	Microstructure analysis by EBSD generated IPF maps of (a) BM, (b-d) S ₁ , and (b ₁ -d ₁) S ₂ regions: (b-b ₁) FSSW, (c-c ₁) UFSSW, and (d-d ₁) GAFSSW.	58
3.11	Grain boundary characteristics study by EBSD generated GBCD (a-g) and GOS (a ₁ -g ₁) maps: (a-a ₁) BM; (b-b ₁), (d-d ₁), (f-f ₁) for the locations of S ₁ ; (c-c ₁), (e-e ₁), (g-g ₁) for the locations of S ₂ for FSSW, UFSSW, and GAFSSW.	59
3.12	EBSD generated KAM maps of (a) BM, (b-b ₁) S ₁ and S ₂ regions of FSSW, (c-c ₁) for UFSSW, and (d-d ₁) for GAFSSW.	60
3.13	(a) Schematic micrograph of the weld cross-section indicating the location for microhardness measurements, 2D surface microhardness map for (b) FSSW, (c) UFSSW, and (d) GAFSSW weld cross-sections.	63

3.14	(a) Schematic micrograph of the weld cross section indicating the locations for indentation tests, L - H curves, and stress-strain curves for (b, c) S ₁ and (d, e) S ₂ locations obtained from the SZ of FSSW, UFSSW, and GAFSSW weld cross sections.	64
3.15	(a) OCP curves concerning time and (b) electrochemical potentiodynamic polarization curves of the tested samples, (c) avg. E _{corr} vs. CR plot, data obtained from potentiodynamic polarization curves of BM, FSSW, UFSSW, and GAFSSW.	68
3.16	Schematic representation of GAFSSW operation in the sea (a) Step - 1: FSW-BOT set up, (b) Step - 2: welding with the gas pocket on the desired location of the workpiece.	69
4.1	(a) Schematic of AMC fabrication using FSP, (b) SEM image of GO particles, (c) a detailed picture of the fabricated AMC.	84
4.2	(a) Axial force distribution, (b) temperature curves obtained during FSP-only and FSP with GO conditions.	86
4.3	OM macrographs of the cross-sections of (a) FSP-only and (b) FSP with GO conditions.	87
4.4	Raman spectrums of (a) GO, (b) AS, and (c) RS of FSP with GO and FSP-only SZ.	88
4.5	(a) Schematic of SIMS location, (b) Al and C depth profiles.	89
4.6	Microprobe Cs ⁺ scanning beam induced total ion imaging of C in (a, b) FSP-only and (c, d) FSP with GO SZ. (e) SEM image on the SIMS site, (f) magnified SEM images from the mark locations (yellow), (g) EDS live chemical imaging of Al and C.	90
4.7	(a) Tilted view of GO at SIMS site under FIB-SEM, (b) Sample extraction (black arrow) using both sides of FIB, (c) SEM image of the extracted sample, (d) magnified image of the marked location (blue dotted rectangle) in Fig. (c), (e) sample prepared for TEM analysis.	91
4.8	(a) TEM micrograph of the entire specimen focused for analysis, (b, c) magnified TEM images of Zone 1 and Zone 2, high-resolution TEM (HR-TEM) images of (d) GO	93

	reinforcement, (e) Al matrix, and (f) interface between GO and Al.	
4.9	HAADF STEM image on the specimen and corresponding EDS elemental area mapping of Al, C, N, O, S, Pt, and W, respectively.	94
4.10	(a) line scanning spectra show the elemental profile of the present trace elements with Al and C, (b) Magnified view of the line scanning spectra C has a slightly higher concentration value among other elements present in GO.	95
4.11	Microstructural analysis of AA1050 (BM) (a) IPF map, (b) KAM map, (c) GBCD map, and (d) GOS map, respectively.	99
4.12	EBSD analysis on the SZ AS (S_1); IPF, KAM, GBCD, GOS maps for (a-d) FSP-only and (e-h) FSP with GO conditions.	100
4.13	EBSD analysis on the RS (S_2) of the SZ; IPF, KAM, GBCD, GOS maps for (a-d) FSP-only and (e-h) FSP with GO conditions.	101
4.14	Microtexture analysis by $\{111\}$ pole figures (a) BM; AS (S_1) and RS (S_2) of the SZs of (b, d) only FSP and (c, e) FSP with GO conditions.	102
4.15	Microhardness mapping of (a) FSP-only and (b) FSP with GO conditions.	104
4.16	(a) Tensile tests curves of BM (in black color), FSP-only (in red color), and FSP with GO (in blue color) specimen merged, (b-d) Fractography of the fractured tensile specimen for BM, FSP-only, and FSP with GO, respectively.	105
5.1	Photographic representation of the summary of Chapter 2.	112
5.2	Photographic representation of the summary of Chapter 3.	113
5.3	Photographic representation of the summary of Chapter 4.	114

LIST OF TABLES

Table No.	Description	Page No.
2.1	Chemical compositions of the BM (wt.%)	14
2.2	Possible elemental compositions (at.%) of various precipitates	22
2.3	Mechanical properties of the BM and FSW joint	33
3.1	Chemical compositions of AA5083-H112 (wt.%)	42
3.2	Optimized weld parameters	44
3.3	Measured dimension of the welding region (spots)	49
3.4	Possible compositions of precipitates (at.%)	52
3.5	Corrosion parameters obtained from the polarization curves	66
4.1	Chemical compositions of AA1050-H14 (wt.%)	80
4.2	FSP parameters	81
4.3	Measured data obtained from the tensile curves	104

CHAPTER I

INTRODUCTION

1.1 RESEARCH MOTIVATION

There is a growing interest in solid-state manufacturing technology because of its excellent capabilities of joining and forming a wide range of structural materials, including ferrous/non-ferrous alloys, advanced material systems, and composites [1,2]. The leading advantage of using solid-state technologies over fusion techniques is the non-radiative, energy-efficient, clean fabrication of structural components for industrial applications [3]. The traditional fusion welding or fabrication techniques, including gas-metal arc welding, tungsten inert gas welding, metal inert gas welding, and flux-coated arc welding, involve a significant amount of toxic fumes, arc radiation, molten spatter that usually pollute environments as well as affect safety for workers [3]. In contrast, the processing temperature for solid-state welding and processing is always below the melting temperature of the substrate, which also helps mitigate the most common fusion defects, like porosity, pinholes, and hot cracking [4,5]. Therefore, the absence of molten metal and almost no filler/flux materials make solid-state manufacturing technology more acceptable as a greener process for bulk metallic structure fabrication in various sectors, including energy, automotive, and aerospace industries [5].

Out of many solid-state manufacturing technologies, friction stir welding (FSW) is one of the versatile joining technology invented at the welding institute (TWI) in 1991 [5]. As a deformation-based solid-state joining technology, FSW became a primary interest because of its unique processing mechanism, which includes a substantial amount of heating with material flow-induced significant plastic deformation inside the target materials [6]. In FSW, a non-consumable

rotating tool entailing a pin and shoulder plunges inside the materials. It travels through the mating surfaces of the substrate, accomplishing metallurgical bonding by frictional heat. The rotating tool pin primarily causes material stirring and mixing with localized heating, whether the larger extent of frictional heat comes from the tool shoulder interaction with the substrate materials and causes a significant amount of material flow during FSW [4-6]. Initially, the tool pin plunges inside the material to reach the desired penetration depth (based on material thickness), and the tool shoulder comes in contact with the workpiece material. After sufficient heat generation, the workpiece material becomes plasticized, and the tool moves toward the desired joining (linear) direction. The advantage of FSW over the other solid-state joining technologies is that it can be applied to various joint configurations, including butt, lap, spot, T-Butt, etc., at similar and dissimilar material combinations. At the initial stage of this process invention, FSW was limited to making an efficient joint in heat-treatable aluminum alloys, which were shown to have poor weldability under fusion joining processes [5-9]. Despite having defects-free joining capabilities of FSW, one of the significant benefits of using this technology is to achieve a dynamically recrystallized fine grain structure formed inside the weld region (typically called stir zone), further helping to develop the mechanical properties of the weldment effectively [6]. Li et al. [10] successfully performed dissimilar FSW between 2024/6061 aluminum alloys with the formation of fine grains microstructure without any defects inside the weld joint. Mishra et al. [11] executed friction stir processing (FSP), a similar processing technology on the surface of the substrate materials, adopted from the FSW. They demonstrated the feasibility of FSP in microstructural changes with high strain rate superplasticity in a commercial aluminum alloy.

1.2 NECESSITY OF THIS RESEARCH

The most significant advancement related to FSW was the development of various tools and their impact on the material flow behavior allied with the microstructure and mechanical behavior of the joint. Mishra et al. [5] thoroughly revealed the use of various types of tools in terms of their designs and the tool fabrication materials, which made FSW acceptable in a more extensive research span and developments with other ferrous and non-ferrous structural materials, apart from aluminum (Al) alloys. There are many published articles available on the feasibility of performing FSW on various grades of structural materials, including steels [12], copper (Cu) alloys [13], titanium (Ti) alloys [14], magnesium (Mg) alloys [15], Inconel [16], and other kinds of structural materials, like composites [17]. Hence, the improved reliability and repeatability of joining on various grades of structural materials made FSW one of the most famous trends in welding technology with broad applications in various industrial sectors.

In the case of the automotive industry, lightweight advanced new-energy vehicle production has recently gained much greater attention for energy-efficient transportation. Unfortunately, lightweight monolithic materials, like Al, Mg alloys, and other advanced steels, sometimes do not fulfill the automotive industry requirements, which increasingly demands new-age materials suitable for various functions [4,6]. The clad material system is one of the highly recommended advanced materials for energy vehicles, in which clad and core materials have different properties, while the whole material system acts as a single material [6]. Figure 1.1 shows the application of clad materials in battery electric vehicles and the various possible clad material systems applicable to the automotive industry. However, this advanced material joining is still challenging due to its laminated structures and different material combinations. A few trials with conventional fusion welding techniques on clad material systems showed delamination of the clad

layer to core, clad layer melts, sticking with the electrode (for resistance spot welding), and solidification defects [18-20]. This is where the importance of FSW of a clad material system is found more significant.

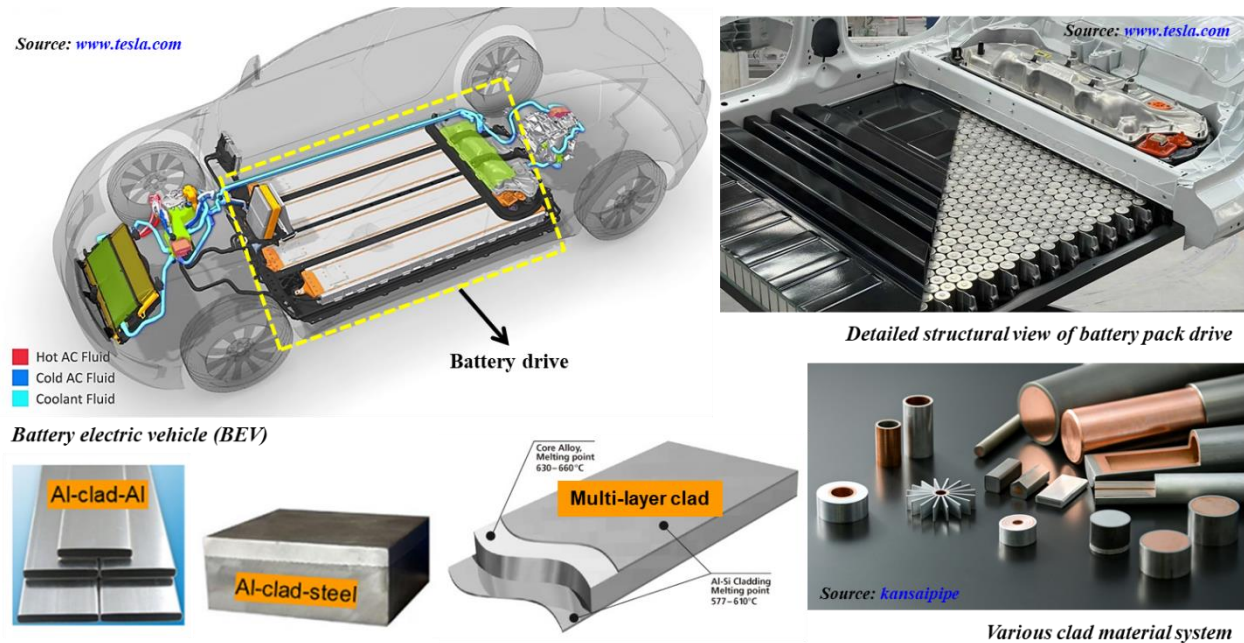
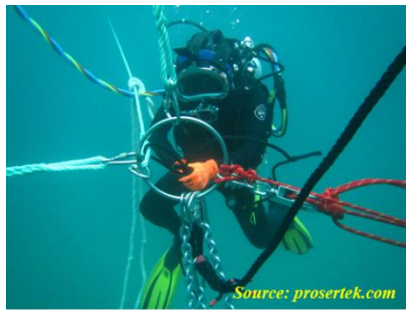


Fig. 1.1 Clad material application in battery electric vehicles (BEV) and the various clad materials available for automotive sectors.

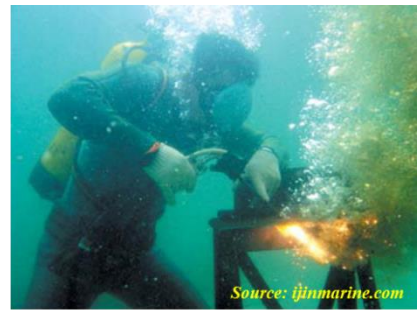
In the case of the subsea industry, welding is considered the most used manufacturing process due to the installation of bulk metallic structures and their continuous maintenance activities. Most structures in subsea industries, including offshore structures and crude oil and gas drilling equipment, are usually built in the sea, ranging from a warm marine to an arctic environment [21-23]. Therefore, underwater wet welding (UWW) is the most fundamental technique for subsea industries. The conventional underwater fusion welding techniques are cheaper but very risky in terms of welder safety as well as material properties degradation [24,25].



Depth of dive: welder safety



Risky diver position: hazardous



Generation of harmful smoke



Ignition and explosions



Unresponsive welder, Accident



In the deep sea no one can hear you

Fig. 1.2 Underwater welding challenges at a glance in present days.

Hence, subsea industries need a profound change in welding techniques for their structures and regular trouble-free operations beneath the sea. Figure 1.2 shows the challenges associated with conventional underwater fusion welding present days. Also, another significant drawback for UWW is the contamination of corrosive species inside the weld, as seawater comes directly and covers the desired weld area inside the sea. This is where research strongly requires more attention in using solid-state welding technique; FSW to replace and avoid hazardous environments and give a better life to the underwater welded. Also, the most influential research could be using FSW and removing seawater from the weld area to have a safer and good quality joint interface in subsea industries.

Another impact of doing research with FSW is the successful generation of cost-effective metal matrix composites (MMC) by FSP. This process is most beneficial in achieving desired reinforcement particle distribution and has less chance of having intermetallics formation between the base material and reinforcements, unlike the conventional fusion or cast techniques [26]. However, fabricating MMC using FSP requires further research introducing reinforcing nanoparticles into the base material. The present method associated with MMC is to make slots or drill holes in the materials and fill up the slots with reinforcing materials. But, this requires additional stages in manufacturing MMC, which consumes extra energy, time, and cost [26-28]. Hence, a new method of introducing particles in the base material before FSP still requires significant research for the cost-efficient fabrication of green composites.

1.3 BRIEF INTRODUCTION OF THE WORKS

In this work, FSW and FSP are used for welding advanced lightweight materials and cost-effective aluminum matrix composites (AMC) fabrications in targets with various industrial sectors. The thesis is divided into three chapters as three different works. Each chapter describes different applications of the material used and discusses in detail the effectiveness of the FSW through microstructural changes in relation to the mechanical properties of the joint.

Chapter 2 represents an experimental investigation of FSW of thin Al-clad-Al sheets. The microstructural changes associated with the material flow and intermixing of the clad layer to the core material are analyzed. Furthermore, the impact of microstructural changes on the mechanical properties developments of the joint is demonstrated. No such delamination of the material structure is found at the weld interface.

A newly developed gas pocket-assisted underwater friction stir spot welding (GA-FSSW) is reported in Chapter 3. This technique is evaluated in view of the necessity of subsea industries and the required modification with UWW. An inert gas pocket helps to drain the seawater from the weld area, which further benefits from removing Cl contamination from the material surface, as anticipated from the scanning electron microscopy linked with energy dispersive spectroscopy (SEM/EDS) analysis. Based on the thermal cycle of this newly developed GA-FSSW technique, microstructural changes related to the evolution of the mechanical properties of the weld are also investigated.

Chapter 4 describes a unique way of introducing reinforcing elements on the pure Al surface to fabricate AMC using FSP. Graphene oxide (GO) particles are pasted using adhesives onto the pure Al surface and dried prior to FSP. This meaningfully avoids additional manufacturing stages, which is the primary interest of this research. The presence of GO in the Al matrix and its morphology are expressively studied by using several advanced characterization techniques, including secondary ion mass spectrometry (SIMS), transmission electron microscopy (TEM), SEM, and EBSD microstructures. As a result of the microstructural changes, the mechanical strength of the composites is improved than the base material and only FSP conditions.

REFERENCES

1. J.J. Lopez, M.B. Williams, T.W. Rushing, M.P. Confer, A. Ghosh, C.S. Griggs, J.B. Jordon, G.B. Thompson, P.G. Allison, A solid-state additive manufacturing method for aluminum-graphene nanoplatelet composites, *Materialia* 23 (2022) 101440. <https://doi.org/10.1016/j.mtla.2022.101440>
2. H. Lalvani, P. Mandal, A.Yaghi, P. Santos, B. Baufeld, A solid-state joining approach to manufacture of transition joints for high integrity applications, *J. Manuf. Process.* 73 (2022) 90-111. <https://doi.org/10.1016/j.jmapro.2021.10.058>
3. P. Kah, R. Rajan, J. Martikainen, R. Suoranta, Investigation of weld defects in friction-stir welding and fusion welding of aluminium alloys, *Int. J. Mech. Mater. Eng.* 10 (2015) 26. <https://doi.org/10.1186/s40712-015-0053-8>
4. K. Gao, S. Basak, M. Mondal, S. Zhang, S.T. Hong, S.Y. Boakye, H.H. Cho, Friction stir welding of AA3003-clad AA6013 thin sheets: Microstructural changes related to tensile properties and fatigue failure mechanism, *J. Mater. Res. Technol.* 17 (2022) 3221-3233. <https://doi.org/10.1016/j.jmrt.2022.02.073>
5. R.S. Mishra, Z.Y. Ma, Friction stir welding and processing, *Mater. Sci. Eng. R Rep.* 50 (2005) 1-78. <https://doi.org/10.1016/j.mser.2005.07.001>
6. S. Basak, M. Mondal, K. Gao, S.T. Hong, S.Y. Anaman, H.H. Cho, Friction stir butt-welding of roll clad aluminum thin sheets: effect of microstructural and texture changes on mechanical properties, *Mater. Sci. Eng. A* 832 (2022) 142490. <https://doi.org/10.1016/j.msea.2021.142490>
7. J.Q. Su, T.W. Nelson, R. Mishra, M. Mahoney, Microstructural investigation of friction stir welded 7050-T651 aluminium, *Acta Mater.* 51 (3) (2003) 713 – 729. [https://doi.org/10.1016/S1359-6454\(02\)00449-4](https://doi.org/10.1016/S1359-6454(02)00449-4)
8. T. Miyamori, Y. Sato, H. Kokawa, Influence of underwater operation on friction stir welding of medium carbon steel, In: Y. Hovanski, R. Mishra, Y. Sato, P. Upadhyay, D. Yan (eds.) *Friction Stir Welding and Processing IX* (2017). The Minerals, Metals & Materials Series. Springer, Cham. https://doi.org/10.1007/978-3-319-52383-5_3
9. P.S De, R.S. Mishra, Microstructural evolution during fatigue of ultrafine grained aluminum alloy, *Mater. Sci. Eng. A* 527 (2010) 7719 – 7730. <https://doi.org/10.1016/j.msea.2010.08.047>
10. Y. Li, L.E. Murr, J.C. McClure, Flow visualization and residual microstructures associated with the friction-stir welding of 2024 aluminum to 6061 aluminum, *Mater. Sci. Eng. A* 271 (1999) 213-223. [https://doi.org/10.1016/S0921-5093\(99\)00204-X](https://doi.org/10.1016/S0921-5093(99)00204-X)

11. R.S. Mishra, M.W. Mahoney, S.X. McFadden, N.A. Mara, A.K. Mukherjee, High strain rate superplasticity in a friction stir processed 7075 Al alloy, *Scr. Mater.* 42 (1999) 163-168. [https://doi.org/10.1016/S1359-6462\(99\)00329-2](https://doi.org/10.1016/S1359-6462(99)00329-2)
12. W.M. Thomas, P.L. Threadgill, E.D. Nicholas, Feasibility of friction stir welding steel, *Sci. Technol. Weld. Join.* 4 (1999) 365-372. <https://doi.org/10.1179/136217199101538012>
13. W.B. Lee, S.B. Jung, The joint properties of copper by friction stir welding, *Mater. Lett.* 58 (2004) 1041-1046. <https://doi.org/10.1016/j.matlet.2003.08.014>
14. H.J. Liu, L. Zhou, Q.W. Liu, Microstructural evolution mechanism of hydrogenated Ti-6Al-4V in the friction stir welding and post-weld dehydrogenation process, *Scr. Mater.* 61 (2009) 1008-1011. <https://doi.org/10.1016/j.scriptamat.2009.08.012>
15. W.B. Lee, Y.M. Yeon, S.B. Jung, Joint properties of friction stir welded AZ31B- H24 magnesium alloy, *Mater. Sci. Technol.* 19 (2003) 785-790. <https://doi.org/10.1179/026708303225001867>
16. H. Das, M. Mondal, S.T. Hong, J.W. Lee, H.H. Cho, Texture and precipitation behavior of friction stir welded Inconel 825 alloy, *Mater. Today Commun.* 25 (2020) 101295. <https://doi.org/10.1016/j.mtcomm.2020.101295>
17. R.A. Prado, L.E. Murr, D.J. Shindo, K.F. Soto, Tool wear in the friction-stir welding of aluminum alloy 6061+20% Al₂O₃: a preliminary study, *Scr. Mater.* 45 (2001) 75-80. [https://doi.org/10.1016/S1359-6462\(01\)00994-0](https://doi.org/10.1016/S1359-6462(01)00994-0)
18. J. Fallu, H. Izadi, A.P Gerlich, Friction stir welding of co-cast aluminium clad sheet, *Sci. Technol. Weld. Join.* 19 (1) (2014) 9-14. <https://doi.org/10.1179/1362171813Y.00000000155>
19. Hasanniah, M. Movahedi, Welding of Al-Mg aluminium alloy to aluminium clad steel sheet using pulsed gas tungsten arc process, *J. Manuf. Process.* 31 (2018) 494-501. <https://doi.org/10.1016/j.jmapro.2017.12.008>
20. S.P. Murugan, M. Cheepu, V. Vijayan, C. Ji, Y.D. Park, The resistance spot weldability of a stainless steel/aluminium/low carbon steel 3-ply clad sheet, *J. Weld. Join.* 36 (1) (2018) 25-33. <https://doi.org/10.5781/JWJ.2018.36.1.3>
21. J. Tomków, D. Fydrych, G. Rogalski, Dissimilar underwater wet welding of HSLA steels, *Int. J. Adv. Manuf. Technol.* 109 (2020) 717-725. <https://doi.org/10.1007/s00170-020-05617-y>

22. J. Łabanowski, Development of under-water welding techniques, *Weld. Int.* 25 (2011) 933-937. <https://doi.org/10.1080/09507116.2010.540847>
23. K.R. Carpenter, P. Dissanayaka, Z. Sterjovski, H. Li, J. Donato, A.A. Gazder, S.V. Duin, D.Miller, M. Johansson, The effects of multiple repair welds on a quenched and tempered steel for naval vessels, *Weld. World* 65 (2021) 1997–2012. <https://doi.org/10.1007/s40194-021-01150-y>
24. C. Xing, C. Jia, Y. Han, S. Dong, J. Yang, C. Wu, Numerical analysis of the metal transfer and welding arc behaviors in Underwater Flux-cored Arc Welding, *Int. J. Heat Mass Transf.* 153 (2020) 119570. <https://doi.org/10.1016/j.ijheatmasstransfer.2020.119570>
25. J. Tomków, D. Fydrych, K. Wilk, Effect of electrode waterproof coating on quality of underwater wet welded joints, *Materials* 13 (2020) 2947. <https://doi.org/10.3390/ma13132947>
26. S. Dixit, A. Mahata, D.R. Mahapatra, SV Kailas, K. Chattopadhyay, Multi-layer graphene reinforced aluminum – Manufacturing of high strength composite by friction stir alloying, *Compos. Pt. B. Eng.* 136 (2018) 63-71. <https://doi.org/10.1016/j.compositesb.2017.10.028>
27. A. Sharma, H. Fuji, J. Paul, Influence of reinforcement incorporation approach on mechanical and tribological properties of AA6061- CNT nanocomposite fabricated via FSP, *J. Manuf. Process.* 59 (2020) 604-620. <https://doi.org/10.1016/j.jmapro.2020.10.016>
28. H. Zhang, B. Zhang, Q. Gao, J. Song, G. Han, A review on microstructures and properties of graphene-reinforced aluminum matrix composites fabricated by friction stir processing, *J. Manuf. Process.* 68 (2021) 126-135. <https://doi.org/10.1016/j.jmapro.2021.07.023>

CHAPTER II

FRICITION STIR LINEAR WELDING OF ALUMINUM-CLAD THIN SHEETS

2.1 INTRODUCTION

The significant demand for greenhouse gas reduction through energy-efficient transportation is devoting the automotive industries to the development of New Energy Vehicles (NEVs) [1]. Out of many components used in NEVs, the total battery drive accounts for up to 30% of the total weight of battery electric vehicles (BEVs) [2]. Thus, weight reduction of the battery drive significantly improves BEV performance. Therefore, the automotive industry is increasingly demanding advanced material systems to perform wide-ranging functions, as monolithic materials fail to meet the current needs of various sectors of this industry [3]. Accordingly, clad material systems have become of primary interest due to their dissimilar properties between the cladding and the core over monolithic alloys [4]. Roll cladding is generally more competent than other cladding methods as it reduces material thickness, uniformity of individual layers, superior surface quality, and ease of manufacture of the flat sheet in large quantities without using filler materials [5]. Roll cladding of lightweight materials is generally performed by removing the surface impurities and achieving a metallurgical bond between the cladding layers and the core materials under a certain pressure and temperature, which goes through several subsequent stages before commercialization [6,7].

The manufacturing of a large-volume metallic structure always includes materials joining. However, joining the clad sheets using fusion welding leads to the delamination of multilayers and the formation of cast microstructure as the temperature ranges similar to the melting points of the

materials [8]. Movahedi et al. [9] examined the welding of Al/Al-clad-steel sheets by a pulsed-gas-tungsten arc process. They observed dendritic microstructure inside the weld nugget, which further caused the degradation of various material properties. Murugan et al. [10] found columnar dendritic grain growth within the weld area of stainless-steel/Al/low-carbon steel clad materials performed by resistance spot welding. They also found that the liquid copper (electrode material) penetrated inside the weld region while the sheets wedged between the electrodes.

Being a solid-state joining process, Friction stir welding (FSW) is a reasonable substitute for fusion techniques, as this process can efficiently control the material flow within the joining region and avoids solidification defects [8,11-15]. Although, the joining of clad sheets was not easy too by FSW, as found in the earlier reports by several researchers. Gerlich et al. [8] performed FSW of co-cast Al-clad sheets and claimed no such delamination of the clad materials. But, the mechanical strength of the joint was found to be less than the base material. Xiao et al. [16] executed FSW of Al-clad-AA2024 to Al2009/SiC composite sheets. They reported that the cladding layer was displaced from the edge of AA2024.

Although many studies on joining clad sheets by FSW have been reported, further research on this topic should still be beneficial due to the extensive groupings of clad/core materials depending on the target applications. This work executes FSW (butt configuration) of thin Al-clad-Al sheets and examines material flow behavior from cladding to core materials. In addition, the microstructural changes in the strengthening mechanism of joints are discussed.

2.2 EXPERIMENTAL SET-UP

Two non-heat-treatable Al alloys, AA4343 (B_T) and AA3003 (B_B) (Table 2.1), act as the clad layer and core material and are considered the base material (BM; thickness 1.5 mm) in this

study. This arrangement ensured a proper grouping between the easily formable, thermally conductive, lightweight B_B with the corrosion-resistant, ductile B_T [13,17-19].

The AA 2-ply clad sheet was machined into 150 mm length and 100 mm width for FSW. The positions of the clad sheets and the FSW process are schematically described in Fig. 2.1(a). The butt joint along the length of the clad sheets was performed at 600 rpm tool rotation speed with 100 mm/min weld speed using a custom-built FSW machine (RM-1, TTI, USA). An H-13 steel-made tool with a 10 mm concave shoulder coupled with a 3 mm cylindrical threaded pin was used in this study. A tool tilt angle of 1.35° was considered to provide an additional backward thrust at the bottom part of the plates during FSW, which further helped to avoid wormhole formation and other defects within the joining area. An embedded data acquisition system was used to record the process responses during joining. The process parameter was optimized based on the separately conducted tensile tests of various joints fabricated with varying tool rotations and weld speeds, as shown in Fig. 2.1(b). The parameter was given higher strength than the others, and the BM was considered the optimized parameter for detailed analysis, such as microstructural changes associated with the development of mechanical properties of the joint.

After FSW, the joint cross-section was prepared for optical microscopy (GX41, Olympus, Japan) through simultaneous grinding, polishing, and etching with Keller's reagent. The distribution of Si particles and the material flow from clad to core materials was precisely examined using an electron probe micro analyzer (EPMA-1610, SHIMADZU, Japan). A Fe-SEM (JSM7600F, Jeol, Japan) equipped with a dispersive energy X-ray (EDX; X-Max50, Horiba, Japan) was used to study the presence of precipitates within the SZ. Another Fe-SEM (SU5000, Hitachi, Japan) equipped with an electron backscatter diffractometer (EBSD; TSL Hikari Super, TSL, USA) was used to capture backscattered electron (BSE) images and EBSD microstructures from the

selected location in the joint cross-section. Prior to this, the specimen was polished to 0.25 μm diamond paste, followed by colloidal silica polishing to obtain a scratch-free mirror-like surface. To understand the microstructural changes in the SZ, various EBSD-generated maps, including inverse pole figure (IPF), grain boundary character distribution (GBCD), kernel average misorientation (KAM), grain orientation spread (GOS) maps, were obtained. Pole figures (PF) were also considered for micro-texture analysis and mapped based on the ideal $\{111\}$ crystallographic shear plane and $\langle 110 \rangle$ crystallographic shear direction for FCC materials [20].

2-D surface hardness mapping on the joint cross-section was performed in four layers of 250 indents, taken using a load of 0.50 N for 10 seconds. An automatic Vickers microhardness tester (HM -100, Mitutoyo, Japan) was used for this measurement. A Vickers indenter (HM -100, Mitutoyo, Japan) was also used to measure the hardness profile through the middle region of the weld cross-section. A sub-size tensile specimen was made along the joining direction according to the ASTM standard [21] to measure the tensile strength of the joint. The tensile testing was performed using a universal testing machine (DTU900-MH, Daekyoung, South Korea) with a cross-head speed of 1 mm/min until the specimen was fractured. The failure mechanism of this specimen was further analyzed by putting the fracture surfaces under FE-SEM. The cross-tensile specimen was similarly fabricated and tested to confirm the effectiveness of the joining.

Table 2.1 Chemical compositions of the BM (wt.%)

Materials	Si	Fe	Cu	Mn	Mg	Zn	Ti	Al
AA 3003	0.33	0.54	0.14	1.11	0.01	0.02	0.004	Balance
AA 4343	7.23	0.33	-	-	-	-	0.020	Balance

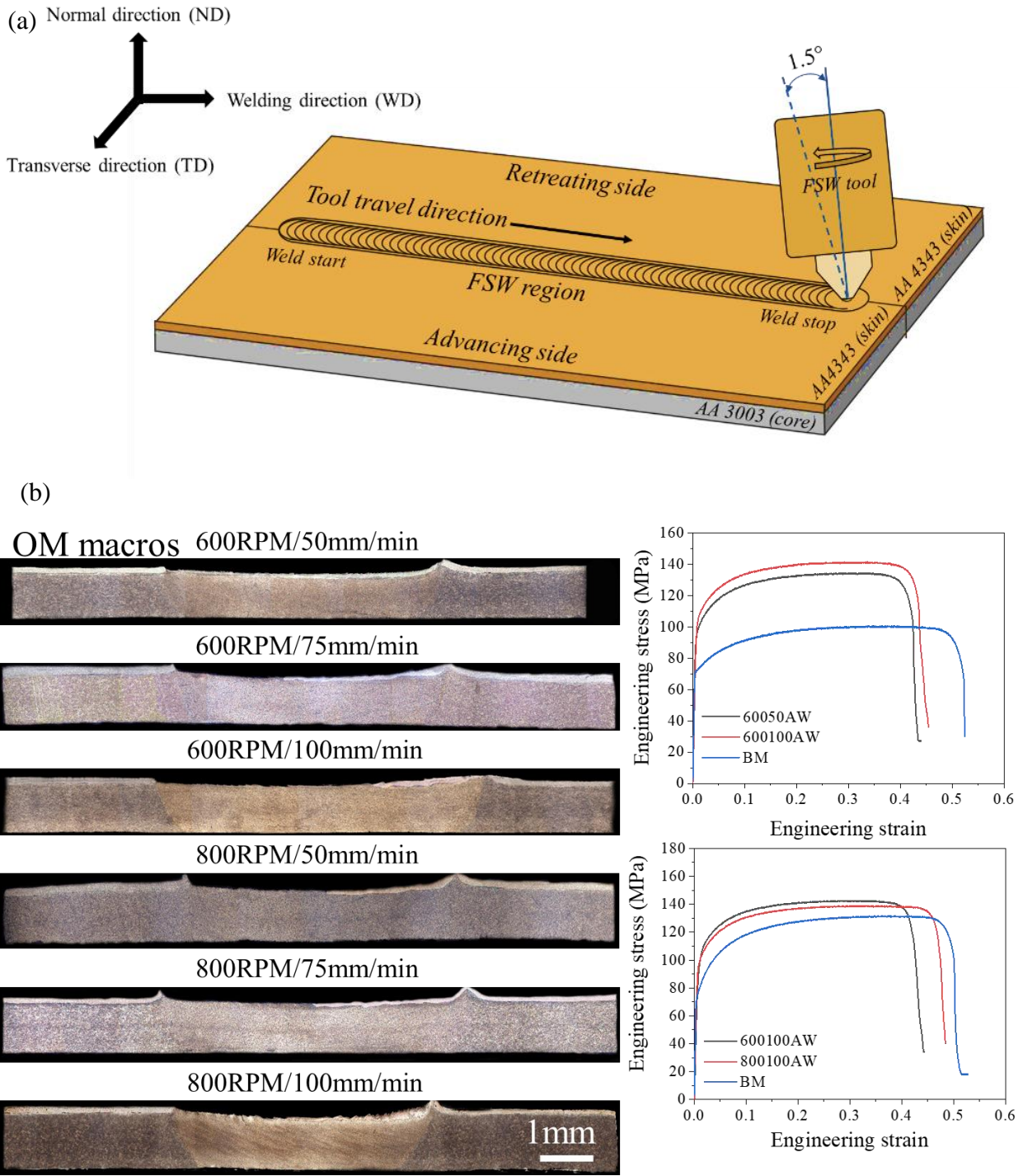


Fig. 2.1 (a) Schematic representation of linear (butt) FSW of Al-clad-Al thin sheets, (b) process parameter optimization of FSW of Al-clad thin sheets.

2.3 RESULTS AND DISCUSSION

2.3.1 Process response and optical microscopy

Initially, the mechanical interaction between the tool shoulder and the clad sheet caused a rapid increase in both the force and torque (Fig. 2.2). Afterward, the continuous tool pin stirring inside the candidate material generated an adequate amount of heat until it reached its desired penetration depth, caused thermal softening of the material [22]. The process responses remained nearly stable after the tool traveled in its desired joining direction. The OM image (Fig. 2.3(a)) of the FSW cross-section shows a joint configuration, including the SZ and the TMAZ adjacent to the existing clad layer (B_T) on the core alloy (B_B) in the BM. An enlarged view of the retreating side (RS) of the SZ (Fig. 2.3(b)) reveals the existence of the clad layer on the core alloy with an interfacial boundary. The shape of the clad layer (near the RS) was changed compared to the BM condition. The clad layer was diminished in the direction of the AS of the SZ. Additionally, no macroscopic joining defects were observed throughout the joint cross-section.

2.3.2 Clad-core intermixing study by EPMA

The intermixing flow pattern of the clad layer to the core was determined by the elemental mapping of Si inside the joint cross-section, as shown in Fig. 2.4(a). Likewise, as shown in Fig. 2.4(b-j), various regions (marked in yellow boxes), including the BM, were analyzed individually. The BM (B_T/B_B) in Fig. 2.4(b) represents relatively low Si in the core (B_B). In contrast, the clad layer (B_T) contained a much higher content of Si particles, which were probably not dispersed inside the Al matrix due to the massive difference between the melting points of Al and Si [23]. Evidence of downward particle movements due to tool compression and shearing during FSW is shown in Fig. 2.4(c), wherein the top region shows the TMAZ-AS interface (T/AS). The formed flow pattern suggests material mixing at the top of the AS (T/AS) since the material commonly

experiences higher amounts of force and temperature at the AS of the SZ during joining [22]. Contrarily, in the RS of the SZ (R_7), the clad layer (Fig. 2.4(j)) survived in a deformed state. This might have been caused by the extrusion motion of the FSW tool pin retreating with instantaneous compressive loading by the tool shoulder at the RS of the SZ. Figure 2.4(e-h) illustrates the scattered distribution of Si at various regions in the SZ. The AS of the SZ (R_1) shows the typical nature of the Si flow with uneven particle distribution, and the middle of the SZ (R_3) indicates the presence of Si-rich bands, as depicted in Fig. 2.4(d, f). The formation of these bands suggests the clustering of Si particles in the presence of a high amount of heat generated at the upper center position of the SZ. In contrast, Fig. 2.4(i) shows the nearly zero intensity of the average Si distribution at the bottom of the SZ (R_6). This phenomenon suggests that the intermixing between clad and core was limited, to some extent, to the top of the SZ.

2.3.3 Precipitation behavior within the SZ by SEM

The intermixing of the clad layer and the core, which increased the Si content in the SZ, brought out interesting changes in the precipitation in the SZ, which differed from the typical precipitation behavior of the aluminum alloys selected in this study. Generally, both materials are non-heat-treatable and exhibit precipitation inside the aluminum matrix during processing [13,24-26]. As shown in the results of the EPMA analysis (Fig. 2.4), the severe stirring motion of the tool during FSW induced the material transfer of Si into the AA3003 core and resulted in a higher Si content in the SZ compared with the AA3003 BM. The formation of precipitates during FSW has thus become of great interest. The SEM results at four different regions - near the AS (P_1), center of SZ (P_2), bottom of SZ (P_3), and RS (P_4), are individually shown in Fig. 2.5(a-d). EDS point analysis of the precipitates confirmed their possible compositions, as presented in Table 2.2.

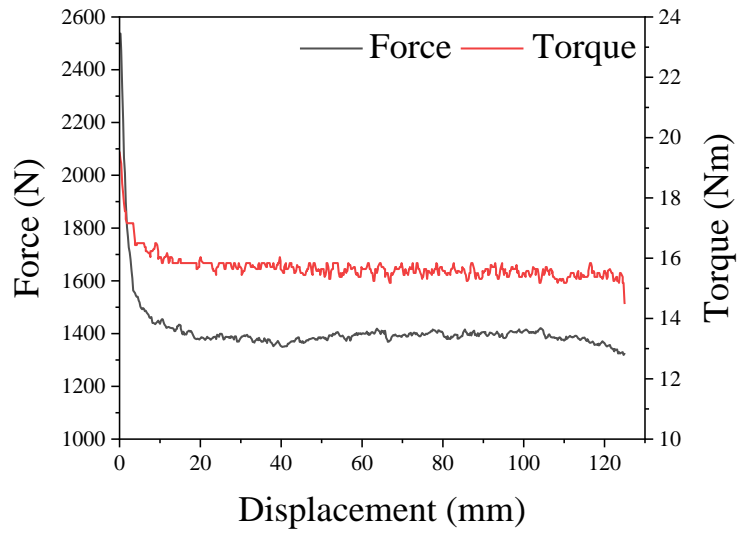


Fig. 2.2 Force-torque responses during the FSW of Al-clad thin sheets.

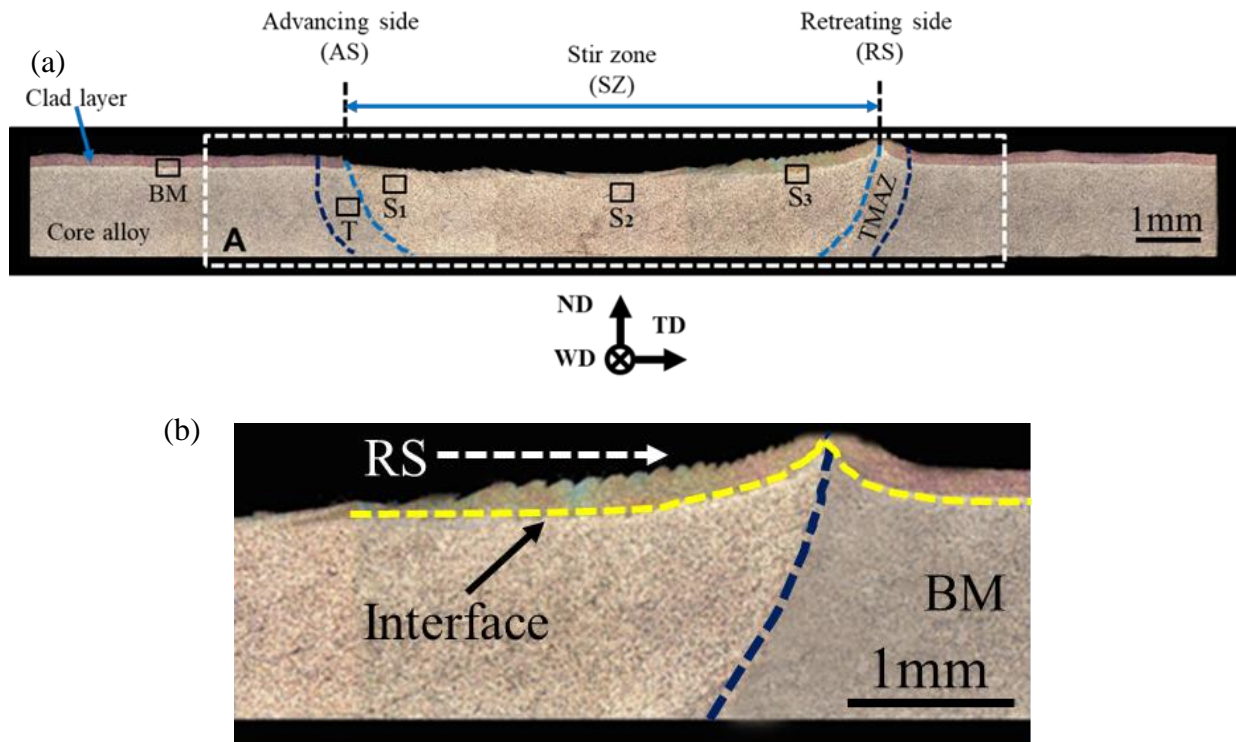


Fig. 2.3 (a) Macrograph of the Al-clad Al FSW cross-section. The black rectangles indicate various regions in the BM, TMAZ, and SZ for EBSD, and a white dashed rectangle (A) represents the area for EPMA analysis. (b) Magnified view of the RS of the SZ.

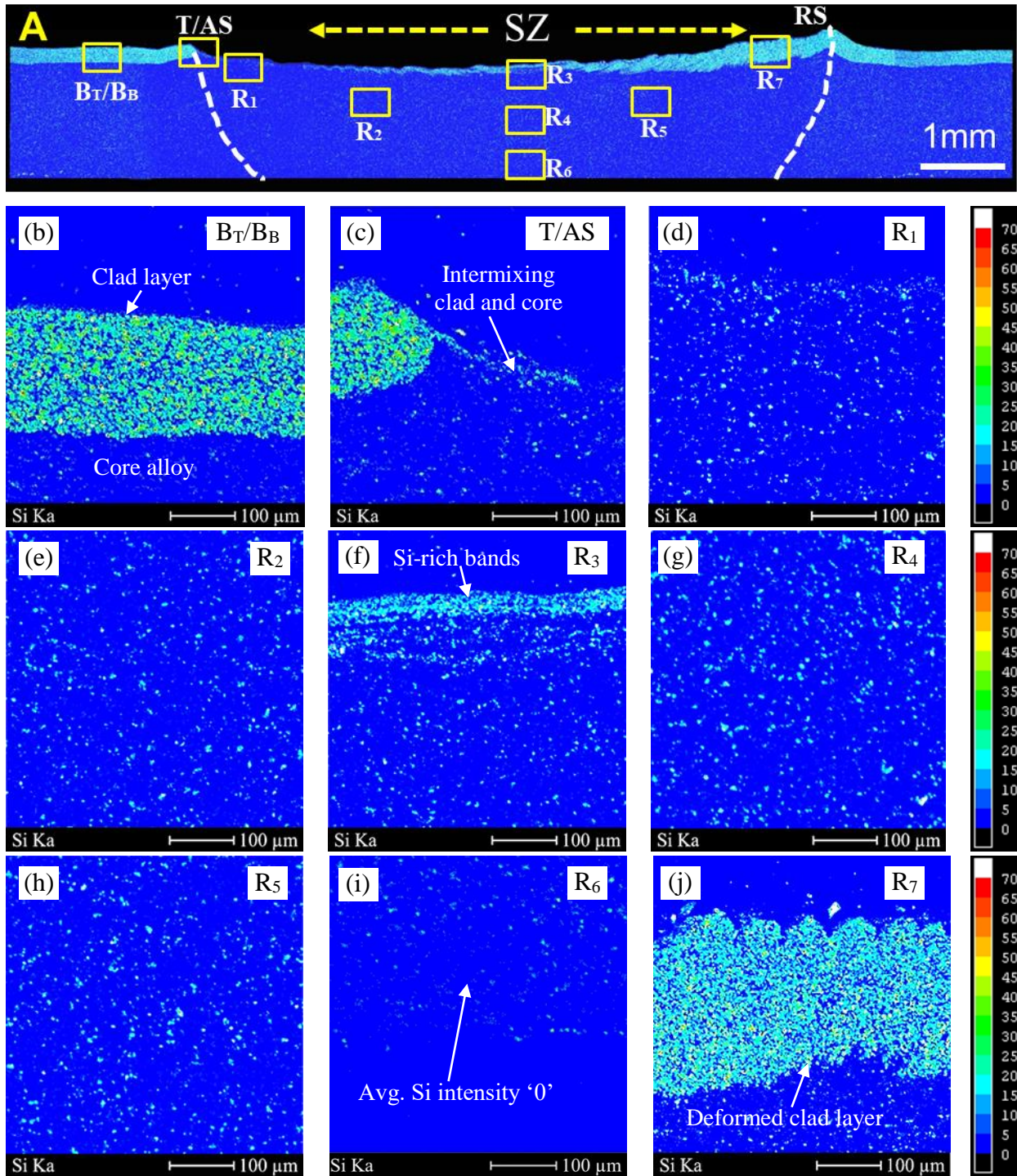


Fig. 2.4 (a) EPMA Si-mapping of the region (A). Magnified images of the sites marked: (b) BM (B_T/B_B); (c) TMAZ and AS interface; (d-j) various regions of the SZ (R₁–R₇), respectively.

Based on their composition, the formation of α -Al (Fe, Mn) Si precipitates along with Al_6 (Mn, Fe) was confirmed in the SEM image (Fig. 5(a)) at the AS of SZ. Tan et al. [13] studied AA3003 FSW joints and mentioned only the presence of Al_6 (Mn, Fe) and MnAl_6 precipitations within the SZ. With the intermixing of the clad layer and the core, the generation of frictional heat, the severe plastic deformation, and the continuous mechanical stirring by the tool in the SZ increased the diffusion coefficient of the Si inside the Al matrix in the SZ [27]. This further promoted the occurrence of α -Al (Fe, Mn) Si quaternary phases in the SZ during FSW. It is also speculated that the Si-induced precipitation was restricted to the upper side of the SZ (Fig. 2.5(a, b, and d)), where most of the precipitates had Al, Mn, Si, and traces of Fe in their compositions; the bottom of the stir zone (Fig. 2.5(c)) was predominated with the Al (0.7% Mn) and Al_6 (Mn, Fe). Finally, the formation of dense precipitation valley (DPV) (Fig. 2.5(d)) was identified near the deformed clad layer at the RS. This region contained various precipitates, including α -Al (Fe, Mn) Si, α -AlMnSi, and AlSi_2 . EDS elemental maps over the SEM images of the BM and RS of the SZ (P_4) are presented in Fig. 2.6(a, b), revealing the presence of unreacted Si particles in huge amounts inside the DPV at the RS. Si particles inside DPV are mainly due to the material flow originating from the AS of SZ, which reached RS through back extrusion under the rotation tool pin during joining. Also, the white-colored (bright) clustered Si particles are also spotted in the AS (Fig. 2.5(a)), and they further increased in the middle of the SZ (Fig. 2.5(b)).

2.3.4 Microstructural characterization by EBSD

The BSE image of the BM (Fig. 2.7(a)) shows that the two dissimilar aluminum alloys were bonded as the clad layer and the core, respectively. EDS chemical analysis was carried out along the yellow dashed line (Fig. 2.7(a1)) to determine the Si and Al intensities across the clad-core interface. The presence of sharp Si peaks alongside the Al dips could be observed up to 150

μm from the line scanning, after which this phenomenon vanished, indicating an interface (marked with the black dashed line) between the two different aluminum alloys. The IPF map of the BM shows a combination of fine (B_T) and coarse (B_B) grain structures with average grain sizes of $12.27 \pm 1.51 \mu\text{m}$ and $46.55 \pm 2.73 \mu\text{m}$, respectively, in Fig. 2.7(b).

The grain boundary distributions inside the clad layer and the core differed from each other. The number of HAGBs (blue lines) and LAGBs (red lines) were almost the same (50%) in the B_T , whereas the B_B had more LAGBs (red lines, 70%), as shown in Fig. 2.7(c). The KAM map explains the locally accumulated misorientation with an average KAM value of 1.01 (Fig. 2.7(d)), representing the high-order deformation accumulated strains within the grains near the cladding interface. The necessary amount of cold work while manufacturing the selected two-ply clad thin sheet is the primary reason behind this [28,29]. The GOS map (Fig. 2.7(e)) similarly confirms the overall deformed grain structures (89.4%) of the BM, including a few recrystallized grains, particularly within the B_T .

The microstructure of TMAZ in the core (marked T, Fig. 2.3(a)) was assessed near the AS of SZ. The IPF and GOS maps indicate primarily deformed grain structures (about 90.8%) with an average grain size of $35.07 \pm 6.74 \mu\text{m}$, as shown in Fig. 2.8(a, d). There are fewer HAGBs (26.2%) in the TMAZ, and most of the region was dominated by LAGBs (73.8%), as represented in Fig. 2.8(b). The average KAM value of 1.39 (Fig. 2.8(c)) suggests a possible rise in misorientation, signifying the presence of many dislocations than the BM. As the circumferential region of the SZ, the TMAZ represents a highly strained region resulting from plastic deformation, similar to hot-working of metallic material. The massive amount of LAGBs and deformed grains were most likely caused by the plastic deformation from the FSW process, with some reduction in grain size due to partial recrystallization in the TMAZ [30-32].

Table 2.2 Possible elemental compositions (at.%) of various precipitates

Precipitates	Al	Si	Mn	Fe
$\alpha - \text{Al}(\text{Fe}, \text{Mn})\text{Si}$	Bal.	7 - 8	0.13 - 0.16	0.17 - 0.23
$\alpha - \text{AlMnSi}$	96.69	2.97	0.35	-
$\text{Al}_6(\text{Mn}, \text{Fe})$	98.52	-	0.73	0.75

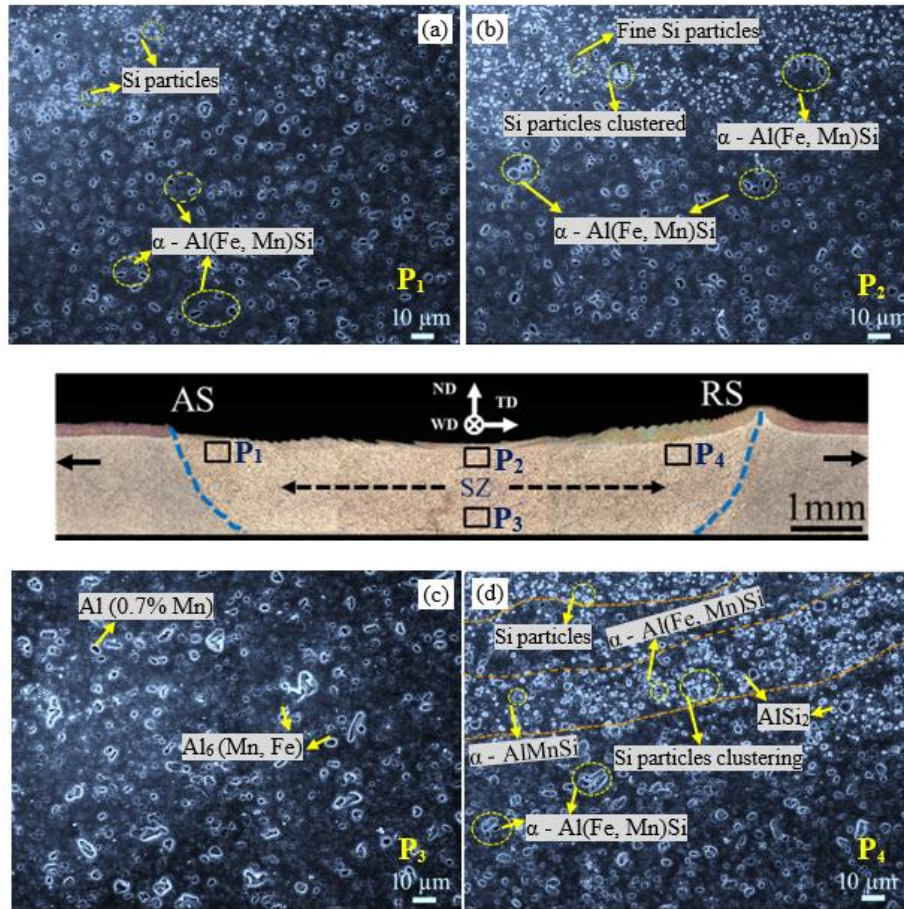


Fig. 2.5 SEM images of the formation of precipitates in the various regions of the SZ of the Al-clad-Al FSW joint cross-section: (a) the AS (P₁), (b) middle of the SZ (top, P₂), (c) the bottom of the SZ (P₃), and (d) the RS (P₄).

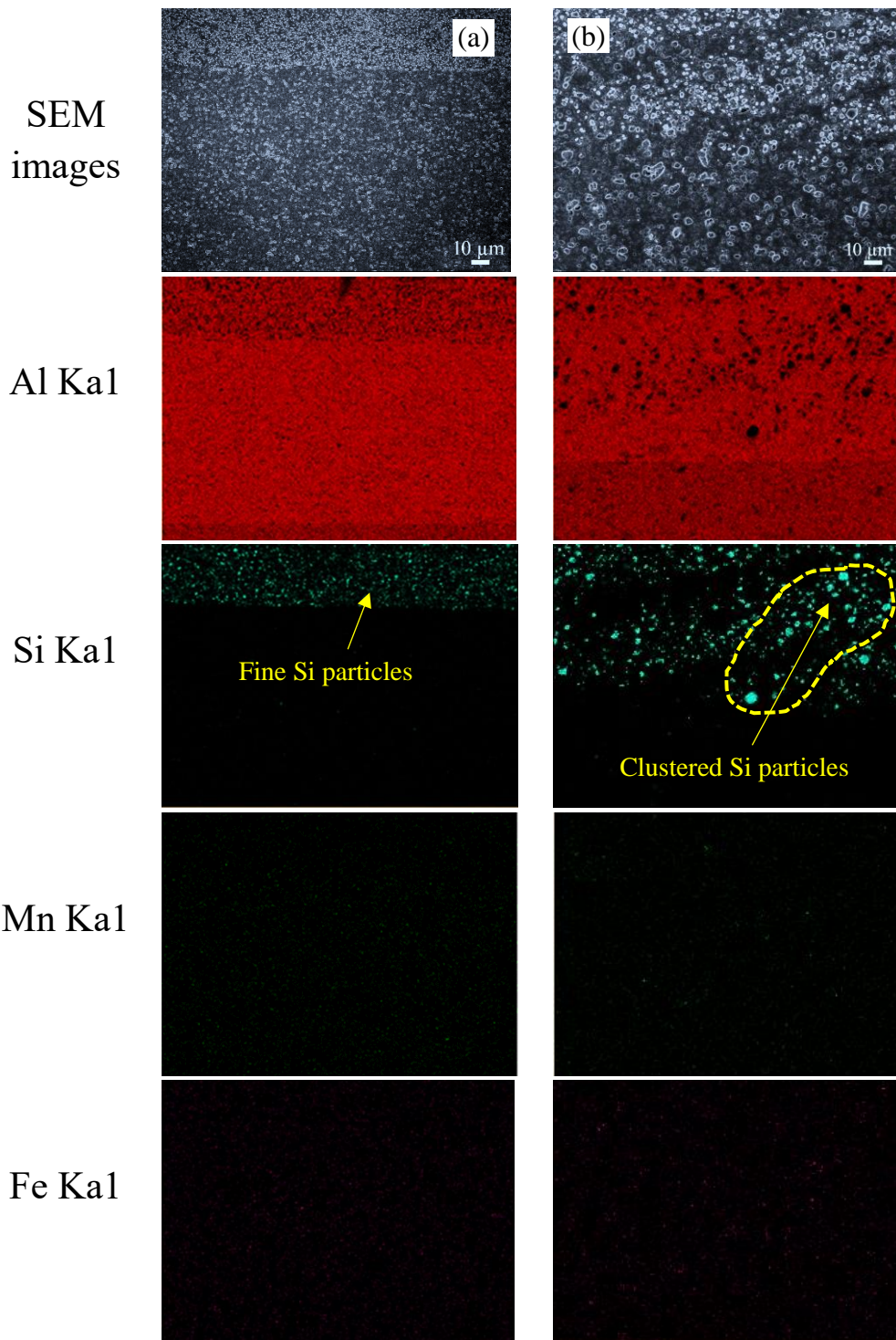


Fig. 2.6 (a, b) Fe-SEM images of BM (BT/BB) and RS of SZ (P₄) and their corresponding EDS elemental mapping of Al, Si, Mn, and Fe.

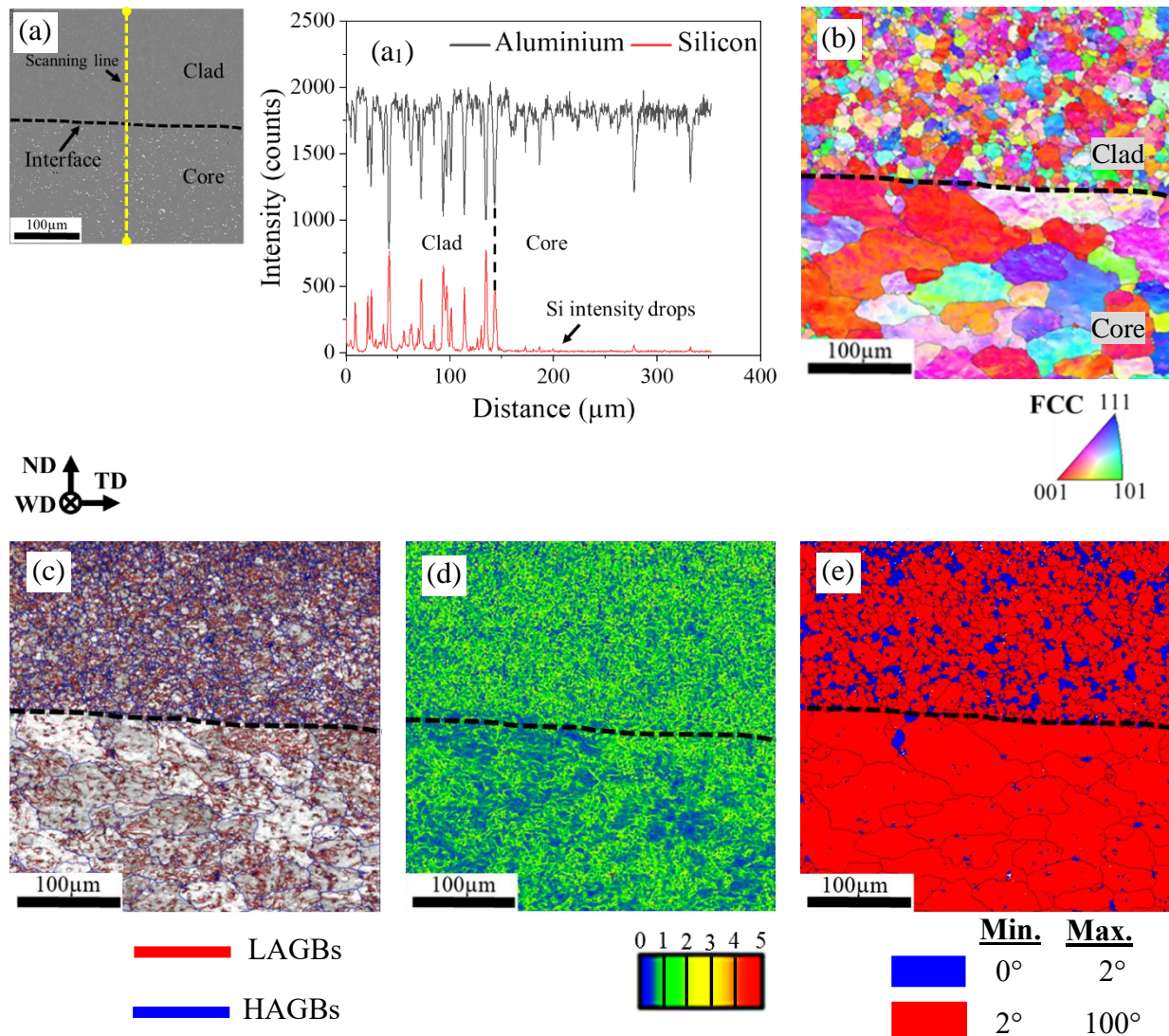


Fig. 2.7 Microstructural analysis of Al-clad thin sheet (a-a₁) BSE image of BM and corresponding EDS line scanning spectrums along the yellow dashed line; EBSD generated (b) IPF map, (c) GBCD map, (d) KAM map, and (e) GOS map of the BM (B_T/B_B).

BSE images of the three different regions in the SZ - AS (S₁, Fig. 2.3(a)), middle of the SZ (S₂), and the RS (marked as S₃) - are depicted in Fig. 2.9(a-c). In Fig. 2.9(a, b), the regions S₁ and S₂ reveal similar appearances, whereas Fig. 2.9(c) displays the presence of the clad and core together in region S₃. This was further confirmed with EDS chemical analysis along the yellow

dashed line (in Fig. 2.9(c)), as shown in Fig. 2.9(c₁). Compared with the BM, the clad-core interface at S₃ was curved (black dashed line), as the processed material experienced high strain due to continuous rotation of the tool shoulder.

A similar type of ultra-fine grain structure compared to the BM condition in S₁, S₂, and S₃ is represented by the IPF maps of all three locations, as shown in Fig. 2.9(d-f). In S₁ and S₂, the average grain sizes were $3.72 \pm 0.77 \mu\text{m}$ and $3.87 \pm 0.84 \mu\text{m}$, respectively. For S₃, the average grain size of the clad and core was separately measured as $3.94 \pm 1.62 \mu\text{m}$ and $3.96 \pm 2.11 \mu\text{m}$, respectively. Figure 2.9(g-i) illustrates the GBCD maps of all three regions, presenting the dominance of the HAGBs over the LAGBs. The HAGBs in the AS (S₁, 73.4%) and middle of the SZ (S₂, 70.4%) appeared similar. For the RS (S₃), the amounts of HAGBs separately measured in the clad layer and the core was 66.8% and 64.4%, respectively. The KAM maps of S₁ and S₂ present intergranular misorientation by rearranging the dislocations in Fig. 2.10(a, b). The average KAM values for S₁ and S₂ were nearly similar (S₁, 0.78; S₂, 0.79) and much lower than the TMAZ (1.274). However, some local accumulation of misorientation was observed, with a sharp increase in the average KAM value (0.97) at S₃ compared to S₁ and S₂ (Fig. 2.10(c)). A deformed clad layer at the RS could contribute to this grain misorientation accumulation along with the back extrusion of the welded materials. From the GOS maps of S₁, S₂, and S₃, amounts of recrystallization in equiaxed ultra-fine grains were found to be 79.8%, 73.4%, and 64.7%, as exhibited in Fig. 2.10(d–f). With the continuous stirring action of the FSW tool on the clad sheets, the SZ simultaneously experienced a high amount of frictional heat and intense plastic deformation that caused the dislocation rearrangement to convert sub-grain boundaries into LAGBs [33,34]. As the deformation increased, the LAGBs gradually turned into HAGBs by continuous dynamic recrystallization (CDR_x), causing extensive grain refinements in the SZ [35,36]. Apart from these,

the development of precipitates and their heterogeneous distribution throughout the SZ could be beneficial for storing the energy caused by plastic deformation during FSW. These energized precipitates further act as the heterogeneous sites of the driving force behind the grain boundary migration toward the formation of HAGBs in the SZ [37]. These undeformed precipitates could easily instigate dislocation pile-up at their surroundings and impede grain growth by conserving recrystallized grains inside the SZ [29,38].

Microtexture analysis by the PFs of the individual BMs (B_T and B_B), TMAZ (near AS), and the SZ (S_1 , S_2 , and S_3), as shown in Fig. 2.11(a-f). The formations of fiber textures and their components have been understood by comparing them with the standard texture fiber orientations of FCC materials in (111) PF [39,40]. The PFs of B_T and B_B revealed B-fiber dominant ideal rolling textures with the presence of $A_1^*/A_2^* \{111\} \langle 112 \rangle$ and $\{111\} \langle 110 \rangle$ components at the maximum intensities of 3.97 and 3.678. The formation of A_1^*/A_2^* and A/\bar{A} roll textures primarily dealt with the deformed coarse grains in the BMs. On the other hand, simple shear textures with the shear components (marked with black triangles, Fig. 2.11(c-f)) were found in the TMAZ and the SZ. The A/\bar{A} shear texture with a maximum intensity of 2.91 (slightly less than that of the BMs) in the TMAZ represented substantial plastic strain with partial recrystallization [30,41].

Inside the SZ (S_1 , S_2 , and S_3), the shear texture was observed to change from A/\bar{A} to B/\bar{B} $\{112\} \langle 110 \rangle$, with maximum intensities of 5.45, 4.54, and 3.859, respectively. The appearance of the weak C texture $\{011\} \langle 110 \rangle$ can also be seen in the corresponding regions (S_1 and S_2) but appeared as the strong texture in S_3 (RS). As the straining increased by the tool plunging and traveling during FSW, the B/\bar{B} and C texture prevailed more than the A/\bar{A} texture, indicating grain refinements through continuous dynamic recrystallization [41-43]. The complex asymmetric nature of the FSW process can explain the appearance of shear texture inside the TMAZ and SZ.

In FSW, continuous rotation of the tool with its threaded pin initiated the shear of the material components with the rotational material flow on the deformation reference frame [39]. As a result, the shear texture was maximized at S_1 of the SZ as the rotational force of the tool and its linear downward mechanical force acted in the same direction at the AS, creating maximal frictional heat and mechanical deformation [44].

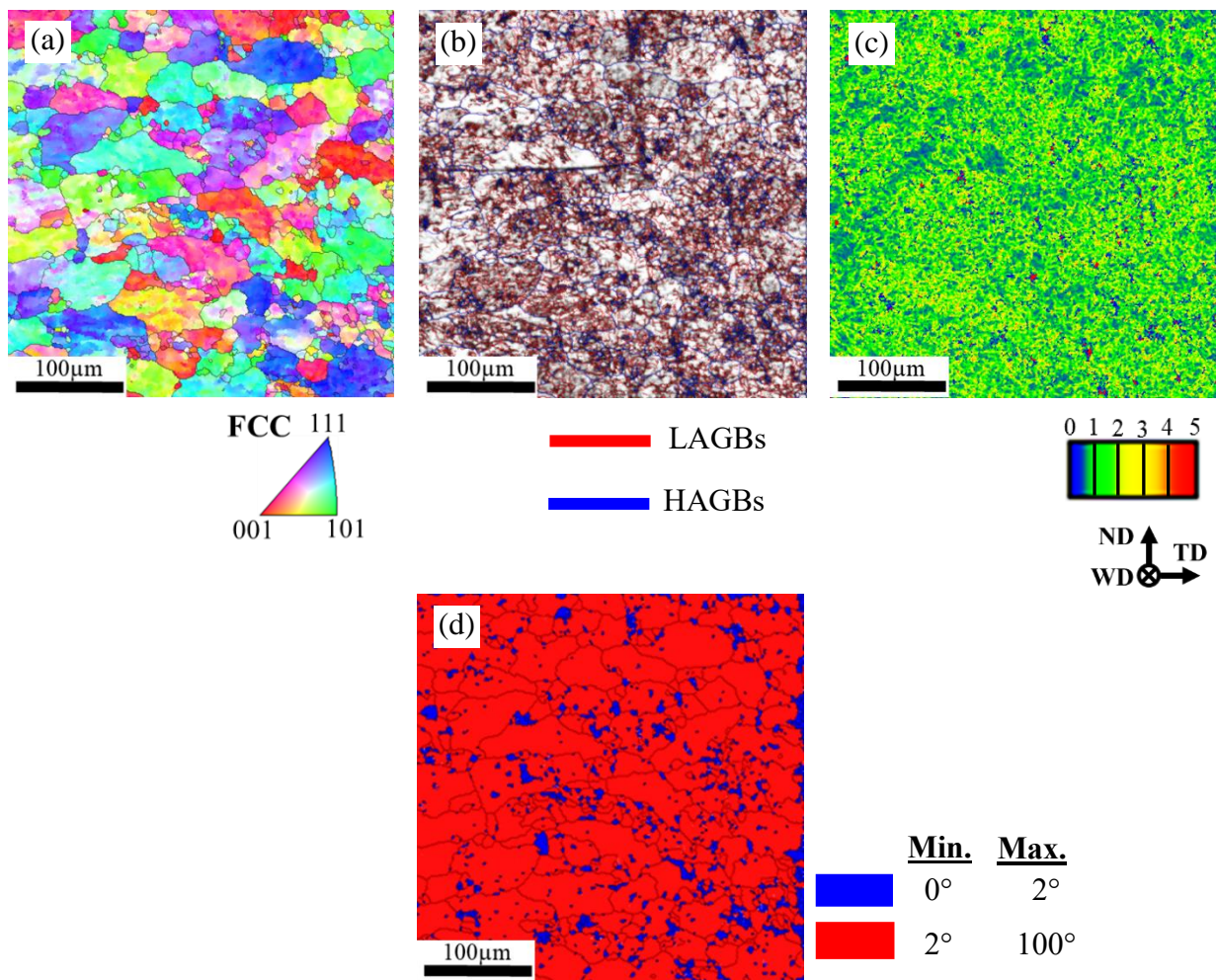


Fig. 2.8 Microstructural analysis of the TMAZ (AS side) (T) of Al-clad-Al FSW joint using EBSD generated (a) IPF map, (b) GBCD map, (c) KAM map, and (d) GOS map.

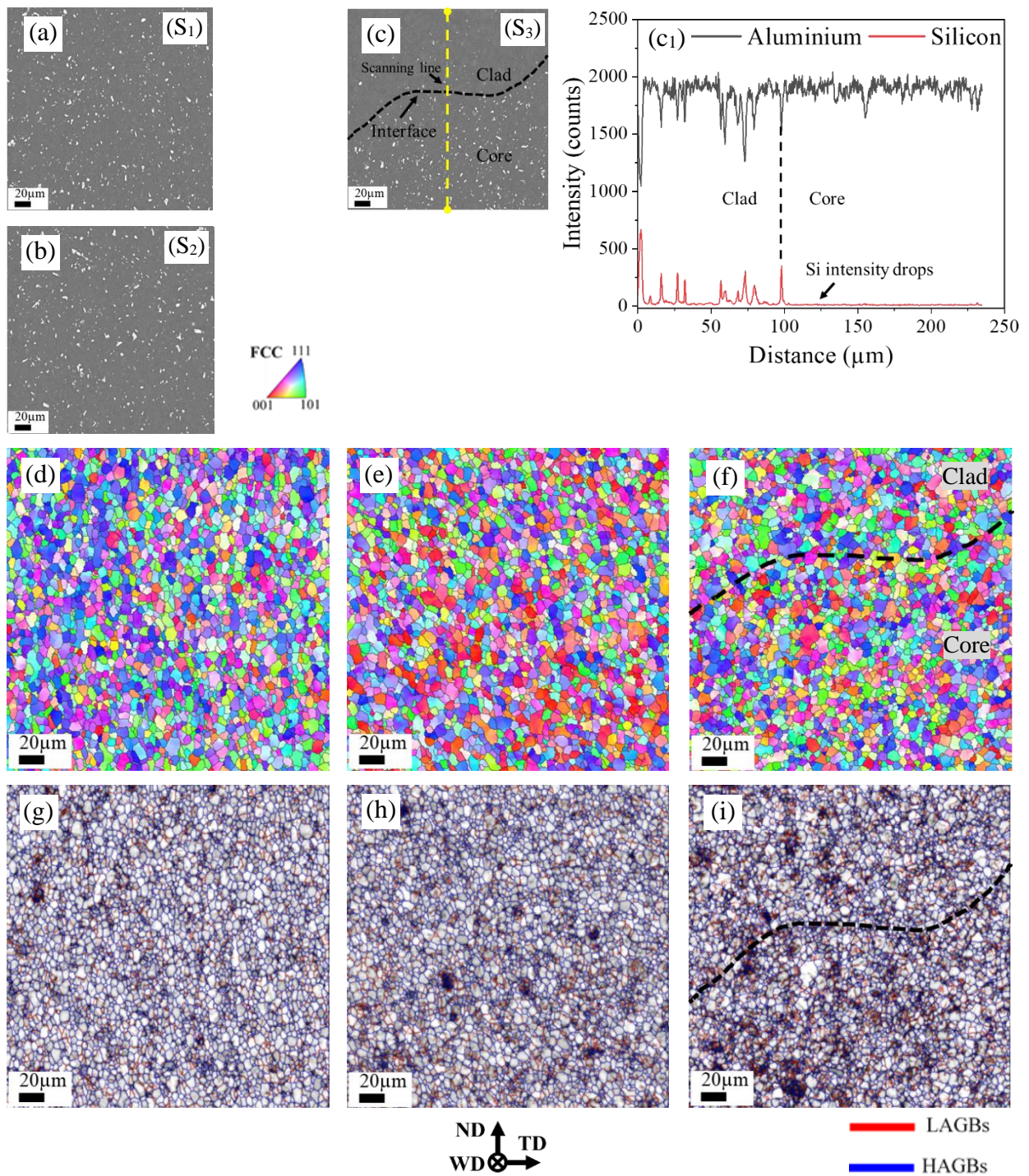


Fig. 2.9 BSE images of (a-c) AS (S₁), middle of the SZ (S₂), and RS (S₃) regions of the SZ; (c₁) corresponding (S₃) element line scanning spectra along the yellow dashed line; EBSD-generated (d-f) IPF maps, and (g-i) GBCD maps for S₁, S₂, and S₃, respectively.

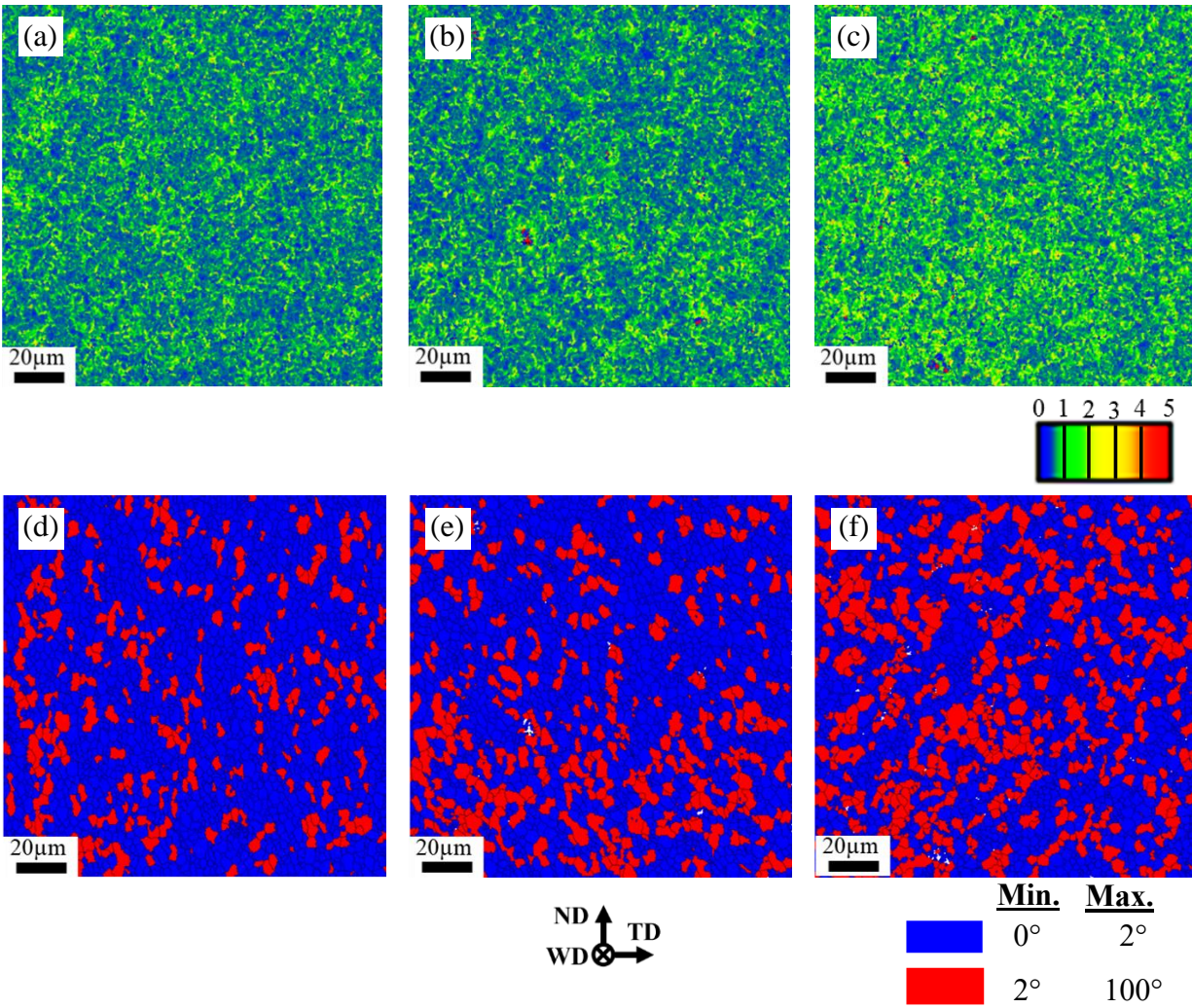


Fig. 2.10 EBSD-generated (a-c) KAM maps, (d-f) GOS maps for the SZ of the Al-clad-Al FSW joint sequentially with AS (S_1), middle of the SZ (S_2), and RS (S_3).

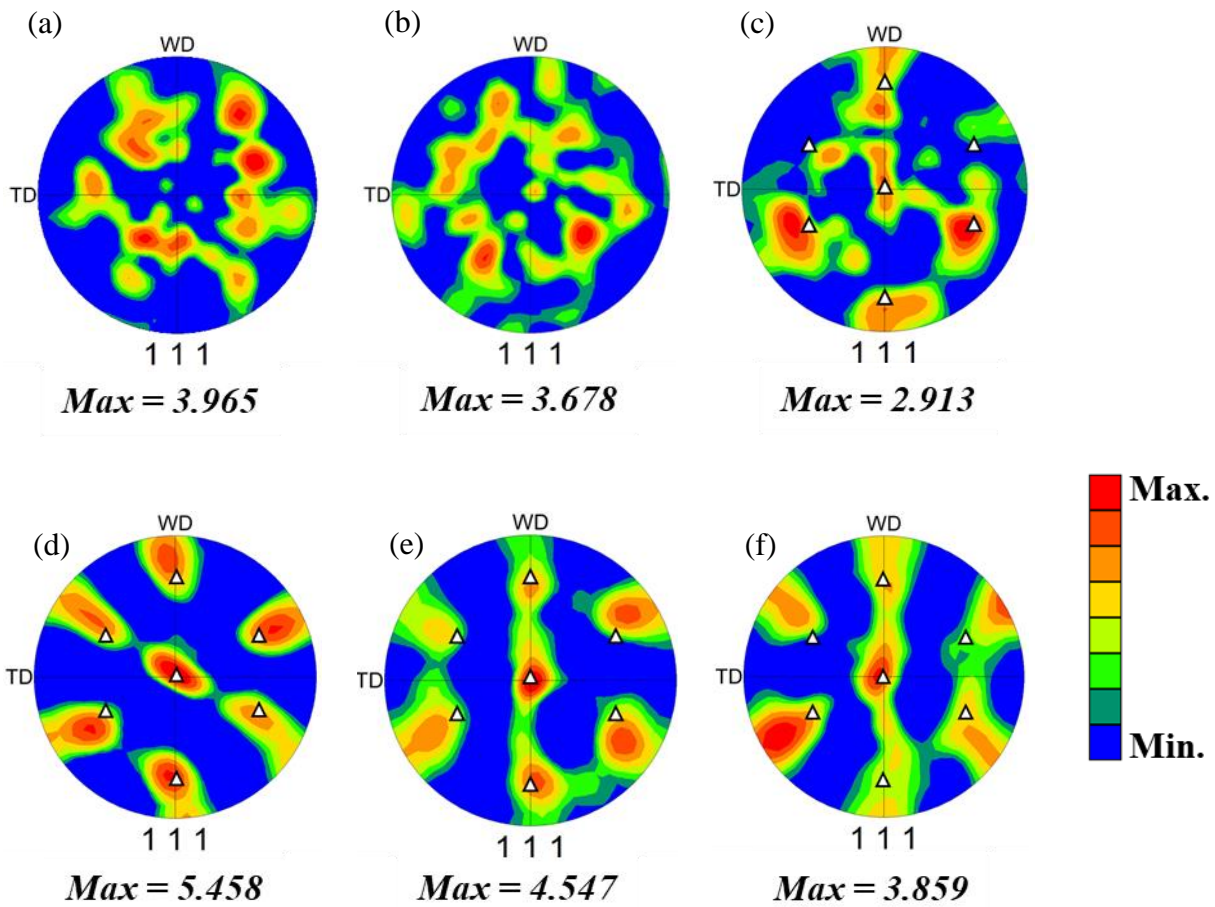


Fig. 2.11 {111} Pole figures acquired from (a) AA4343 (B_T), (b) AA3003 (B_B), (c) TMAZ (T), and (d-f) in the SZ - AS (S₁), middle (S₂), and RS (S₃), respectively for Al-clad-Al FSW joint.

2.3.5 Mechanical properties analysis of the FSW joint

Surface microhardness mapping (2D) on the FSWed Al-clad-Al cross-section was carried out, as shown in Fig. 2.12(a-c). A total of 248 indentations were marked (Fig. 2.12(a)) under a transplant layer of the mapping. Individual observations for the AS and RS of the SZ are detailed in Fig. 2.12(b, c). The surface microhardness in the SZ (54 ± 3.4 HV) was higher than in the BM (B_B; 42 ± 2.1 HV). This is similarly confirmed in Fig. 2.12(d), where the surface microhardness distribution is plotted throughout the mid-thickness of the FSWed cross-section. The appearance

of ultra-fine grain structures in the SZ could cause enhanced microhardness values. Likewise, the formation of various precipitates and the scattered distribution of Si in the SZ resulted in solid solution strengthening during FSW and were found equally responsible for enhancing the surface microhardness [45]. Moreover, the presence of the DPV (Fig. 2.5(d)) with accumulated dislocation (Fig. 2.10(c)) near the RS of the SZ is a potential reason for the higher surface microhardness than in the AS.

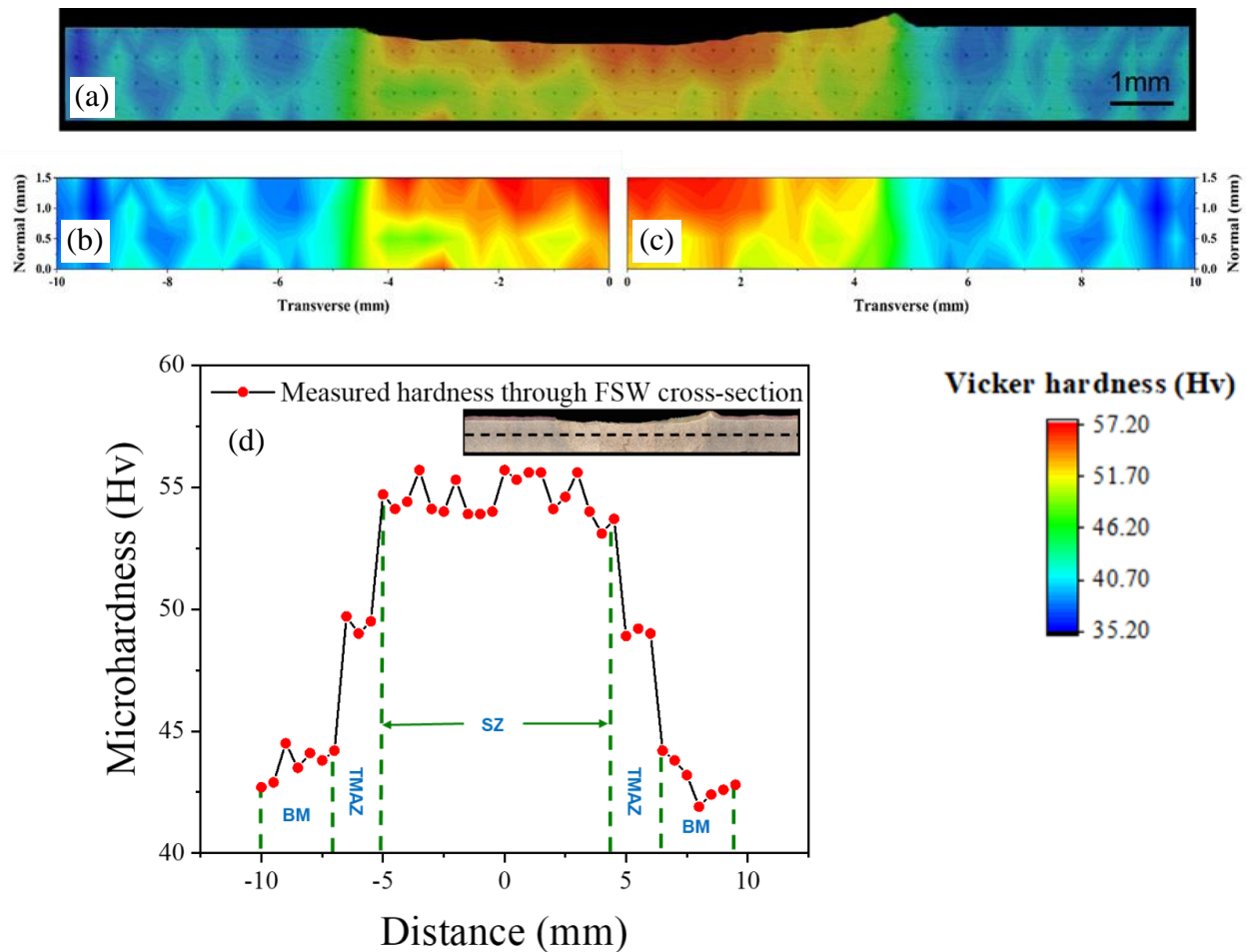


Fig. 2.12 (a) FSW joint cross-section indicating indentation marks under the transparent layer of the microhardness distribution; (b-c) 2D microhardness mapping of the weld cross-section BM to AS and RS to BM; (d) microhardness profile through the mid-thickness of the joint.

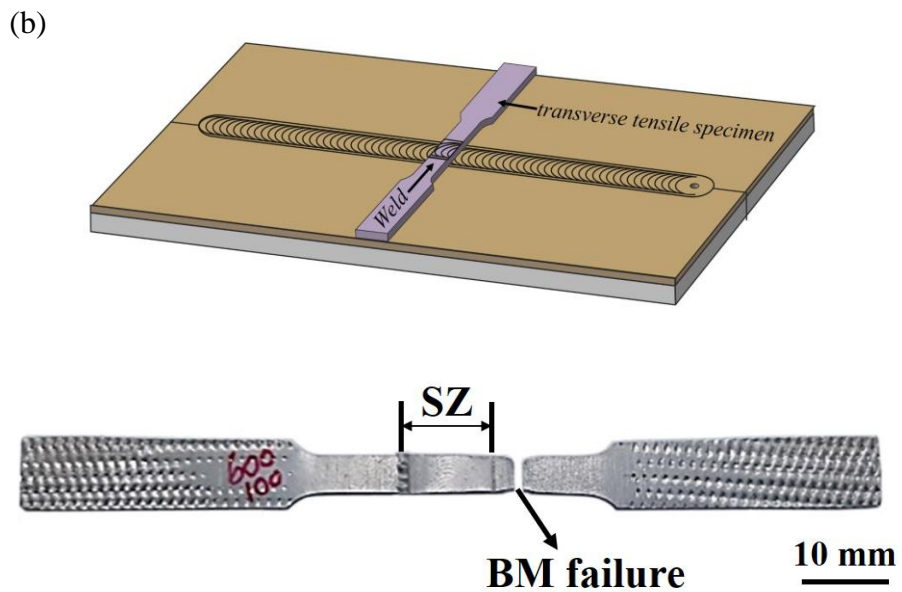
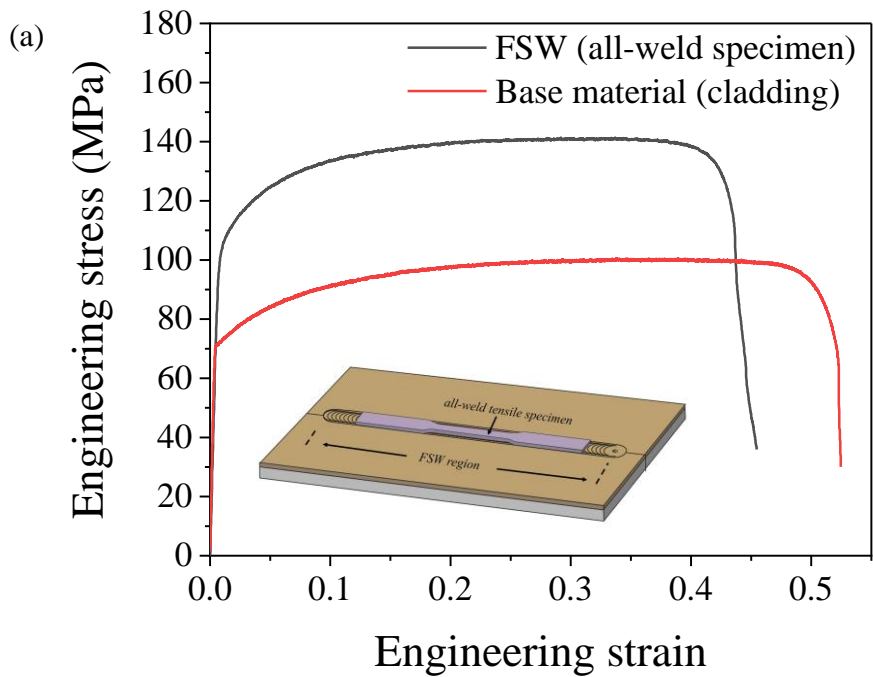


Fig. 2.13 (a) Engineering stress vs. engineering strain curves of the BM and the FSW specimen (all-weld) in black (sample fabrication inset); (b) transverse tensile specimen schematic and broken tensile specimen reveals fracture location from the BM.

Table 2.3 Mechanical properties of the BM and FSW joint

Materials	Yield strength (YS, MPa)	Ultimate tensile strength (UTS, MPa)	Elongation (%)
BM	76.32 ± 2.12	104.94 ± 1.89	52 ± 0.42
FSW	112.64 ± 1.13	142.37 ± 1.45	45 ± 0.79

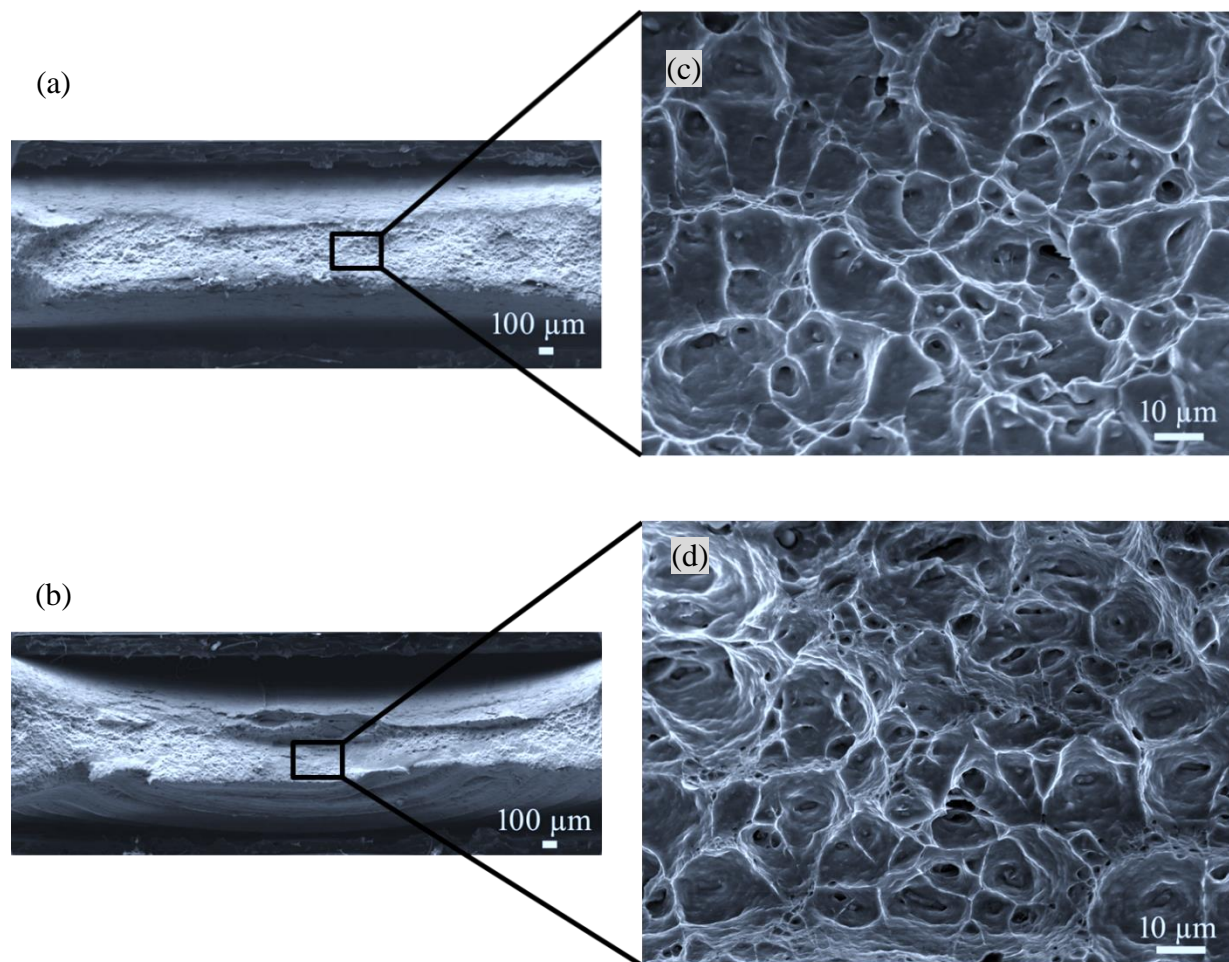


Fig. 2.14 (a, b) SEM macro-fractography of the broken tensile specimens in the BM and the FSW weld sequentially; (c, d) enlarged views of the regions marked with black rectangles in (a, b).

The uniaxial quasi-static tensile test results (Fig. 2.13(a)) indicated an improvement in the strength of the FSWed Al-clad-Al compared to the BM condition. As listed in Table 2.3, the ultimate tensile strength (142.37 ± 1.45) of the joint was increased compared with that of the BM (104.94 ± 1.89). The enormous grain refinement in the SZ also hindered slip transmission and resulted in the higher tensile strength of the FSWed specimen [46,47]. Similarly, precipitation in the SZ clogged the dislocation motion for tensile loading and became accountable for the changes in the mechanical properties of the FSWed Al-clad-Al sheets [48,49]. Enhancement of mechanical strength simultaneously caused a slight reduction in the ductility ($45 \pm 0.79\%$) of the joint related to the BM ($52 \pm 0.42\%$). The pictograph of the fractured transverse tensile specimen (Fig. 2.13(b)) also confirms the successful joining with the occurrence of BM fracture. Finally, the SEM macrofractography of BM and FSW joint (all weld) (Fig. 2.14(a-d)) exhibit typical cup and cone shapes. An enlarged view of the marked regions shows dimples, which indicate ductile failure in both cases.

2.4 CONCLUSIONS

FSW was successfully executed by joining two-ply Al-clad Al thin (1.5 mm) sheets in linear butt configuration. Due to the combined effects of tool compression and shearing, the Si particles flowed downward (clad to the core) inside the SZ and led to the formation of the quaternary phases (precipitates), e.g., α -Al (Fe, Mn) Si. The SZ of the FSW joint was characterized by higher-order HAGBs and ultra-fine dynamically recrystallized grain structures. Surface microhardness and strength of the FSW joint were enhanced, as anticipated from microstructural and texture changes, in addition to the precipitation behavior inside SZ.

REFERENCES

1. M.A. Hannan, F.A. Azidin, A. Mohamed, Hybrid electric vehicles and their challenges: a review, *Renew. Sustain. Energy Rev.* 29 (2014) 135–150.
<https://doi.org/10.1016/j.rser.2013.08.097>
2. M. Yilmaz, P.T. Krein, Review of battery charger topologies, charging power levels, and infrastructure for plug-in electric and hybrid vehicles, *IEEE Trans. Power Electron.* 28 (5) (2013) 2151–2169. <https://doi.org/10.1109/TPEL.2012.2212917>
3. S. Das, P.H. Jean, T. Bruce, Evaluation of the Benefits Attributable to Automotive Light-weight Materials Program Research and Development Projects, Oak Ridge National Laboratory, 2001.
4. S.P. Murugan, M. Cheepu, D.G. Nam, Y.D. Park, Weldability and Fracture Behaviour of Low Carbon Steel/Aluminium/Stainless Steel Clad Sheet with Resistance Spot Welding, *Trans. Indian Inst. Met.* 70 (3) (2017) 759-768.
<https://doi.org/10.1007/s12666-017-1081-2>
5. L. Chen, Z. Yang, B. Jha, G. Xia, J.W. Stevenson, Clad metals, roll bonding and their applications for SOFC interconnects, *J. Power Sources* 152 (2005) 40-45.
<https://doi.org/10.1016/j.jpowsour.2005.01.055>
6. E. Foroozmehr, S. Esmaeili, D.J. Lloyd, M. Gallerneault, Modeling of solutionizing and solute redistribution in a co-cast bi-layer Al alloy system, *Metall. Mater. Trans. A* 43 (2012) 1770-1780. <https://doi.org/10.1007/s11661-011-1068-2>
7. M. Karavolis, S. Jha, J. Forster, *ASM Handbook: Welding, Brazing, and Soldering*, D.L. Olson, T.A. Siewert, S. Liu, and G.R. Edqards, eds. ASM Intl. 6 (1993).
8. J. Fallu, H. Izadi, A.P Gerlich, Friction stir welding of co-cast aluminium clad sheet, *Sci. Technol. Weld. Join.* 19 (1) (2014) 9-14.
<https://doi.org/10.1179/1362171813Y.00000000155>
9. Hasanniah, M. Movahedi, Welding of Al-Mg aluminium alloy to aluminium clad steel sheet using pulsed gas tungsten arc process, *J. Manuf. Process.* 31 (2018) 494-501.
<https://doi.org/10.1016/j.jmapro.2017.12.008>
10. S.P. Murugan, M. Cheepu, V. Vijayan, C. Ji, Y.D. Park, The resistance spot weldability of a stainless steel/aluminium/low carbon steel 3-ply clad sheet, *J. Weld. Join.* 36 (1) (2018) 25-33. <https://doi.org/10.5781/JWJ.2018.36.1.3>

11. P. kah, R. Rajan, J. Martikainen, R. Suoranta, Investigation of weld defects in friction-stir welding and fusion welding of aluminium alloys, *Int. J. Mech. Mater. Eng.* 10 (1) (2015) 26. <https://doi.org/10.1186/s40712-015-0053-8>
12. H.M. Rao, B. Ghaffari, W. Yuan, J.B. Jordon, H. Badarinarayan, Effect of process parameters on microstructure and mechanical behaviours of friction stir linear welded aluminium to magnesium, *Mater. Sci. Eng. A.* 651 (2016) 27-36. <https://doi.org/10.1016/j.msea.2015.10.082>
13. Y.B. Tan, X.M. Wang, M. Ma, J.X. Zhang, W.C. Liu, R.D. Fu, S. Xiang, A study on microstructure and mechanical properties of AA3003 aluminum alloy joint by underwater friction stir welding, *Mater. Charact.* 127 (2017) 41–52. <https://doi.org/10.1016/j.matchar.2017.01.039>
14. R. Nandan, T. DebRoy, H.K.D.H. Bhadeshia, Recent advances in friction-stir welding – process, weldment structure and properties, *Prog. Mater. Sci.* 53 (2008) 980–1023. <https://doi.org/10.1016/j.pmatsci.2008.05.001>
15. L. Karlsson, E.L. Berqvist, H. Larsson, Application of friction stir welding to dissimilar welding, *Weld. World.* 46 (2002) 10–14. <https://doi.org/10.1007/BF03266360>
16. B.L. Xiao, D. Wang, J.B. Zhang, Z.Y. Ma, Friction stir welding of SiCp/Al composite and 2024 Al alloy, *Mater. Sci. Forum*, 638–642 (2010) 1500–1505. <https://doi.org/10.4028/www.scientific.net/MSF.638-642.1500>
17. G. Mathers, *The welding of aluminium and its alloys*, Woodhead publishing series in welding and other joining technologies, 2002, 35-50. <https://doi.org/10.1533/9781855737631.35>
18. S. Tierce, N. Pébère, C. Blanc, C. Casenave, G. Mankowski, H. Robidou, Corrosion behaviour of brazing material AA4343, *Electrochim. Acta* 52 (2006) 1092-1100. <https://doi.org/10.1016/j.electacta.2006.07.007>
19. S. Tierce, N. Pébère, C. Blanc, C. Casenave, G. Mankowski, H. Robidou, Corrosion behaviour of brazed multilayer material AA4343/AA3003/AA4343: Influence of coolant parameters, *Corros. Sci.* 49 (12) (2007) 4581-4593. <https://doi.org/10.1016/j.corsci.2007.04.013>
20. M. Hajizadeh, S. Emami, T. Saeid, Influence of welding speed on microstructure formation in friction-stir-welded 304 austenitic stainless steels, *Int. J. Miner. Metall. Mater.* 27 (11) (2020)1517–1524. <https://doi.org/10.1007/s12613-020-2001-8>

21. ASTM E8 / E8M-21, Standard Test Methods for Tension Testing of Metallic Materials, ASTM International, West Conshohocken, PA, 2021.
https://doi.org/10.1520/E0008_E0008M-21
22. M. Mondal, H. Das, E.Y. Ahn, S.T. Hong, M.J. Kim, H.N. Han, T.K. Pal, Characterization of friction stir welded joint of low nickel austenitic stainless steel and modified ferritic stainless steel, *Met. Mater. Int.* 23 (2017) 948–957.
<https://doi.org/10.1007/s12540-017-6845-z>
23. X.X. Dong, P. Li, S. Amirkhanlou, S. Ji, P.S. Popel, U. Dahlborg, M.C. Dahlborg, Evidence of disruption of Si-rich microstructure in engineering-lightweight Al-12.2at.%Si alloy melt above liquidus temperature, *Sci. Rep.* 10 (2020) 1-11.
<https://doi.org/10.1038/s41598-020-69972-2>
24. Y.J. Li, L. Arnberg, Evolution of eutectic intermetallic particles in DC-cast AA3003 alloy during heating and homogenization, *Mater. Sci. Eng. A* 347 (2003) 130 – 135.
[https://doi.org/10.1016/S0921-5093\(02\)00555-5](https://doi.org/10.1016/S0921-5093(02)00555-5)
25. S. Tierce, N. Pébère, C. Blanc, G. Mankowski, H. Robidou, D. Vaumousse, J. Lacaze, Solidification and phase transformations in brazed aluminium alloys used in automotive heat exchangers, *Int. J. Cast Met. Res.* 18 (6) (2005) 370 -376.
<https://doi.org/10.1179/136404605225023144>
26. J. Lacaze, S. Tierce, M.C. Lafont, Y. Thebault, N. Pébère, G. Mankowski, C. Blanc, H. Robidou, D. Vaumousse, D. Daloz, Study of the microstructure resulting from brazed aluminium materials used in heat exchangers, *Mater. Sci. Eng. A* 413 (2005) 317 – 321.
<https://doi.org/10.1016/j.msea.2005.08.187>
27. S. Fujikawa, K. Hirano, Y. Fukushima, Diffusion of silicon in aluminum, *Metall. Mater. Trans. A.* 9 (1978) 1811–1815. <https://doi.org/10.1007/BF02663412>
28. A. Kar, S. Malopheyev, S. Mironov, R. Kaibyshev, S. Suwas, S.V. Kailas, A new method to elucidate fracture mechanism and microstructure evolution in titanium during dissimilar friction stir welding of aluminium and titanium, *Mater. Charact.* 171 (2021) 110791.
<https://doi.org/10.1016/j.matchar.2020.110791>
29. M.M.Z. Ahmed, S. Ataya, M.E.S. Seleman, H.R. Ammar, E. Ahmed, Friction stir welding of similar and dissimilar AA7075 and AA5083, *J. Mater. Process. Technol.* 242 (2017) 77-91. <https://doi.org/10.1016/j.jmatprotec.2016.11.024>
30. R.S. Mishraa, Z.Y. Ma, Friction stir processing, In: *Friction stir welding and processing*, Springer, Cham. (2014) 259-296. https://doi.org/10.1007/978-3-319-07043-8_9

31. F. Khodabakhshi, A.P. Gerlich, On the correlation between indentation hardness and tensile strength in friction stir processed materials, *Mater. Sci. Eng. A* 789 (2020) 139682. <https://doi.org/10.1016/j.msea.2020.139682>
32. T.R. McNelley, S. Swaminathan, J.Q. Su, Recrystallization mechanisms during friction stir welding/processing of aluminum alloys, *Scripta Mater.*, 58 (5) (2008), pp. 349-354. <https://doi.org/10.1016/j.scriptamat.2007.09.064>
33. A. Kar, B. Vicharapu, Y. Morisada, H. Fuji, Elucidation of interfacial microstructure and properties in friction stir lap welding of aluminium alloy and mild steel, *Mater. Charact.* 168 (2020) 110572. <https://doi.org/10.1016/j.matchar.2020.110572>
34. S.Y. Anaman, S. Ansah, Y.F. Li, H.H. Cho, J.S. Lee, H.N. Han, S.T. Hong, Experimental and numerical studies on the electrochemical properties of an electrically assisted pressure joint of austenitic stainless steel and Ni-based superalloy, *Mater. Charact.* 165 (2020) 110404. <https://doi.org/10.1016/j.matchar.2020.110404>
35. M. Mondal, H. Das, S.T. Hong, B.S. Jeong, H.N. Han, Local enhancement of the material properties of aluminium sheets by a combination of additive manufacturing and friction stir processing, *CIRP Annals* 68 (1) (2019) 289-292. <https://doi.org/10.1016/j.cirp.2019.04.109>
36. M. Mondal, S. Basak, H. Das, S.T. Hong, H. Choi, J.W. Park, H.N. Han, Manufacturing of magnesium/aluminum bimetallic ring components by friction stir assisted simultaneous forging and solid-state joining, *Int. J. of Precis. Eng. and Manuf.-Green Tech.* (2020). <https://doi.org/10.1007/s40684-020-00244-0>
37. K. Huang, K. Marthinsen, Q. Zhao, R.E. Logé, The double-edge effect of second-phase particles on the recrystallization behaviour and associated mechanical properties of metallic materials, *Prog. Mater. Sci.* 92 (2018) 284-359. <https://doi.org/10.1016/j.pmatsci.2017.10.004>
38. J.Q. Su, T.W. Nelson, R. Mishra, M. Mahoney, Microstructural investigation of friction stir welded 7050-T651 aluminium, *Acta Mater.* 51 (3) (2003) 713 – 729. [https://doi.org/10.1016/S1359-6454\(02\)00449-4](https://doi.org/10.1016/S1359-6454(02)00449-4)
39. R.W. Fonda, J.F. Bingert, Texture variations in aluminium friction stir weld, *Scr. Mater.* 57(11) (2007) 1052-1055. <https://doi.org/10.1016/j.scriptamat.2007.06.068>
40. U.F.H.R. Suhuddin, S. Mironov, Y.S. Sato, H. Kokawa, Grain structure and texture evolution during friction stir welding of thin 6016 aluminum alloy sheets, *Mater. Sci. Eng. A*. 527 (2010) 1962-1969. <https://doi.org/10.1016/j.msea.2009.11.029>

41. R.W. Fonda, K.E. Knipling, J.F. Bingert, Microstructural evolution ahead of the tool in aluminum friction stir welds, *Scr. Mater.* 58 (2008) 343-348.
<https://doi.org/10.1016/j.scriptamat.2007.09.063>
42. X.C. Liu, Y.F. Sun, H. Fujii, Clarification of microstructure evolution of aluminum during friction stir welding using liquid CO₂ rapid cooling, *Mater. Des.* 129 (2017) 151-163.
<https://doi.org/10.1016/j.matdes.2017.05.013>
43. X.C. Liu, Y.F. Sun, T. Nagira, K. Ushioda, H. Fujii, Microstructure evolution of Cu–30Zn during friction stir welding, *J. Mater. Sci.* 53 (2018) 10423-1044.
<https://doi.org/10.1007/s10853-018-2313-5>
44. S. Emani, T. Saeid, R.A. Khosroshahi, Microstructural evolution of friction stir welded SAF 2205 duplex stainless steel, *J. Alloys Compd.* 739 (2018) 678 - 689.
<https://doi.org/10.1016/j.jallcom.2017.12.310>
45. H.J. Aval, S. Serajzadeh, A.H. Kokabi, Evolution of microstructures and mechanical properties in similar and dissimilar friction stir welding of AA5086 and AA6061, *Mater. Sci. Eng. A* 528 (28) (2011) 8071-8083.
<https://doi.org/10.1016/j.msea.2011.07.056>
46. X.D. Zhang, N. Hansen, Y.K. Gao, X.X. Huang, Hall-Petch and dislocation strengthening in graded nanostructured steel, *Acta Mater.* 60 (2012) 5933 – 5943.
<https://doi.org/10.1016/j.actamat.2012.07.037>
47. S. Memon, M. Paidar, S. Mehrez, K. Cooke, O.O. Ojo, H.M. Lankaran, Effects of materials positioning and tool rotational speed on metallurgical and mechanical properties of dissimilar modified friction stir clinching of AA5754-O and AA2024-T3 sheets, 22 (2021) 1030962. <https://doi.org/10.1016/j.rinp.2021.103962>
48. P.S. De, R.S. Mishra, Microstructural evolution during fatigue of ultrafine grained aluminum alloy, *Mater. Sci. Eng. A* 527 (2010) 7719 – 7730.
<https://doi.org/10.1016/j.msea.2010.08.047>
49. M. Paidar, K. Tahani, R.V. Vignesh, O.O. Ojo, H.R. Ezatpour, A. Moharrami, Modified friction stir clinching of 2024-T3 to 6061-T6 aluminium alloy: Effect of dwell time and precipitation-hardening heat treatment, *Mater. Sci. Eng. A* 791 (2020) 139734.
<https://doi.org/10.1016/j.msea.2020.139734>

CHAPTER III

GAS POCKET-ASSISTED UNDERWATER FRICTION STIR SPOT WELDING

3.1 INTRODUCTION

The subsea industry is rapidly expanding with many offshore constructions to meet the operational demands of crude oil and natural gas worldwide [1]. The offshore structures, especially the submerged pipeline systems, oil-field platforms, drill pipes, and floating vessels, are mainly built in the sea, ranging from a warm marine to an arctic environment [1,2]. Successful installation of these structures involves joining similar or dissimilar materials in bulk. In offshore structures, damage mainly occurs due to corrosive environments, fatigue, cold cracking, design flaws, and other mechanical factors, including defects in welded joints [1,3-5]. Therefore, underwater welding plays a significant role in installing offshore components and regular repair works for safety and trouble-free operation in the subsea industry [1-5].

Most of the underwater wet welding (UWW) is performed with manual metal arc welding (MMAW) and flux-cored arc welding (FCAW) techniques [6,7]. Low-cost and small-scale instruments make these conventional welding methods acceptable regardless of the difficulties caused by the hostile marine environment [7]. However, limited visibility with an unstable welding arc is the major constraint of these methods, as the surrounding seawater comes directly inside the joining area and creates water bubbles. In addition, the weld slag inclusions and strong hydrogen diffusion due to the rapid cooling in direct contact with the seawater degrade the quality of the joints [8-11]. Fydrych and Labanowski [12] revealed that the hydrogen generation during fusion welding is twice as high in the water as in the air, further compounding the challenges by many

folds. Tomków et al. [13] studied UWW of S460N steel and observed massive cracks in the weld zone and HAZ, characterizing the welded joints as highly susceptible to cold cracking. Many attempts have been made to address the core concerns of UWW [14 -19]. Thus, the difficulties encountered during UWW have not been fully resolved and require further technological development.

Friction stir welding/processing (FSW/P) is a solid-state technology in which the joining involves frictional heating and plastic deformation between the non-consumable rotating tool and the workpiece [20-22]. The formation of cast microstructures with other solidification defects can be avoided in FSW as it does not cause the melting of materials [23]. Also, the absence of consumable electrodes has made FSW energy efficient and more acceptable than other fusion joining techniques [24-28]. The FSW/P can be executed efficiently in water by controlling the thermal cycle of the process [29-31]. Miyamori et al. [32] successfully used UFSW on defective medium carbon steel and found a defect-free joining area with higher hardness than FSW in the air. Regarding other challenges, including welder safety, UFSW is very safe as it involves no arc generation, radiation, or electric hazards, and the quality of the joint is less dependent on the water depth than conventional UWW [30]. These features are crucial for developing UFSW as an efficient UWW technique for offshore components installation and maintenance. However, the most notable of subsequent developments with UFSW would be finding a way to divert seawater from the desired area of its operations. This is important to reduce the chances of seawater decomposition, hydrocarbon uptakes, and the deposition of other aggressive species in the joint while performing amid the sea.

Therefore, the research aims to develop a newly designed GAFSSW on a commercially available AA in the presence of inert gas (argon, Ar) pocket in a simulated seawater solution. This

technique will lead to new development in reducing or even eliminating the absorption of corrosive species (like chlorine) from seawater into the welded region. The feasibility of this proposed technique is further emphasized by comparing its performance to UFSSW and FSSW.

3.2 MATERIALS AND EXPERIMENTAL METHODS

3.2.1 Materials

The square blocks of (50 mm × 50 mm) strain-hardened AA5083-H112 were considered the BM (Table 3.1). The effectiveness of AAs over steels with numerous advantages, including reasonable strength-to-weight ratio, thermal conductivity, excellent corrosion resistance, higher recycling value, and longer service life, make them widely used in the subsea industry [33-35]. For example, in the case of oil exploration, replacing steels with AAs in the manufacture of tubular components like drill pipe helps manufacturers get twice the length of Al tubing hanging under its weight than steel [36,37].

Table 3.1 Chemical compositions of AA5083-H112 (wt.%)

Materials	Si	Fe	Cu	Mn	Mg	Cr	Al
AA5083-H112	0.09	0.29	0.02	0.54	4.40	0.07	Balance

3.2.2 Experimental methods

A custom-designed tank of 240 mm in length and width was used to perform GAFSSW, UFSSW, and FSSW, as shown in Fig. 3.1(a). The samples were fixed (Fig. 3.1(b)) with screws, and the welding was executed in bead-on-plate condition. During the UFSSW, the workpiece was

fully immersed in the seawater solution (3.5 wt.% NaCl + distilled water), while the FSSW was performed in the air. In addition, a custom-made acrylic adapter with circular holes on either side was adhesively fixed (Fig. 3.1(c)) at the workpiece center to ensure gas pocket formation during GAFSSW. Gas tubes were plugged into the adapter holes to enable the gas flow inside the adapter, as shown in Fig. 3.1(d, e). The design of the adapter used in this study is shown in Fig. 3.1(f). Finally, the simulated seawater solution was poured into the tank (Fig. 3.1(g)), so the whole workpiece with the adapter (Fig. 3.1(h, i)) was completely immersed. A custom-made H-13 tool with a 13 mm diameter concave shoulder associated with a 5 mm diameter cylindrical pin was used in this study.

The implementation of the GAFSSW process is illustrated by the images presented in Fig. 3.2(a-f). First, the tank with all the internals was clamped (Fig. 3.2(a)) onto the custom-built FSW machine (RM-1, Bond Technologies, Elkhart, IN, USA). Once the gas flow commenced, a water vortex began to form in Fig. 3.2(b). Finally, after continuous gas flow at 1 MPa for 60 seconds, the gas pocket was formed (Fig. 3.2(c)), and tool plunging (Fig. 3.2(d)) was initiated. The tool was extracted upon completion, but the gas flow was uninterrupted (Fig. 3.2(e)) until the workpiece had cooled to room temperature. Eventually, the gas flow stopped, and water filled the adapter (Fig. 3.2(f)) before the workpiece returned from the tank. Besides the formation of the gas pocket, the Ar gas was used to control the thermal cycle of GAFSSW. The process parameters were kept constant for comparative analysis of the GAFSSW over the UFSSW and FSSW, as given in Table 3.2. The process parameter was optimized (Fig. 3.3) based on the proper weld penetration and formation of defects (flash). An embedded data acquisition system recorded the force and torque responses to penetration depths during welding. The temperature profiles were recorded using a type K thermocouple placed 8.5 mm from the tool axis 0.5 mm deep inside the material.

Table 3.2 Optimized weld parameters

Welding cond.	Tool rotational speed (rpm)	Plunge speed (mm/min)	Depth of penetration (mm)	Tool tilt angle (°)
FSSW				
UFSSW	800	100	2.52	0
GAFSSW				

After execution, individual cross-sections perpendicular to the welding direction were cut from the FSSW, UFSSW, and GAFSSW specimens. The cross-sections were polished up to 0.25 μm diamond paste suspension and etched with Keller's reagent for optical microscopy (OM, GX41, Olympus Corp., Tokyo, Japan). The top surfaces of UFSSW and GAFSSW samples were studied under scanning electron microscopy (FE-SEM, SU5000, Hitachi High-Technologies Corp., Japan), followed by the elemental analysis using energy-dispersive spectroscopy (EDS, X-Max, Oxford Instruments America Inc., Concord MA, USA) to confirm the presence of Cl. The appearance of the precipitates was observed through the SEM images of the selected regions in the cross-section of the welded specimens, while the EDS elemental point/area analysis was used to examine their possible chemical compositions. Finally, the cross-sections were electrolytically polished with 60% ethanol and 40% perchloric acid solution for EBSD analysis using FE-SEM equipped with an electron backscatter diffractometer (EBSD, TSL Hikari Super, TSL, USA). EBSD-generated maps, including inverse pole figure (IPF), grain boundary character distribution (GBCD), grain orientation spread (GOS), and kernel average misorientation (KAM), are used for this study.

The mechanical properties of the FSSW, UFSSW, and GAFSSW specimens were determined by surface microhardness and micro indentation tests. The surface microhardness

mapping was performed using an automated Vickers microhardness tester (HM-200, Mitutoyo Corp., Japan). A total of 256 indents were made, applying a load of 0.49 N for a dwell time of 10 seconds for each sample. A displacement control micro stress mapper (MicroSM-IH-01-Master, Frontics Inc., Republic of Korea) was used to perform micro indentation tests for the tensile properties measurements of the welded regions. The tests were performed with a 0.10 mm diameter spherical indenter on the cross-sections of the polished specimens. Loading rate (0.03 mm/min) and holding time (100 ms) were constant in each case. To ensure the reproducibility of the test results, a total of 6 indentation points for each region were considered.

The corrosion analysis was performed based on the potentiodynamic polarization tests using a potentiostat (ZIVE SP2, ZIVELAB, Republic of Korea) consisting of a standard three-electrode cell and a Luggin capillary. The top surfaces of the FSSW, UFSSW, GAFSSW specimen, and BM were used. Samples were polished to 2000 grit and cleaned with ethanol prior to the polarization testing in 3.5 wt.% NaCl simulated seawater solution [38]. Each test sample with an -exposed area of 100 mm² was considered the working electrode, while a graphite rod and a standard saturated calomel electrode (SCE) were used as the counter and reference electrodes, respectively. Before starting the polarization tests, the samples were immersed in 1 liter of fresh electrolyte solution for 60 minutes to calculate the open circuit potentials (OCPs). The polarization tests commenced with a potential scanning rate of 0.1667 mV/s from an initial voltage of -1.4 V versus OCPs to the final voltage of -0.7 V versus SCE. Due to the complex nature of assessing the corrosion behaviors of metals, four potentiodynamic tests were carried out for each sample under the same conditions.

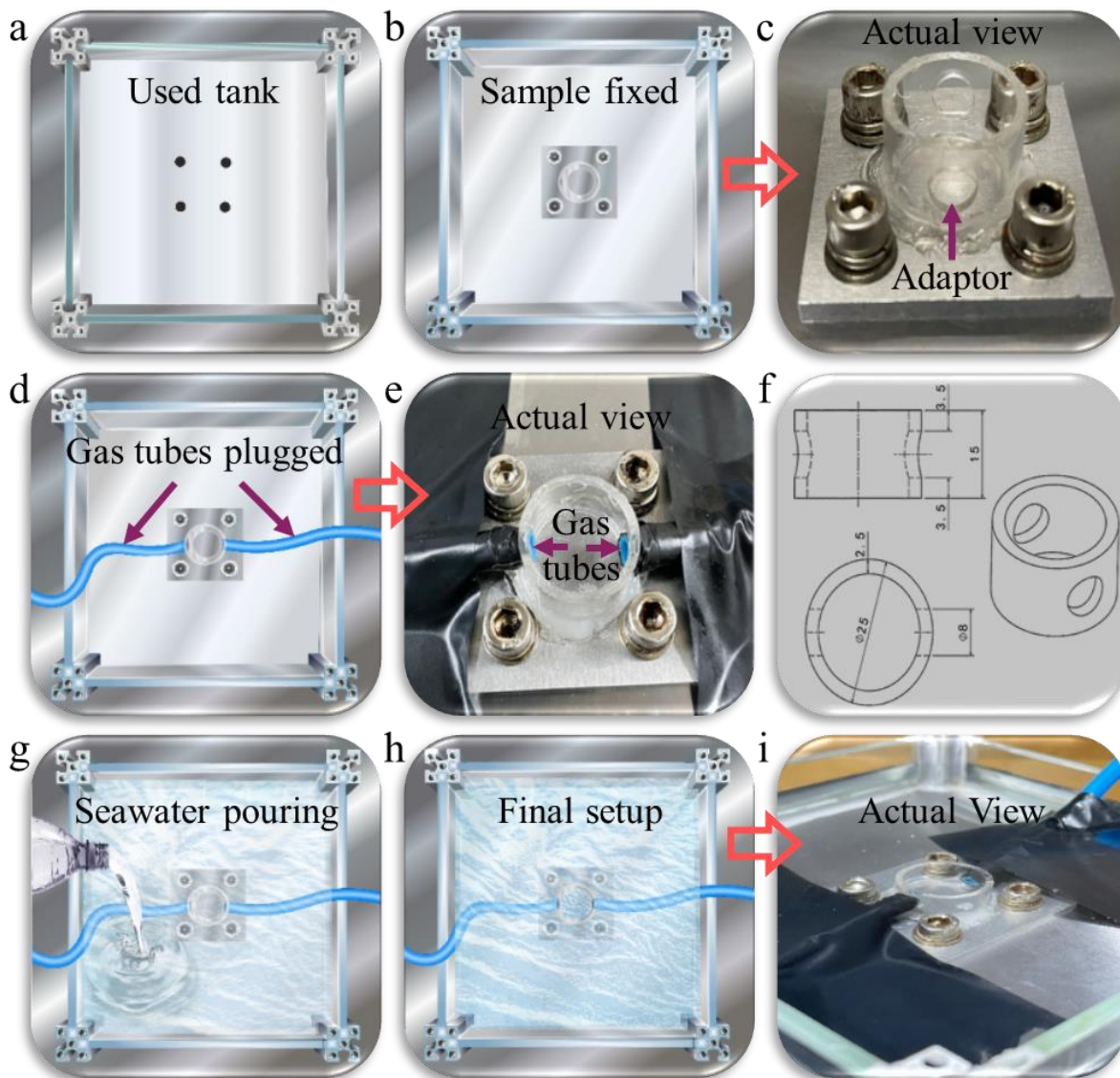


Figure 3.1 Schematic view of (a) the tank, (b, c) sample attachment inside the tank for GAFSSW and its actual view with adapter, (d, e) gas tubes attachment with adapter and actual view with its positions, (f) design of the adapter, (g) seawater filling inside the tank, (h, i) final setup of GAFSSW and its actual view represents the entire sample attachment immersed inside the solution.

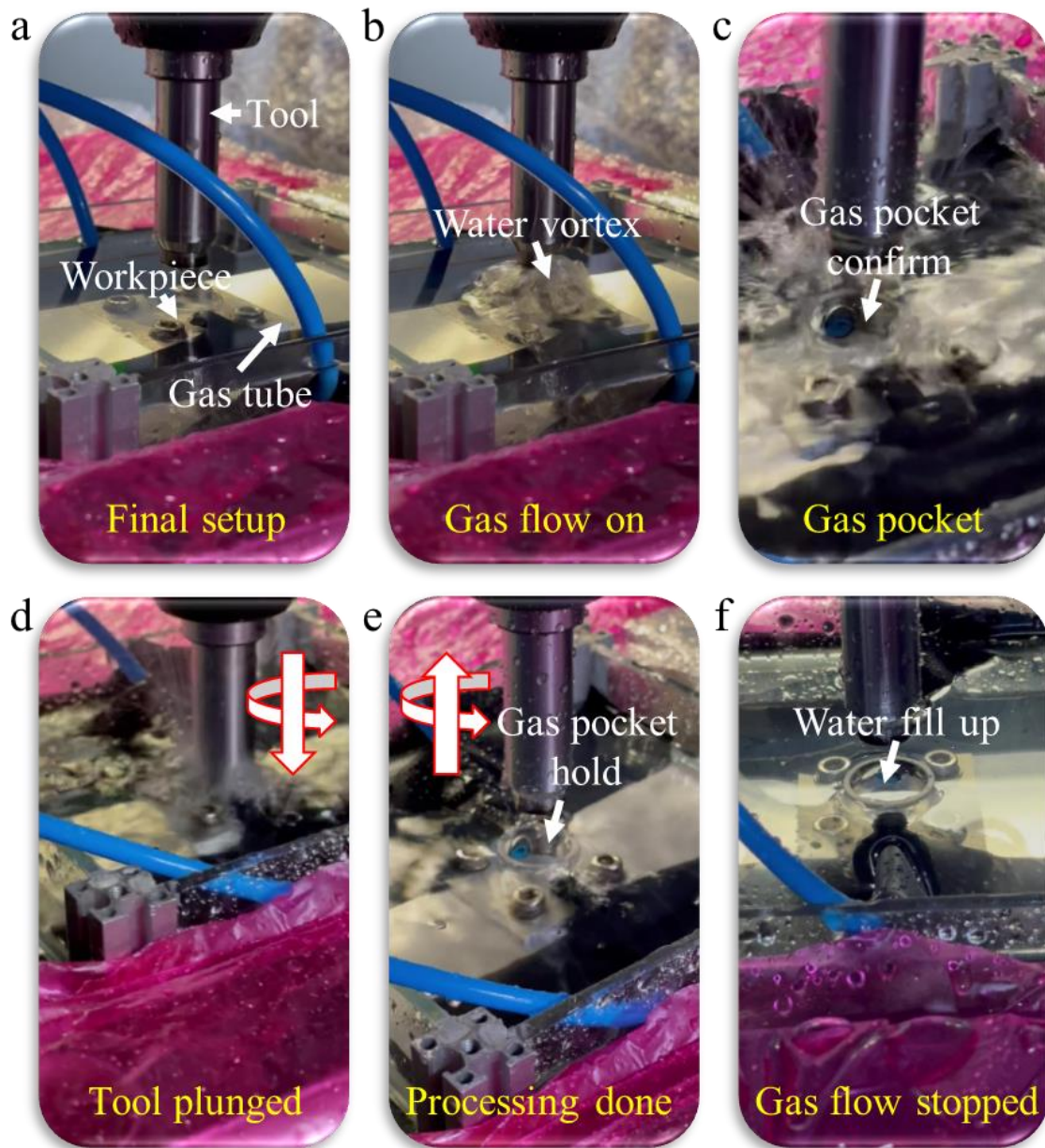


Figure 3.2 (a) The complete setup with the tank for GAFSSW, (b) water vortex began initiating gas flow, (c) gas pocket formed and enclosed with the adapter, (d) rotating tool plunged next to the workpiece, (e) tool extracted after welding. The gas pocket was held until the workpiece cooled down, (f) gas flow stopped, and water filled up inside the adapter.

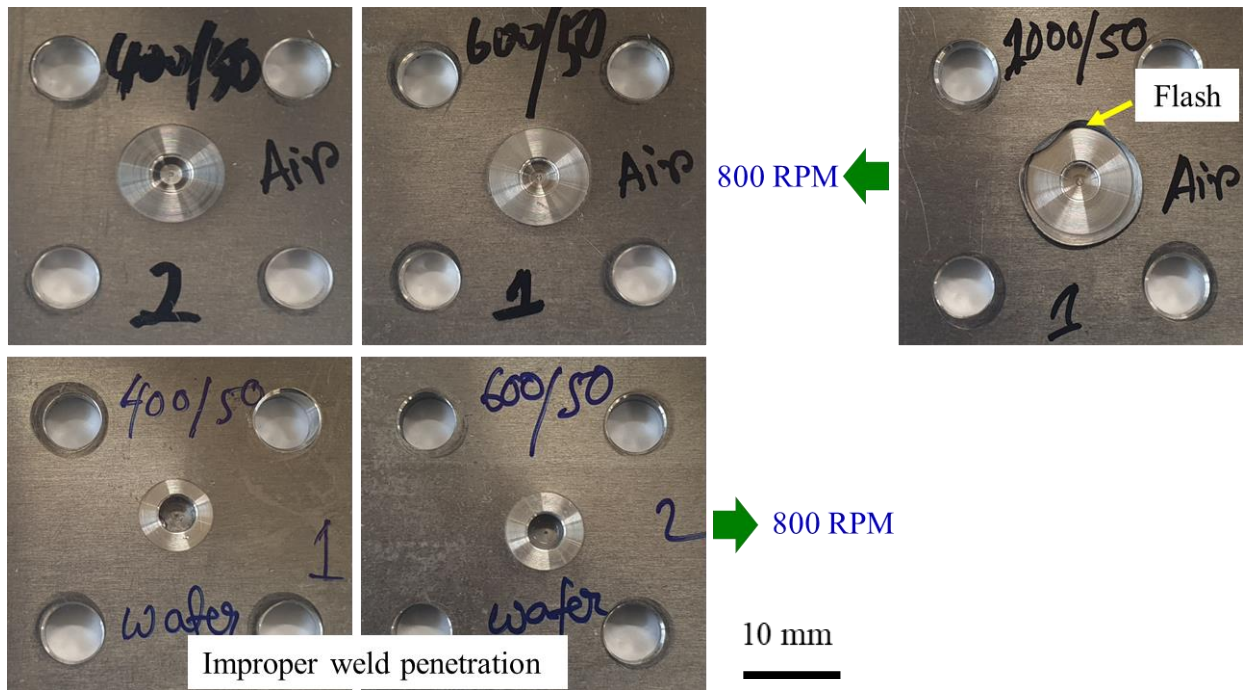


Figure 3.3 The process parameter optimization ways for GSAFSSW.

3.3 RESULTS AND DISCUSSION

3.3.1 Process responses and optical microscopy

The force and torque responses (Fig. 3.4(a, b)) for UFSSW are higher than those of FSSW and GAFSSW. This indicates strong mechanical deformation during the UFSSW, as the simulated seawater surrounded the tool and material. The force-torque responses for the GAFSSW technique appeared similar to FSSW. During the initial plunging of the tool into the material, there was a sharp rise in torque values (Fig. 3.4(b)), which decreased and stabilized to a certain depth (2.4 mm) and continued to increase as the process progressed. The tool stirring became most prominent when the torque increased again in the final stages of the processing. A reduction in torque value in the final stage of UFSSW indicates less material softening, where the material exhibits lower flowability compared to others [39,40]. The temperature profiles (Fig. 3.4(c)) represent the

maximum and minimum peak temperatures for FSSW (~249.5°C) and UFSSW (~150°C), respectively. Compared with FSSW, the lower peak temperature for UFSSW is primarily due to the higher heat transfer coefficient of seawater than air. On the other hand, the proposed GAFSSW technique achieved the peak temperature (~197°C) between FSSW and UFSSW. Despite having a higher peak temperature, GAFSSW showed faster cooling than UFSSW. This is due to the continuous flow of high-velocity Ar gas, revealing the nature of convective heat transfer from free (during UFSSW) to forced convection [41]. In contrast, seawater absorbs heat during UFSSW and heats up immediately through boiling heat transfer near the workpiece and tool interface [42]. The differences in process responses strongly impact the geometry of the welded regions, as shown in Fig. 3.5(a,a₁-c,c₁). The spot diameters (Table 3.3) of the welded regions differ along with the processing modes. In the case of FSSW and GAFSSW, the measurements are almost equal (~13 mm), whereas the spot diameter for UFSSW (~11 mm) measures the smallest. Moreover, UFSSW shows the maximum possible deformation at the bottom of the workpiece (Fig. 3.5(c₁)), which is not noticeable for FSSW and GAFSSW. The frictional heating was less for UFSSW. The material could not receive a sufficient plasticization temperature, stirring harder while pushing it down under compressive loading.

Table 3.3 Measured dimension of the welding region (spots)

Welding cond.	Spot diameter (mm)	Depth of SZ (D; mm)
FSSW	13	0.63
UFSSW	11	0.51
GAFSSW	12.8	0.82

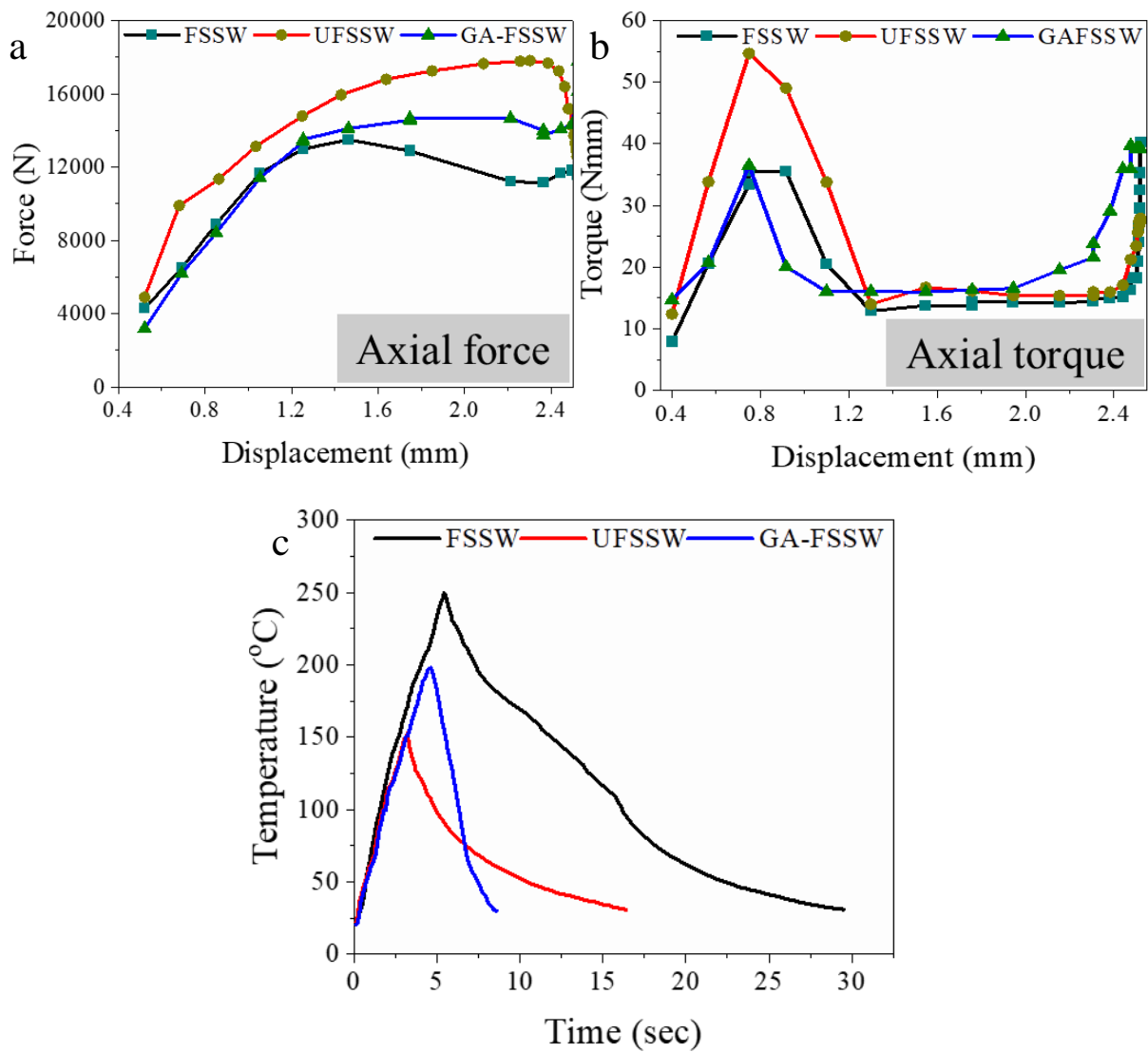


Figure 3.4 (a) Force, (b) torque, (c) temperature profiles for FSSW, UFSSW, and GAFSSW.

Optical micrographs (Fig. 3.6(a-c)) of the FSSW, UFSSW, and GAFSSW cross-sections represent a typical appearance, including SZ and TMAZ with the BM. The SZ depth (D) was measured at approximately 0.51 mm, 0.63 mm, and 0.82 mm for UFSSW, FSSW, and GAFSSW, respectively. For all three cases, in the merit of the FSW techniques, no such defects, including cold cracking and porosity, were observed throughout the micrographs of the weld cross-sections.

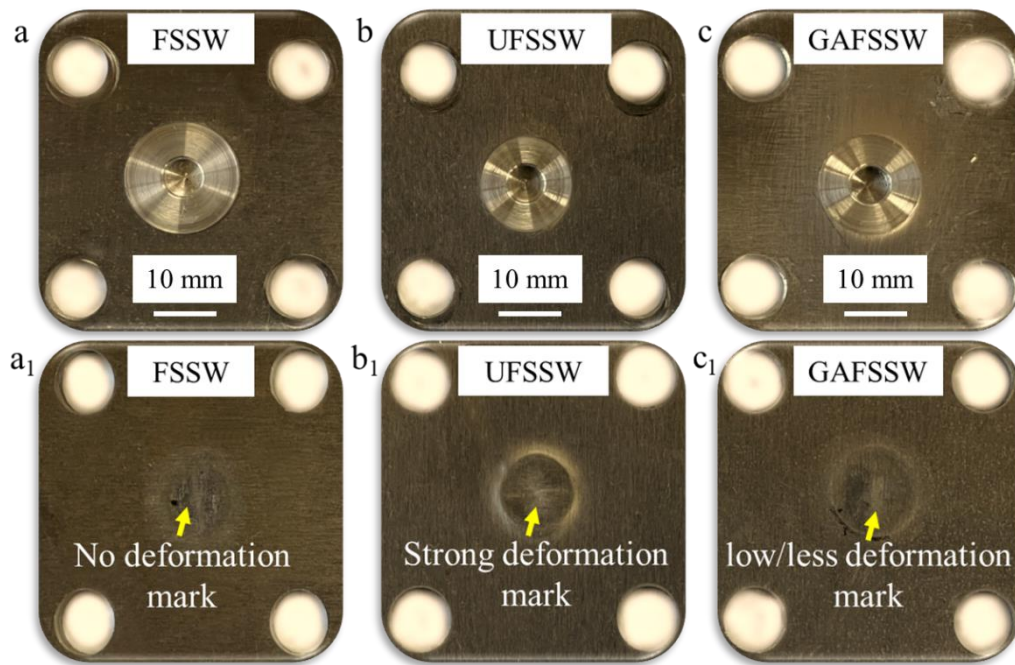


Figure 3.5 Top and bottom surface pictographs of (a, a₁) FSSW, (b, b₁) UFSSW, (c, c₁) GAFSSW.

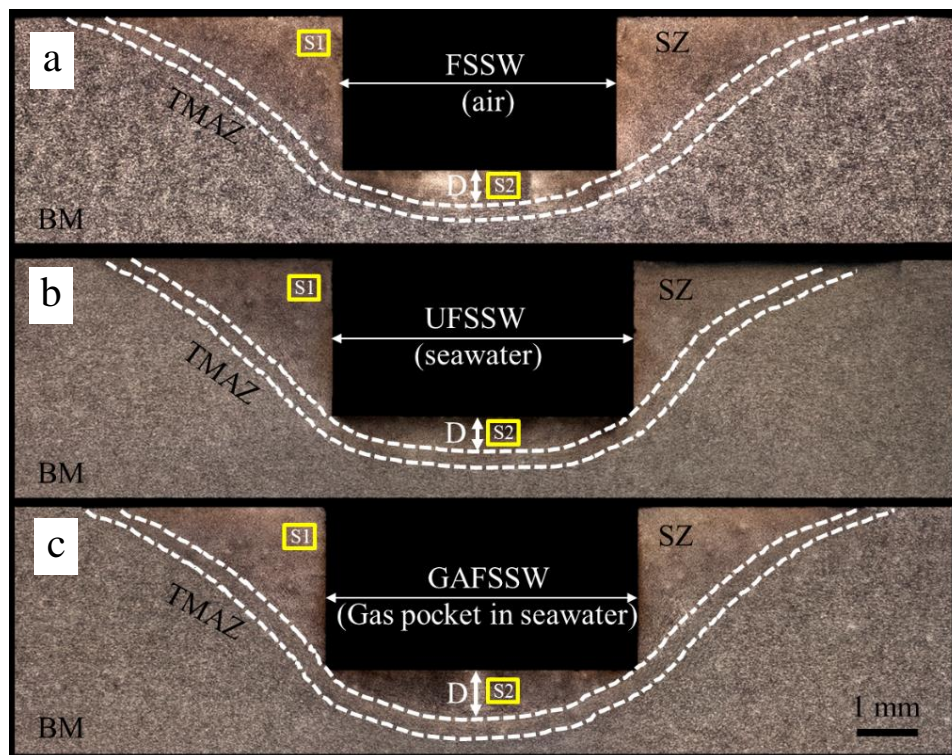


Figure 3.6 (a-c) Optical micrographs of the FSSW, UFSSW, and GAFSSW cross-sections.

3.3.2 SEM analysis on the top and cross-sections of the weld

The top surfaces of the UFSSW and GAFSSW specimens were examined under SEM followed by EDS chemical analysis to characterize the presence of Cl, as shown in Fig. 3.7(a-d). Elemental compositions of the EDS spectra confirm the presence of Cl (Fig. 3.7(c)) on the surface of UFSSW, whereas no evidence of Cl was found (Fig. 3.7(d)) for GAFSSW. In the case of UFSSW, the Cl ions enter the welded region because the workpiece was utterly exposed to the seawater. Hence, considering the benefit of the gas pocket formation, GAFSSW claims to remove Cl by repelling seawater from its weld region.

SEM analysis (Fig. 3.8(a-g)) on the cross-sections of the selected regions within the SZ (as marked in Fig. 3.6) shows the appearance of two types of precipitates differentiated by color. EDS point analysis followed by the area scanning confirmed white color precipitate (α) as $\text{Al}_6(\text{Fe}, \text{Mn})$ and Mg_2Si in black (β). The EDS area mapping (Fig. 3.9) on the BSE image of the S_2 region of the GAFSSW specimen displays that the elemental profiles of Si and Mg are overlaid to confirm the formation of Mg_2Si . Similarly, the elemental profiles of Fe, Mn matched with the Al phase profile, confirming another composition (Table 3.4) of $\text{Al}_6(\text{Fe}, \text{Mn})$. These two secondary phases act differently based on their characteristics. The α phase has a high energy non-coherent interface with Al, whereas the β phase has a comparatively lower energy semi-coherent interface, where the atoms are strongly connected to Al [43-45].

Table 3.4 Possible compositions of precipitates (at.%)

Precipitates	Al	Si	Mn	Mg	Fe
$\text{Al}_6(\text{Mn}, \text{Fe})$	88.37	-	2.94	-	8.69
Mg_2Si	-	63.49	-	36.51	-

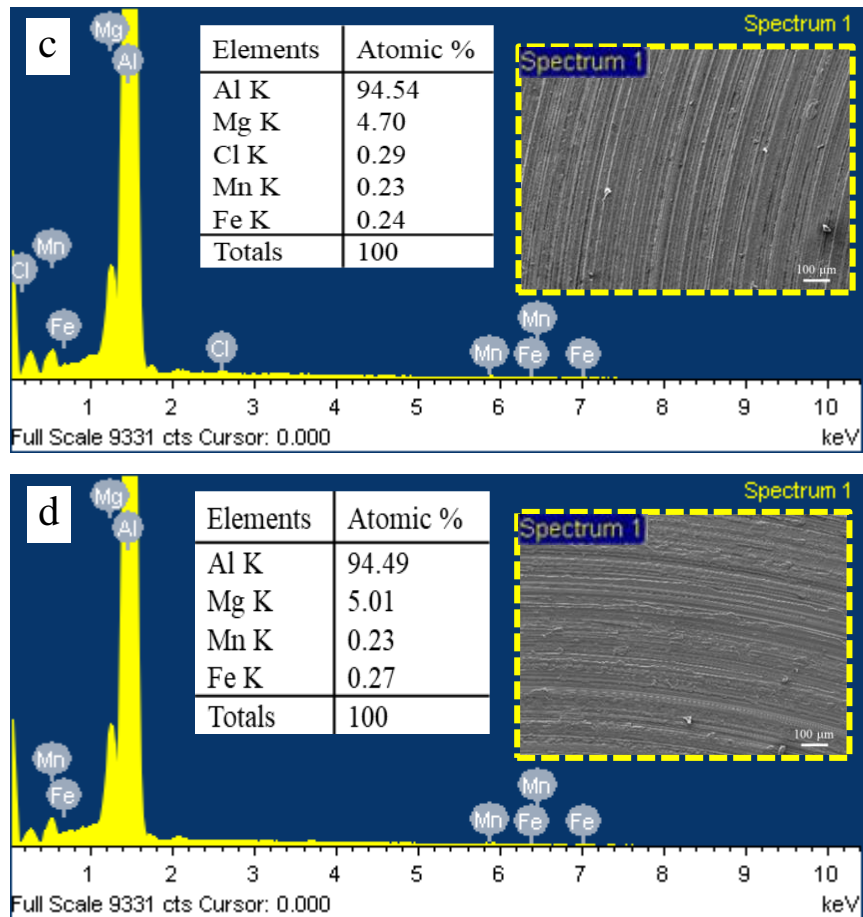
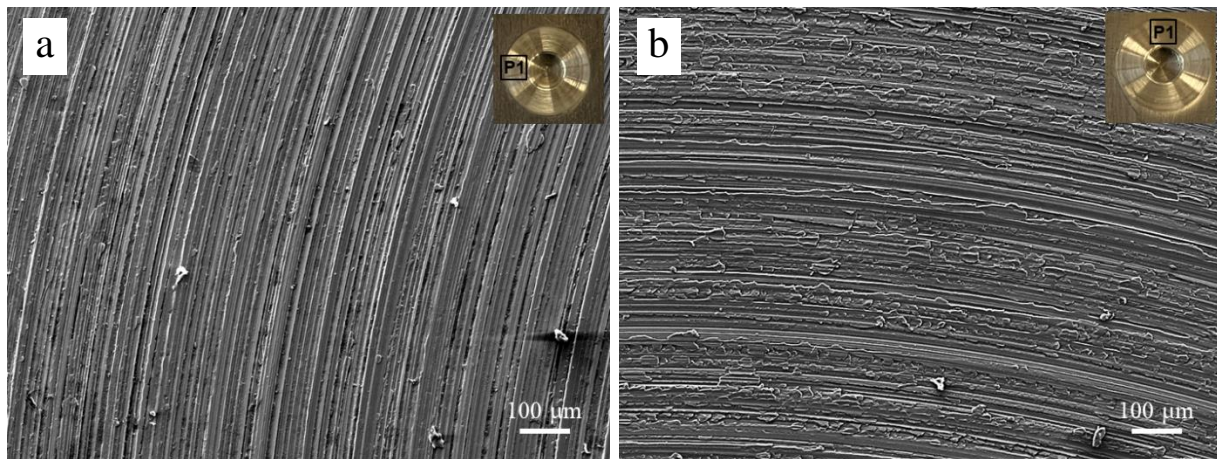


Figure 3.7 SEM image of the top surface of (a) UFSSW, (b) GAFSSW, (c, d) corresponding EDS spectra with elemental compositions.

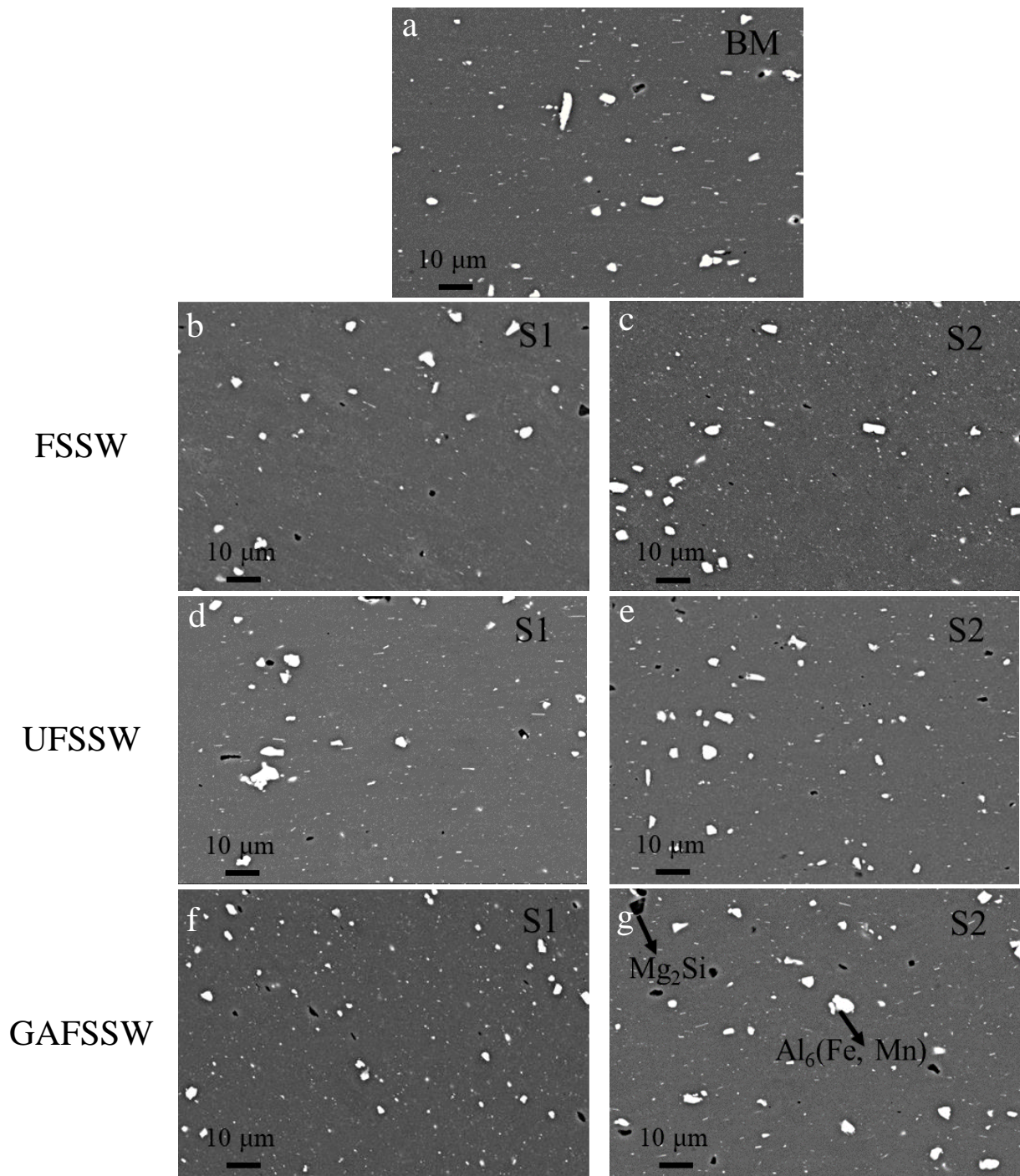


Figure 3.8 SEM images of the formation of the precipitate in (a) BM, S₁, and S₂ regions in the SZ of (b, c) FSSW, (d, e) UFSSW, and (f, g) GAFSSW.

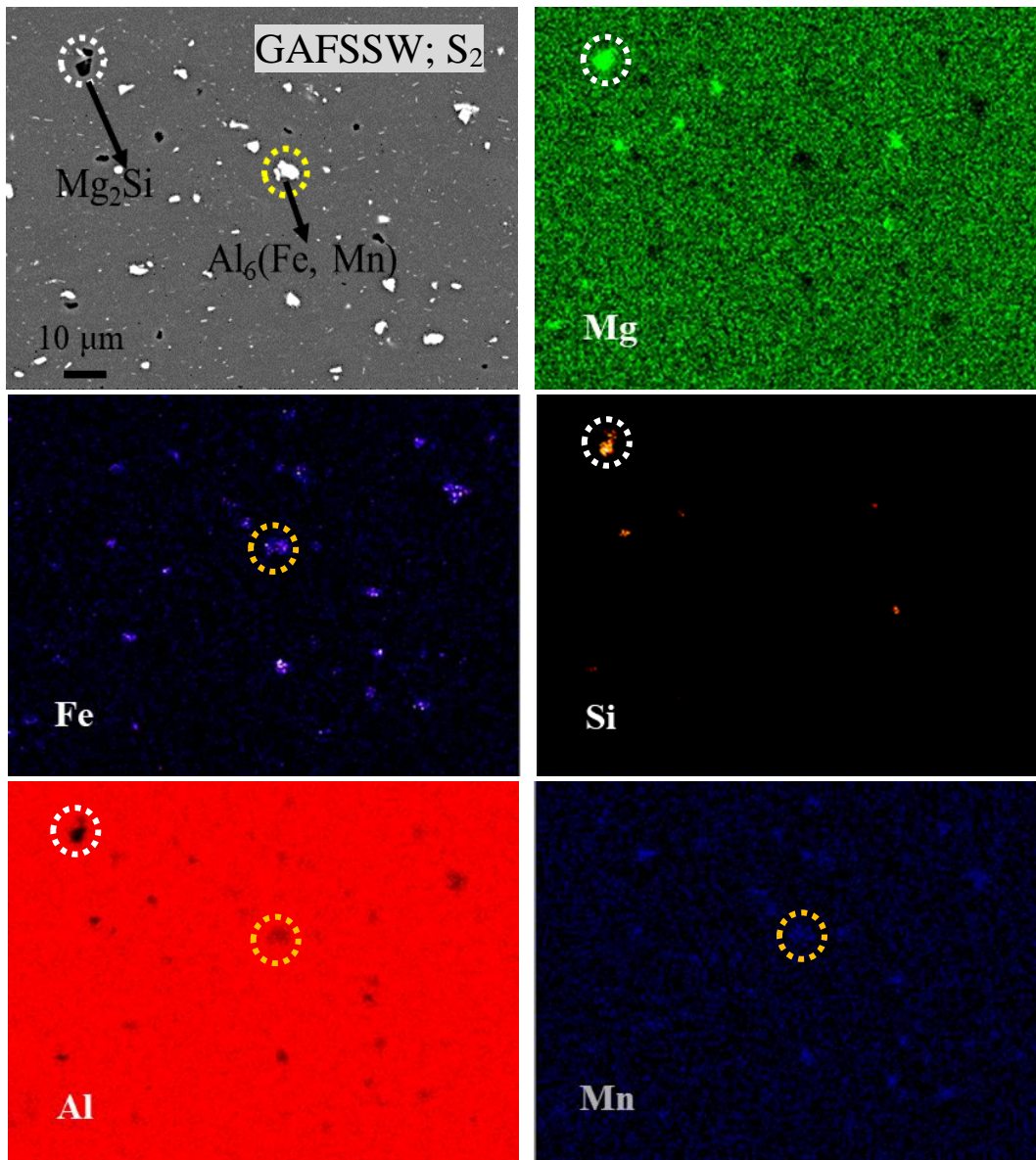


Figure 3.9 BSE image of GAFSSW (S₂) and their corresponding EDS chemical mapping of Mg, Fe, Si, Al, and Mn, respectively.

The average precipitate size and their distribution also vary since the welding conditions of FSSW, UFSSW, and GAFSSW are changed. A few large α phases are observed in BM, which breaks down into smaller particles by adequate straining through FSW. The pin-influenced region

(S₁) of the SZ of GAFSSW represents the most significant homogenous distribution of fine precipitates (Fig. 3.8(f)) with an average size of $0.66 \pm 0.50 \mu\text{m}$. The similar locations in FSSW (S₁) and UFSSW(S₁) correspondingly reveal an irregular distribution of the precipitates (Fig. 3.8(b, d)), with a few larger α particles in the range of $6.00 \pm 0.59 \mu\text{m}$ and $4.00 \pm 0.30 \mu\text{m}$. Heirani et al. [46] performed underwater FSW of AA 5083 alloy and found a few coarse precipitates similar to this recent observation. The variation in precipitate size and distribution is mainly due to the different heating and cooling rates, which differ from one process to another. Zeng et al. [47] made a similar observation on the FSP of Mg-Li-Al-Zn alloy in the presence of a liquid CO₂ medium. The precipitates were more refined than those with lesser cooling conditions. The present study found that GAFSSW takes only ~2.5 secs to cool down the sample from 150°C to 25°C, shorter than ~5 secs during UFSSW. Therefore, the higher cooling rate of the GAFSSW technique (Fig. 3.3(c)) with effective tool stirring inside the more plasticized material (compared to UFSSW) further controls the formation of fine and uniform precipitates within the SZ.

3.3.3 Microstructural analysis by EBSD

The IPF map of the BM shows (Fig. 3.10(a)) coarse-grained microstructure with an average grain size of $20.94 \pm 8.73 \mu\text{m}$, where most of the grain boundaries (93.80%) appear to be HAGBs, as shown in Fig. 3.11(a). This specifies a case of a highly recrystallized grain structure (98.50%) in the BM, as confirmed by the GOS map in Fig. 3.11(a1). The BM 5083, marked with grade H112, indicates thermal treatment at an elevated temperature after strain-hardened [48]. In addition, the average KAM value of 0.20 (Fig. 3.12(a)) also indicates low strains in the BM. Microstructures of the SZ (S₁ and S₂ in Fig. 3.5) of FSSW, UFSSW, and GAFSSW are examined, and the changes are more evident than the BM. These two regions are considered based on their locations where plastic deformation-induced material flow behavior differs significantly [49,50]. Irrespective of

the welding conditions, the S_1 sites of the SZ represent dynamically recrystallized fine-grained structures compared to BM. The IPF maps (Fig. 3.10(b-d)) of FSSW, UFSSW, and GAFSSW represent an average grain size of $4.23 \pm 1.56 \mu\text{m}$, $2.92 \pm 1.11 \mu\text{m}$, and $3.80 \pm 1.44 \mu\text{m}$, respectively. The GBCD maps of the similar regions show a higher proportion of HAGBs presence over the LAGBs, with 86.30% for FSSW (Fig. 3.11(b)), 70.80% for UFSSW (Fig. 3.11(d)), and 75.70% for GAFSSW (Fig. 3.11(f)). Likewise, the GOS maps show more dynamically recrystallized grain structures over the deformed grains, with the amount of recrystallization measured as 87.70%, 67.80%, and 73.00% for FSSW (Fig. 3.11(b₁)), UFSSW (Fig. 3.11(d₁)), and GAFSSW (Fig. 3.11(f₁)), respectively. A comparison of the KAM maps in Fig. 3.12(b-d) shows relatively higher strains in the case of the UFSSW (KAM_{avg} 0.43) than in the FSSW (KAM_{avg} 0.24) and GAFSSW (KAM_{avg} 0.28). The nature of the microstructures appears similar for S_2 , in contrast to some measurable differences in S_1 . The IPF maps represent (Fig. 3.10(b₁-d₁)) the average grain sizes of $3.44 \pm 1.31 \mu\text{m}$, $2.19 \pm 0.84 \mu\text{m}$, and $2.85 \pm 0.95 \mu\text{m}$ for FSSW, UFSSW, and GAFSSW, respectively. The GBCD and GOS maps of similar regions show the presence of 82.50%, 74.60%, and 80.80% HAGBs with the recrystallization amounts of 80.00%, 72.10%, and 78.80%, in the case of FSSW (Fig. 3.11(c-c₁)), UFSSW (Fig. 3.11(e-e₁)), and GAFSSW (Fig. 3.11(g-g₁)), individually. No significant changes are perceived in the KAM maps (Fig. 3.12(b₁-d₁)) of S_2 locations compared to S_1 for any of these three methods. The dominance of HAGBs in the SZs confirms the occurrence of CDRx through cross-slip dislocations, as the aluminum has high stacking fault energy that exhibits a high recovery rate against intense plastic deformation during processing [50,51]. Consequently, the average grain sizes of S_2 are smaller than S_1 due to variables in frictional heating caused by the tool-workpiece from the top of the SZ to its bottom [52].

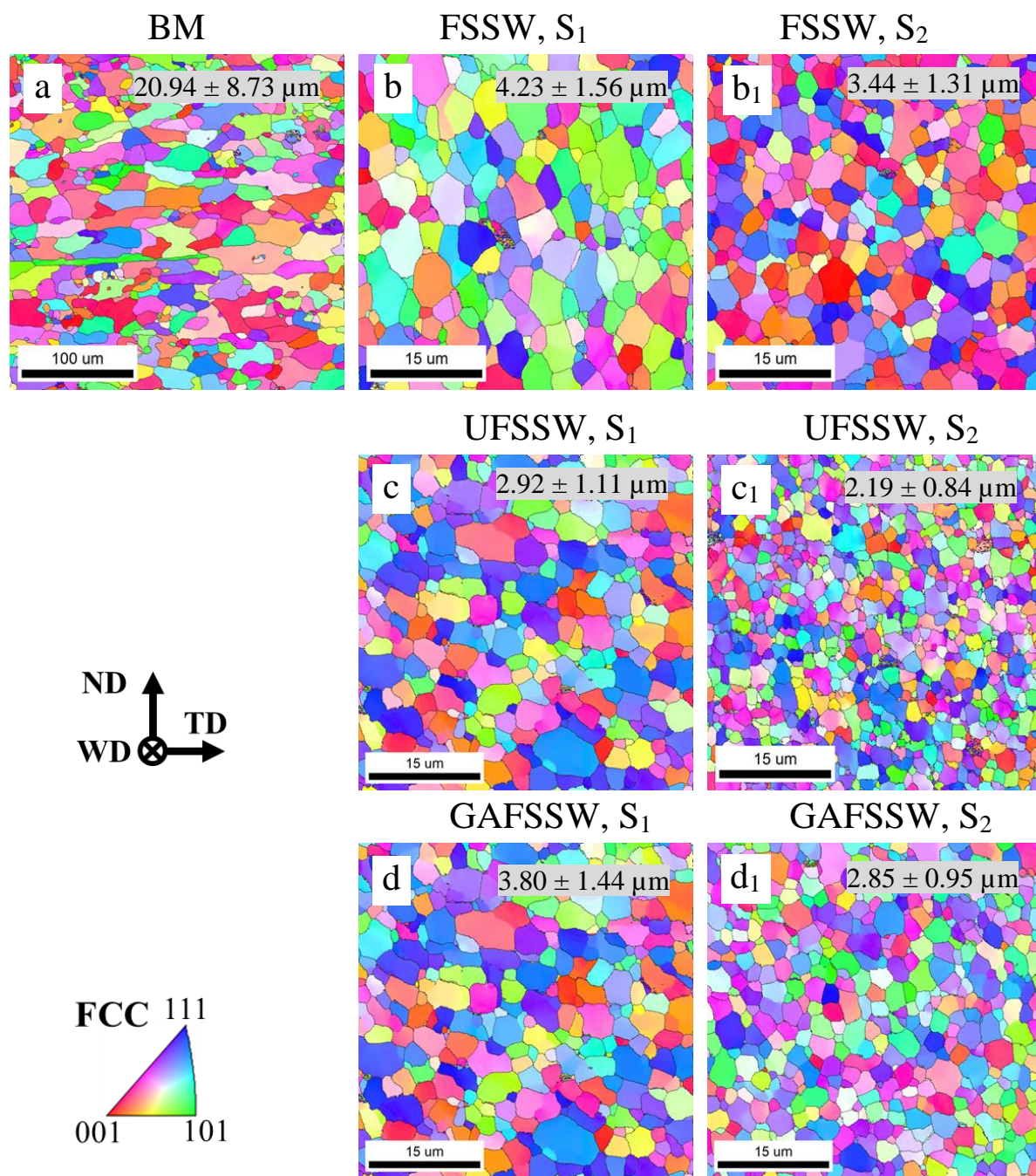


Figure 3.10 Microstructure analysis by EBSD generated IPF maps of (a) BM, (b-d) S₁, and (b₁-d₁) S₂ regions: (b-b₁) FSSW, (c-c₁) UFSSW, and (d-d₁) GAFSSW.

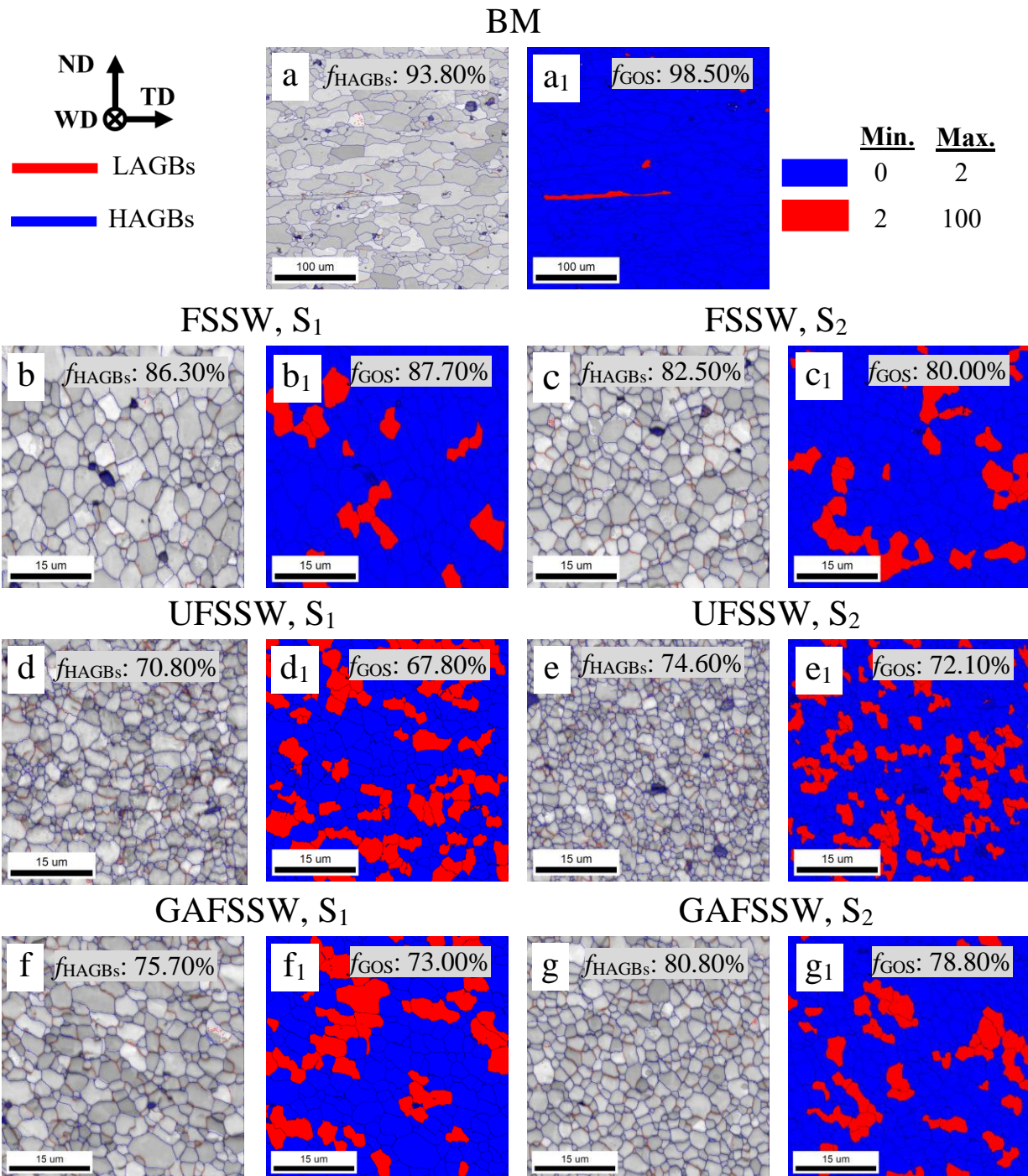


Figure 3.11 Grain boundary characteristics study by EBSD generated GBCD (a-g) and GOS (a₁-g₁) maps: (a-a₁) BM; (b-b₁), (d-d₁), (f-f₁) for the locations of S₁; (c-c₁), (e-e₁), (g-g₁) for the locations of S₂ for FSSW, UFSSW, and GAFSSW.

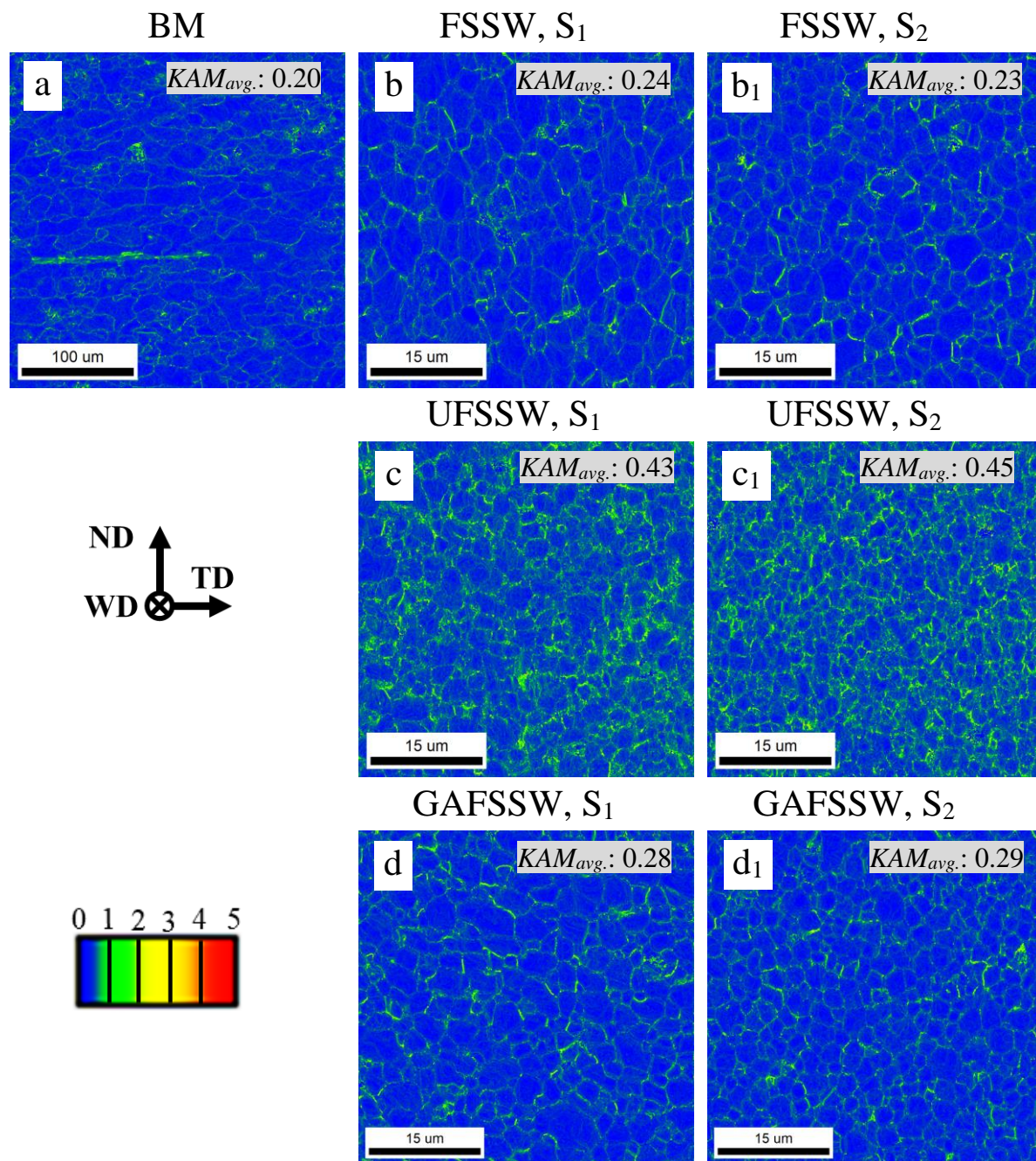


Figure 3.12 EBSD generated KAM maps of (a) BM, (b-b₁) S_1 and S_2 regions of FSSW, (c-c₁) for UFSSW, and (d-d₁) for GAFSSW.

Also, location S_2 experiences a shorter thermal cycle than S_1 , as the heat dissipates faster through the connection between the tank plate and the bottom of the workpiece [50]. Besides, precipitates and their heterogeneous distribution can impede grain boundary migration by particle-stimulated nucleation (PSN) during DRx, increasing the possibility of forming fine-grained structures in the SZ [53]. The amount of recrystallization also finds a minimum for UFSSW (S_1 and S_2) because the generated heat was insufficient. In comparison, GAFSSW appears to have a much more standardized grain refinement with the preferred recrystallization, as the peak temperature was between UFSSW and FSSW. Also, the amount of recrystallization increases at S_2 for UFSSW and GAFSSW compared to S_1 . The main reason for this observation is the generation of an enormous amount of strains during welding at lower peak temperatures with a higher cooling rate than FSSW, which further increases the chances of achieving a higher DRx through dynamic recovery [51]. Overall, the maximum average KAM value for UFSSW is primarily responsible for the occurrence of a large compressive force (Fig. 3.4(a)) during its processing [50,54].

3.3.4 Mechanical properties analysis

2D surface hardness maps on FSSW, UFSSW, and GAFSSW cross-sections were performed as depicted in Fig. 3.13. The area marked with a blue dashed line in the schematic micrograph in Fig. 3.13(a) represents the location for the hardness observation. As shown in Fig. 3.13(b-c), irrespective of the processing environments, the SZs of all three processed conditions showed higher surface hardness values than BM (75.80 ± 2.87). The GAFSSW showed higher average surface hardness (93.97 ± 4.78) than UFSSW (86.30 ± 3.93) and FSSW (83.47 ± 3.08). The improvement in surface hardness of all three SZs is governed by the presence of fine grain structures (Fig. 3.10) than BM. In addition, for the precipitation-hardened aluminum alloy, the presence of the secondary phases plays a crucial role in increasing the surface hardness through

solid-solution strengthening [51,55]. Although UFSSW has the smallest grain size, the improvements in hardness values for GAFSSW are mainly confined near the pin-influence area of the SZ. In the case of GAFSSW, the homogeneously dispersed fine precipitates (Fig. 3.8(f)) clog the dislocation motion and enhance the hardening effect in Al by the dispersion strengthening mechanism [56,57]. Hence, dispersion strengthening and grain refinement contribute to the fact that GAFSSW achieves the maximum average surface hardness in contrast to UFSSW and FSSW.

To understand the overall improvement in the mechanical properties of the process regions, tensile properties obtained from the indentation tests were comparatively analyzed. The indentation test locations on the cross-section of the individually processed specimen are illustrated in Fig. 3.14(a). The indentation tests were performed using eight load-unload cycles considering a maximum indentation depth of 8 μm to obtain a set of typical stress and strain values from each unload curve according to the standard procedure [58]. The load (L) – depth (H) curves corresponding to their stress-strain curves are merged in the case of the S1 and S2 regions of FSSW, UFSSW, and GAFSSW, as presented in Fig. 3.14(b-e). The merged L - H curves for both the sites (S₁, S₂) show a considerable improvement in the maximum loading parallel to the indentation depths (Fig. 14(b, d)) for UFSSW and GAFSSW than the FSSW, which is also reflected in their respective stress-strain curves in Fig. 3.14(c, e). The maximum loading/stress for each case is slightly higher in the case of S₂ compared to S₁. These differences are possibly due to the heterogeneous microstructures caused by the asymmetric tool stirring along the material thickness [50]. The improvement in maximum bearable load with tensile properties of UFSSW and GAFSSW compared to FSSW was mainly due to the differences in grain sizes. The differences in the tensile strength of UFSSW and GAFSSW are very close, as the indentation test sites have nearly similar hardness (green color), as seen in Fig. 3.13(b, d).

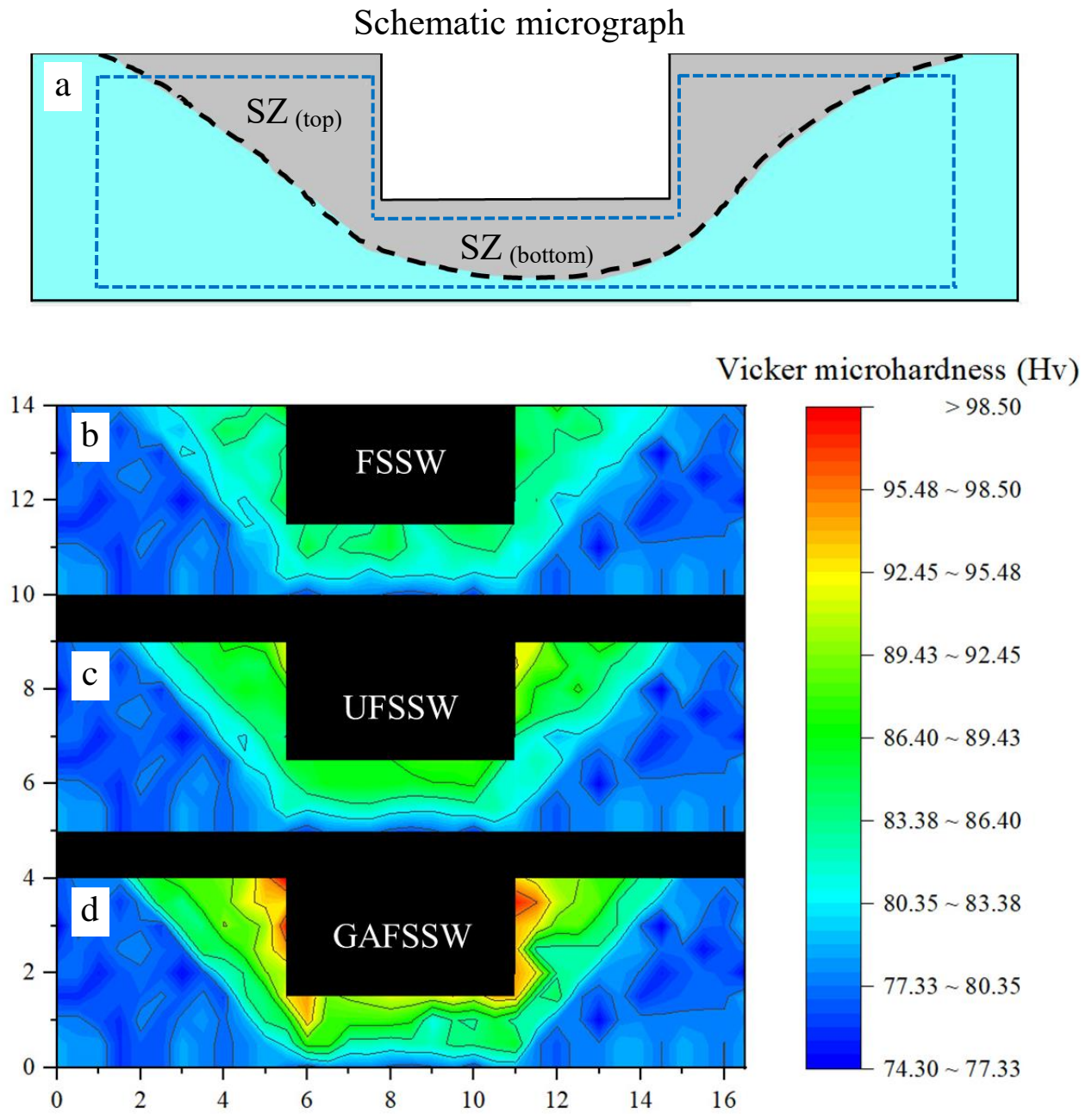


Figure 3.13 (a) Schematic micrograph of the weld cross-section indicating the location for microhardness measurements, 2D surface microhardness map for (b) FSSW, (c) UFSSW, and (d) GAFSSW weld cross-sections.

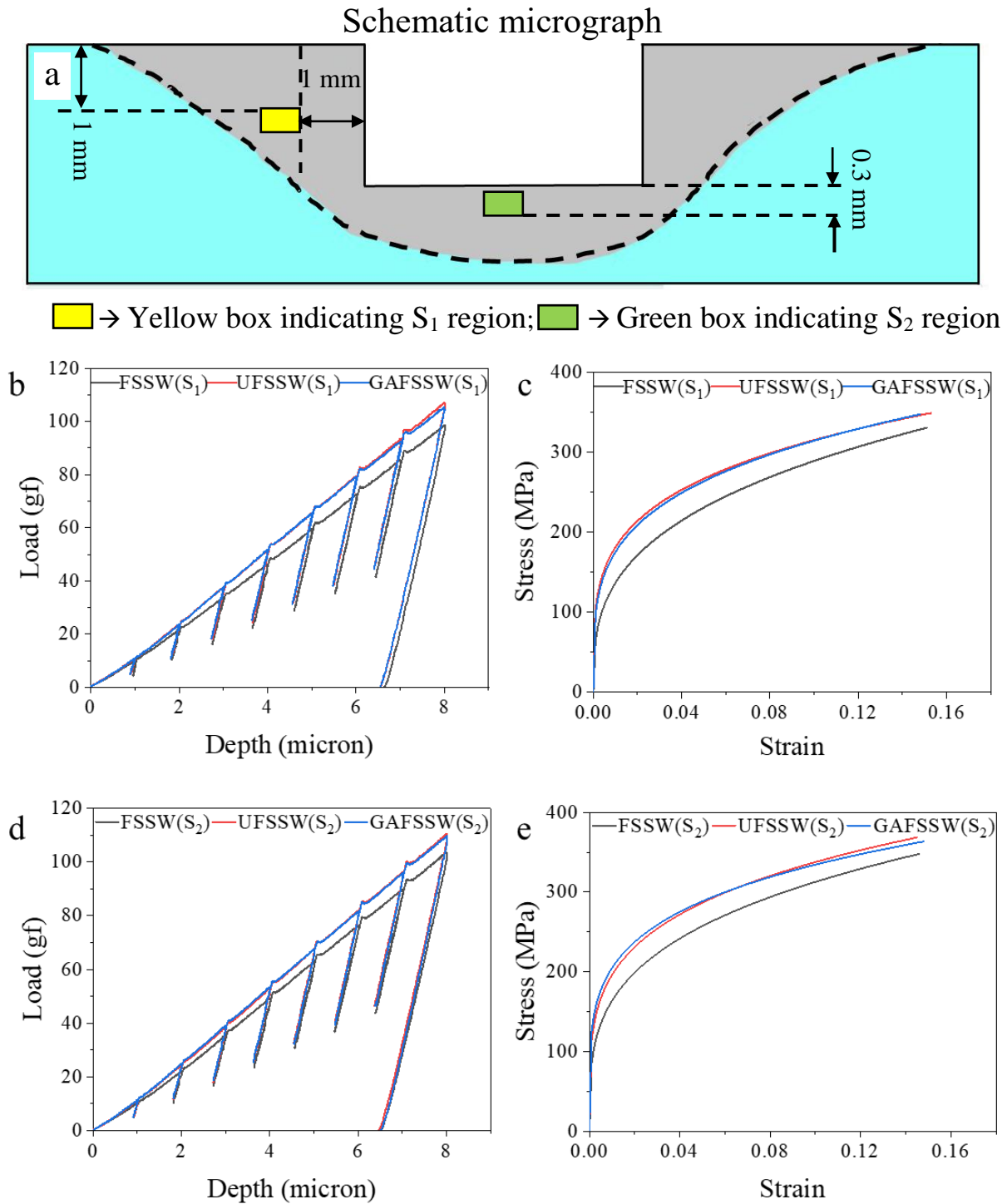


Figure 3.14 (a) Schematic micrograph of the weld cross-section indicating the locations for indentation tests, L - H curves, and stress-strain curves for (b, c) S_1 and (d, e) S_2 locations obtained from the SZ of FSSW, UFSSW, and GAFSSW weld cross-sections.

3.3.5 Corrosion properties analysis

OCP measurements for all the samples were performed by immersing the samples in the electrolyte solution with no current applied to the system. Before the potentiodynamic polarization tests, the trends of the OCP values over time are shown in Fig. 3.15(a). The OCP of the BM increased steadily from an initial value of -0.849 V to -0.754 V in 60 min, with an average value of -0.751 V over the last 1 min. In the case of the FSSW, there was an initial drop in OCP from -0.955 V to -0.982 V in 5 min, then gradually increased again and became stable at -0.871 V at the last minute. For UFSSW, the OCP values first decreased from -0.822 V to -0.895 V within the first 23 min and finally increased to -0.849 V and remained stable for the rest of the measurement. But for GAFSSW, a similar trend to the FSSW was observed, as the OCP dropped from -0.869 V to -0.920 V in the first 9 min and then became stable with a steady rise to -0.794 V. The initial decrease of the OCP values for FSSW, UFSSW, and GAFSSW suggests anodic behaviors. This indicates that the corrosion product was formed initially when the material surface came in contact with the electrolyte solution [59]. Further, the corrosion products deposited to form the protective layer on the material surface hinder the movement of ions, which helps to increase the potential at the next.

Once the OCP became stable, electrochemical polarization tests were performed on each sample to analyze the corrosion properties, mainly using corrosion potential values (E_{corr}) and corrosion current density (i_{corr}). The corrosion rate (CR) of each case was then calculated in millimeters per year (mm/yr) by the following equation [60]:

$$\text{CR} = \frac{I_{\text{corr}}KEW}{DA} \quad (1)$$

where $\frac{I_{\text{corr}}}{A} = i_{\text{corr}}$ the corrosion current density in $\mu\text{A}/\text{cm}^2$, K is a constant with a value of $3.27 \times 10^{-3} \text{ mm g}/\mu\text{A cm yr}$, EW and D are the equivalent weights and densities (g/cm^3) of the samples, respectively.

The representative plot of the potentiodynamic polarization curves of each sample, including BM, is shown in Fig. 3.15(b). The average values of the corrosion data obtained from the four polarization tests of the individual sample are presented with the standard deviations in Table 3.5. Furthermore, the average values of E_{corr} with standard deviations for each case are plotted concerning CR in Fig. 3.15(c).

Table 3.5 Corrosion parameters obtained from the polarization curves

Samples	E_{corr} (V/SCE)	i_{corr} ($\mu\text{A}/\text{cm}^2$)	CR (mm/yr)
BM	-0.974 ± 0.122	2.054 ± 0.574	0.024 ± 0.006
FSSW	-0.930 ± 0.026	1.786 ± 0.457	0.019 ± 0.005
UFSSW	-0.898 ± 0.029	4.595 ± 1.887	0.051 ± 0.024
GAFSSW	-0.860 ± 0.028	1.303 ± 0.584	0.014 ± 0.007

As seen in Fig. 3.15(c), the average E_{corr} values for all three cases appear higher than the BM. Among those, GAFSSW reveals maximum E_{corr} with a difference of 104 mV from the BM. The increase of E_{corr} towards nobler indicates a higher corrosion resistance due to the grain refinement, leading to an improved passive film formation on the processed surfaces compared to BM [61-63]. However, the overall corrosion rate depends on the breakdown of the passive layer by a certain amount of i_{corr} with the formation of pits. Thus, the minimum value of i_{corr} for GAFSSW is the primary reason for the lowest corrosion rate among others. Contrarily, the corrosion rate of UFSSW appears maximum with its maximum i_{corr} , although it has a higher E_{corr} than BM. The novelty of the GAFSSW technique includes driving out the seawater from its processed region, giving the surface an additional advantage against corrosion since there is no Cl accumulation, unlike UFSSW. Besides, compared to BM and others, the microstructural changes

for GAFSSW play an essential role in its highest corrosion resistance. The preferential stirring and recrystallization in the grain structures with the formation of very fine precipitates improve the corrosion resistance in Al for GAFSSW [63]. Due to the shearing effect of the tool and the plastic deformation inside the material, these particles are usually broken down, so they cannot act as local cathodes. As a result, the broken fine precipitates prevent the attack of corrosive species on the passive layer formed [64]. A similar observation was made by Chung et al. [65] in the effect of equal channel angular pressing on the corrosion properties of Al alloys. UFSSW experienced more drastic grain refinements than GAFSSW. However, this is mainly due to the lowest peak temperature during processing. Therefore, the grain structures are comparatively more deformed than in the GAFSSW. Also, the limited stirring with the strong compressive force (as previously discussed in section 3.1) promotes higher local strains (as noticed in Fig. 12 (c,c₁)) for UFSSW compared to GAFSSW and FSSW. This limited amount of stirring also restricts the formation of finer precipitates (as seen in Fig. 8(d)) for UFSSW. Hence, the grain size is not a good metric of the corrosion resistance of UFSSW as there is also the presence of coarser secondary phases, which can act as a local cathode to initiate the localized attack on its surface [63]. Also, pre-existing Cl in its processed region could result in poor corrosion resistance, especially pitting. Thus, the overall processing difference with possible microstructural changes for GAFSSW appears to possess excellent corrosion properties, which is a step ahead of UFSSW.

Emphasis on various findings and analyses of GAFSSW, it can be recommended that the merit of this technology can be adopted as an advanced technique in structural installation and maintenance for the subsea industry. For example, a custom-made FSW robot system, named FSW-BOT, is schematically designed to demonstrate the feasibility of the GAFSSW in the actual scenario. Figure 3.16(a) shows the FSW-BOT engaging the desired location of the workpiece using

the O-ring. After successfully setting up the FSW-BOT at the desired location, gas plunging begins through plug 1 to form the gas pocket while the seawater drives out through plug 2, as shown in Fig. 3.16(b). GAFSSW can then be applied locally to complete the required activities without the corrosive environment, seawater.

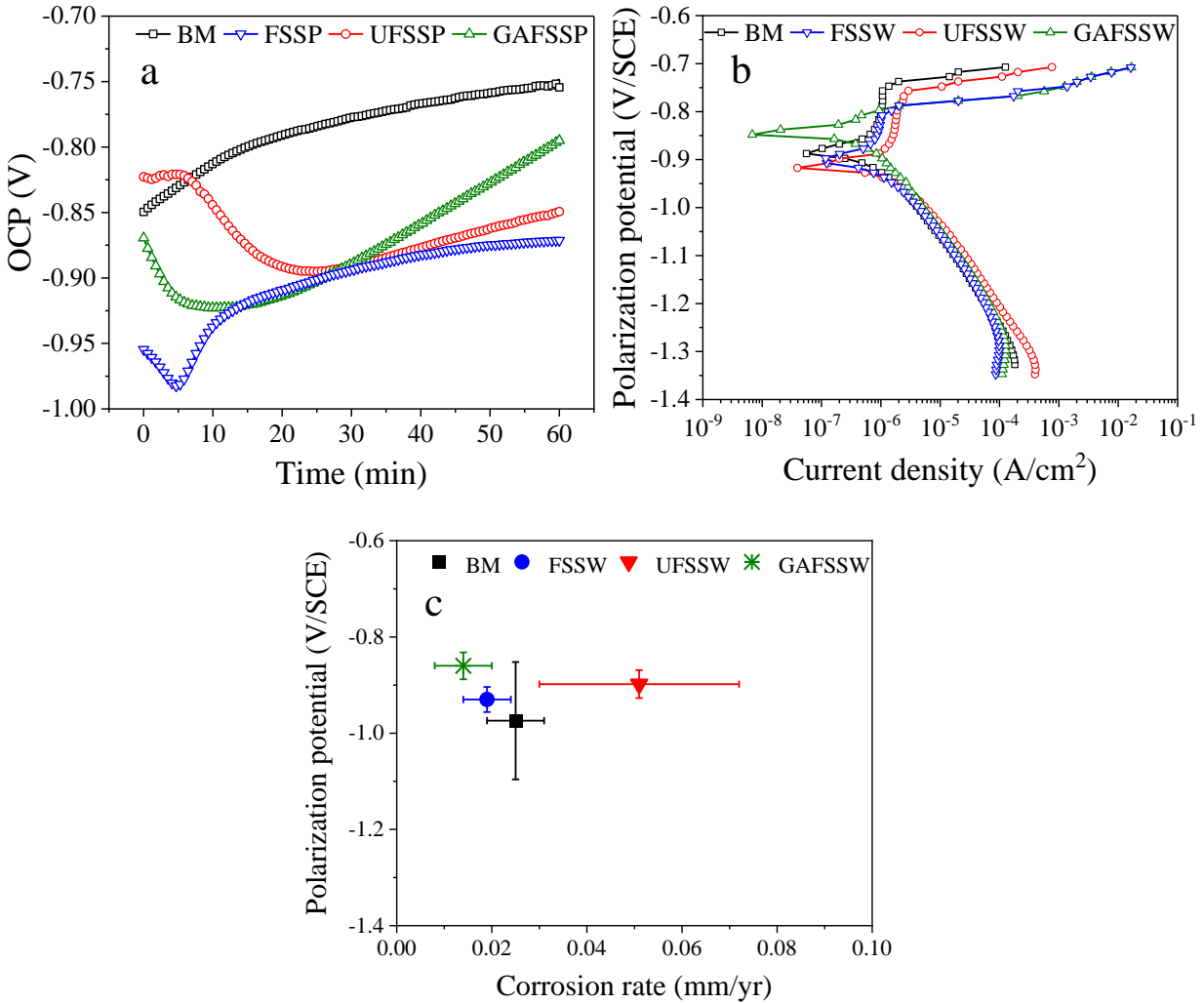


Figure 3.15 (a) OCP curves concerning time and (b) electrochemical potentiodynamic polarization curves of the tested samples, (c) avg. E_{corr} vs. CR plot, data obtained from potentiodynamic polarization curves of BM, FSSW, UFSSW, and GAFSSW.

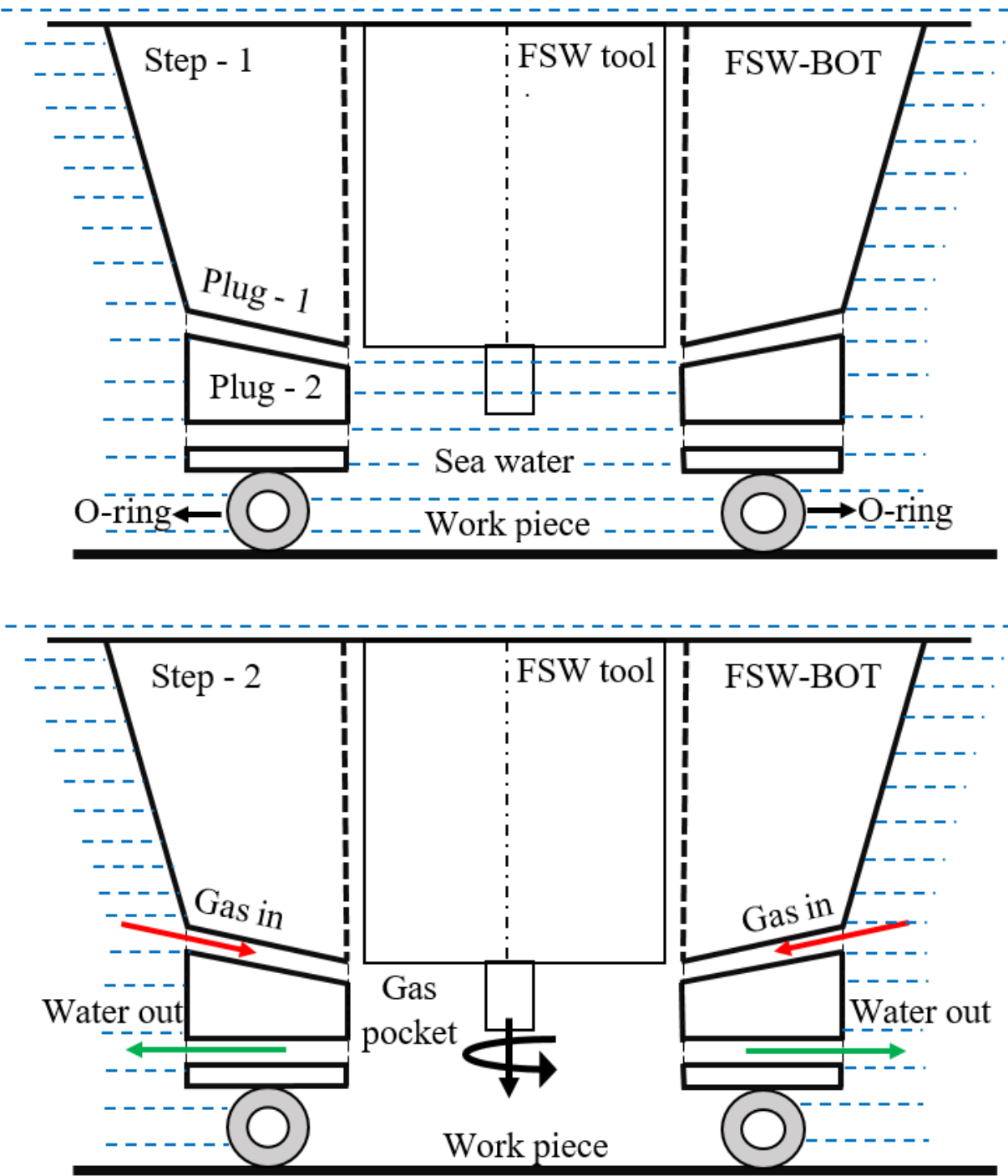


Figure 3.16 Schematic representation of GAFSSW operation in the sea (a) Step - 1: FSW-BOT set up, (b) Step - 2: welding with the gas pocket on the desired location of the workpiece.

3.4 CONCLUSIONS

The novelty of the GAFSSW technique was successfully established in view of recent developments with UWW techniques for subsea industries. In addition, forming a stable Ar gas pocket helped GAFSSW control its thermal cycle and achieve the peak temperature between UFSSW and FSSW. The SEM/EDS analysis confirmed the presence of Cl for UFSSW, while it was not identified for GAFSSW. SEM images of the selected regions in the SZs of FSSW, UFSSW, and GAFSSW revealed the formation of two types of precipitates, $Al_6(Fe, Mn)$ and Mg_2Si . Most importantly, the distribution and size of the precipitates were uniform and finest in the case of GAFSSW. IPF maps of the SZs of all three processed conditions showed dynamically recrystallized finer grain structures than the BM. The grain size for GAFSSW appeared a bit coarser than UFSSW but finer than FSSW. The presence of the finest precipitates caused dispersion strengthening along with grain refinement and helped GAFSSW achieve the maximum average surface hardness and overall mechanical strength. Electrochemical polarization tests showed that the GAFSSW specimen has the lowest corrosion rate, followed by FSSW, BM, and UFSSW.

REFERENCES

1. J. Tomków, D. Fydrych, G. Rogalski, Dissimilar underwater wet welding of HSLA steels, *Int. J. Adv. Manuf. Technol.* 109 (2020) 717–725.
<https://doi.org/10.1007/s00170-020-05617-y>
2. J. Łabanowski, Development of under-water welding techniques, *Weld. Int.* 25 (2011) 933-937. <https://doi.org/10.1080/09507116.2010.540847>
3. K.R. Carpenter, P. Dissanayaka, Z. Sterjovski, H. Li, J. Donato, A.A. Gazder, S.V. Duin, D. Miller, M. Johansson, The effects of multiple repair welds on a quenched and tempered steel for naval vessels, *Weld. World* 65 (2021) 1997–2012.
<https://doi.org/10.1007/s40194-021-01150-y>
4. S.T. Kandukuri, K.G. Robbersmyr, H.R. Karimi, Towards farm-level health management of offshore wind farms for maintenance improvements, *Int. J. Adv. Manuf. Technol.* 83 (2016) 1557–1567. <https://doi.org/10.1007/s00170-015-7616-y>
5. X. Wei, Z. Wen, L. Xiao, C. Wu, Review of fatigue assessment approaches for tubular joints in CFST trusses, *Int. J. Fatigue* 113 (2018) 43-53.
<https://doi.org/10.1016/j.ijfatigue.2018.04.007>
6. C. Xing, C. Jia, Y. Han, S. Dong, J. Yang, C. Wu, Numerical analysis of the metal transfer and welding arc behaviors in Underwater Flux-cored Arc Welding, *Int. J. Heat Mass Transf.* 153 (2020) 119570. <https://doi.org/10.1016/j.ijheatmasstransfer.2020.119570>
7. J. Tomków, D. Fydrych, K. Wilk, Effect of electrode waterproof coating on quality of underwater wet welded joints, *Materials* 13 (2020) 2947.
<https://doi.org/10.3390/ma13132947>
8. S.G. Parshin, Underwater wet FCA-welding of high-strength steel X70 through the use of flux-cored electrode, *Weld. Int.* 34 (2020) 24-28.
<https://doi.org/10.1080/09507116.2021.1918470>
9. C. Xu, N. Guo, X. Zhang, H. Chen, Y. Fu, L. Zhou, Internal characteristic of droplet and its influence on the underwater wet welding process stability, *J. Mater. Process. Technol.* 280 (2020) 116593. <https://doi.org/10.1016/j.jmatprotec.2020.116593>
10. P. Wei, H. Li, J. Liu, S. Li, Y. Zhang, Q. Zhu, Y. Lei, The effect of water environment on microstructural characteristics, compositional heterogeneity and microhardness distribution of 16Mn/304L dissimilar welded joints, *J. Manuf. Process.* 56 (2020) 417-427.
<https://doi.org/10.1016/j.jmapro.2020.05.006>

11. T. Schaupp, W. Ernst, H. Spindler, T. Kannengiesser, Hydrogen-assisted cracking of GMA welded 960 MPa grade high-strength steels, *Int. J. Hydrog. Energy* 45 (2020) 20080-20093. <https://doi.org/10.1016/j.ijhydene.2020.05.077>
12. D. Fydrych, J. Łabanowski, An experimental study of high-hydrogen welding processes, *Rev. Metal.* 51 (2015) e055. <http://dx.doi.org/10.3989/revmetalm.055>
13. J. Tomków, J. Łabanowski, D. Fydrych, G. Rogalski Cold cracking of s460n steel welded in water environment, *Pol. Marit. Res.* 25 (2018) 131-136. <https://doi.org/10.2478/pomr-2018-0104>
14. H. Chen, N. Guo, C. Liu, X. Zhang, C. Xu, G. Wang, Insight into hydrostatic pressure effects on diffusible hydrogen content in wet welding joints using in-situ X-ray imaging method, *Int. J. Hydrog. Energy* 45 (2020) 10219-10226. <https://doi.org/10.1016/j.ijhydene.2020.01.195>
15. J. Wang, Q. Sun, S. Hou, T. Zhang, P. Jin, J. Feng, Dynamic control of current and voltage waveforms and droplet transfer for ultrasonic-wave-assisted underwater wet welding, *Mater. Des.* 181 (2019) 108051. <https://doi.org/10.1016/j.matdes.2019.108051>
16. P.H.R. Menezes, E.C.P. Pessoa, A.Q. Bracarense, Comparison of underwater wet welding performed with silicate and polymer agglomerated electrodes, *J. Mater. Process. Technol.* 266 (2019) 63-72. <https://doi.org/10.1016/j.jmatprotec.2018.10.019>
17. S. Yasinta, J. Triyono, N. Muhayat, Y.C.N. Saputro, Effect of water depth and water flow on the physics and mechanic properties of underwater wet welded low carbon steel with post weld heat treatment, *AIP Conf. Proc.* 2217 (2020) 030093. <https://doi.org/10.1063/5.0000658>
18. X. Zhang, E. Ashida, S. Shono, F. Matsuda, Effect of shielding conditions of local dry cavity on weld quality in underwater Nd:YAG laser welding, *J. Mater. Process. Technol.* 174 (2006) 34–41. <https://doi.org/10.1016/j.jmatprotec.2004.12.009>
19. J. Zhu, J. Gao, A. Ehn, M. Aldén, Z. Li, D. Moseev, Y. Kusano, M. Salewski, A. Alpers, P. Gritzmant, M. Schwenk, Measurements of 3D slip velocities and plasma column lengths of a gliding arc discharge, *Appl. Phys. Lett.* 106 (2015) 044101. <https://doi.org/10.1063/1.4906928>
20. P.S. De, R.S. Mishra, Friction stir welding of precipitation strengthened aluminum alloys: scope and challenges, *Sci. Technol. Weld. Join.* 16 (2011) 343-347. <https://doi.org/10.1016/j.msar.2005.07.001>

21. R. Nandan, T. Debroy, H.K.D.H. Bhadeshia, Recent advances in friction-stir welding – Process, weldment structure and properties, *Prog. Mater. Sci.* 53 (2008) 980–1023. <https://doi.org/10.1016/j.pmatsci.2008.05.001>
22. K. Gao, S. Zhang, M. Mondal, S. Basak, S.T. Hong, H. Shim, Friction Stir Spot Butt Welding of Dissimilar S45C Steel and 6061-T6 Aluminum Alloy, *Metals* 11 (2021) 1252. <https://doi.org/10.3390/met11081252>
23. J. Li, M. Su, W. Qi, C. Wang, P. Zhao, F. Ni, K. Liu, Mechanical property and characterization of 7A04-T6 aluminum alloys bonded by friction stir welding, *J. Manuf. Process.* 52 (2020) 263-269. <https://doi.org/10.1016/j.jmapro.2020.02.018>
24. Y.B. Tan, X.M. Wang, M. Ma, J.X. Zhang, W.C. Liu, R.D. Fu, S. Xiang, A study on microstructure and mechanical properties of AA3003 aluminum alloy joint by underwater friction stir welding, *Mater. Charact.* 127 (2017) 41–52. <https://doi.org/10.1016/j.matchar.2017.01.039>
25. H.A. Derazkola, E. Garcia, M. Elyasi, Underwater friction stir welding of PC: experimental study and thermo-mechanical modelling, *J. Manuf. Process.* 65 (2021) 161-173. <https://doi.org/10.1016/j.jmapro.2021.03.034>
26. K. Mori, N. Bay, L. Fratini, F. Micari, A.E. Tekkaya, Joining by plastic deformation, *CIRP Ann. Manuf. Technol.* 62 (2013) 673–694. <https://doi.org/10.1016/j.cirp.2013.05.004>
27. B. Sutton, K. Ross, G. Grant, G. Cannell, G. Frederick, R. Couch, Friction Stir Processing of Degraded Austenitic Stainless Steel Nuclear Fuel Dry Cask Storage System Canisters, In: X. Liu et al. (eds.) *Energy Materials 2017. The Minerals, Metals & Materials Series*, Springer, Cham. https://doi.org/10.1007/978-3-319-52333-0_31
28. E.P. Silva, D.R. Leiva, H.C. Pinto, R. Floriano, A.M. Neves, W.J. Botta, Effects of friction stir processing on hydrogen storage of ZK60 alloy, *Int. J. Hydrog. Energy* 43 (2018) 11085-11091. <https://doi.org/10.1016/j.ijhydene.2018.04.209>
29. S. S. Sabari, S. Malarvizhi, V. Balasubramanian, G.M. Reddy, Experimental and numerical investigation on under-water friction stir welding of armour grade AA2519-T87 aluminium alloy, *Def. Technol.* 12 (2016) 324–333. <https://doi.org/10.1016/j.dt.2016.02.003>
30. M.A. Wahid, Z.A. Khan, A.N. Siddiquee, Review on underwater friction stir welding: A variant of friction stir welding with great potential of improving joint properties, *Trans. Nonferrous Met. Soc. China* 28 (2018) 193-219. [https://doi.org/10.1016/S1003-6326\(18\)64653-9](https://doi.org/10.1016/S1003-6326(18)64653-9)

31. H.A. Derazkola, F. Khodabakhshi, Underwater submerged dissimilar friction-stir welding of AA5083 aluminum alloy and A441 AISI steel, *Int. J. Adv. Manuf. Technol.* 102 (2019) 4383–4395. <https://doi.org/10.1007/s00170-019-03544-1>
32. T. Miyamori, Y. Sato, H. Kokawa, Influence of underwater operation on friction stir welding of medium carbon steel, In: Y. Hovanski, R. Mishra, Y. Sato, P. Upadhyay, D. Yan (eds.) *Friction Stir Welding and Processing IX* (2017). The Minerals, Metals & Materials Series. Springer, Cham. https://doi.org/10.1007/978-3-319-52383-5_3
33. M.A. Wahid, A.N. Siddiquee, Z.A. Khan, Aluminum alloys in marine construction: characteristics, application, and problems from a fabrication viewpoint, *Mar. Syst. Ocean Technol.* 15 (2020) 70–80. <https://doi.org/10.1007/s40868-019-00069-w>
34. R.A. Sielski, Research needs in aluminum structure, *Ships Offshore Struct.* 3 (2008) 57–65. <https://doi.org/10.1080/17445300701797111>
35. M. Gelfgat, A. Alkhimenko, S. Kolesov, Corrosion and the role of structural aluminum alloys in the construction of oil and gas wells, *E3S Web Conf.* 121 (2019) 04003. <https://doi.org/10.1051/e3sconf/201912104003>
36. M.Y. Gelfgat, V.S. Basovich, A.J. Adelman, Aluminium alloy tubulars for oil and gas industry, paper presented at the SPE Annual Technical Conference and Exhibition, Society of Petroleum Engineers: Dallas, SPE-97035-MS (2005) 1– 11. <https://doi.org/10.2118/97035-MS>
37. J.C.R. Plácido, P.E.V. Miranda, T.A. Netto, I.P. Pasqualino, G.F. Miscow, B.C. Pinheiro, Fatigue Analysis of Aluminum Drill Pipes, *Materials Research* 8 (2005) 409-415. <https://doi.org/10.1590/S1516-14392005000400009>
38. T. Datta, A.D. Pathak, S. Basak, S. Gollapudi, K.K. Sahu, Fractal behavior of surface oxide crack patterns on AISI 4140 high-strength low-alloy steel exposed to the simulated offshore environment, *Appl. Surf. Sci. Adv.* 5 (2021) 100110. <https://doi.org/10.1016/j.apsadv.2021.100110>
39. H. Jia, K. Wu, Y. Sun, F. Hu, G. Chen, Evaluation of axial force, tool torque and weld quality of friction stir welded dissimilar 6061/5083 aluminum alloys, *CIRP J Manuf. Sci. Technol.* 37 (2022) 267-277. <https://doi.org/10.1016/j.cirpj.2022.02.003>
40. H.I. Khalaf, R. Al-Sabur, M.E. Abdullah, A. Kubit, Effects of Underwater Friction Stir Welding Heat Generation on Residual Stress of AA6068-T6 Aluminum Alloy, *Materials* 15 (2022) 2223. <https://doi.org/10.3390/ma15062223>

41. A.K. Shukla, R. Dmitry, O. Volkova, P.R. Scheller, B. Deo, Cold Model Investigations of Melting of Ice in a Gas-Stirred Vessel, *Metall. Mater. Trans. B* 42 (2011) 224-235. <https://doi.org/10.1007/s11663-010-9442-9>
42. Y. Zhen, J. Shen, S. Hu, C. Yin, F. Yin, X. Bu, Effect of rotation rate on microstructure and mechanical properties of CMT cladding layer of AZ91 magnesium alloy fabricated by friction stir processing, *J. Manuf. Process.* 79 (2022) 553-561. <https://doi.org/10.1016/j.jmapro.2022.05.017>
43. Y.J. Li, W.Z. Zhang, K. Marthinsen, Precipitation crystallography of plate-shaped Al₆(Mn, Fe) dispersoids in AA5182 alloy, *Acta Mater.* 60 (2012) 5963-5974. <https://doi.org/10.1016/j.actamat.2012.06.022>
44. G. Yi, B. Sun, J.D. Poplawsky, Y. Zhu, M.L. Free, Investigation of pre-existing particles in Al 5083 alloys, *J. Alloys Compd.* 740 (2018) 461-469. <https://doi.org/10.1016/j.jallcom.2017.12.329>
45. O. Engler, S.M. Jupp, Control of second-phase particles in the Al-Mg-Mn alloy AA 5083, *J. Alloys Compd.* 689 (2016) 998-1010. <https://doi.org/10.1016/j.jallcom.2016.08.070>
46. F. Heirani, A. Abbasi, M. Ardestani, Effects of processing parameters on microstructure and mechanical behaviors of underwater friction stir welding of Al5083 alloy, *J. Manuf. Process.* 25 (2017) 77-84. <https://doi.org/10.1016/j.jmapro.2016.11.002>
47. Z. Zeng, M. Zhou, M. Esmaily, Y. Zhu, S. Choudhary, J.C. Griffith, J. Ma, Y. Hora, Y. Chen, A. Gullino, Q. Shi, H. Fujii, N. Birbilis, Corrosion resistant and high-strength dual-phase Mg-Li-Al-Zn alloy by friction stir processing, *Commun. Mater.* 3 (2022) 1-10. <https://doi.org/10.1038/s43246-022-00245-3>
48. J.G. Kaufman, Chapter 2: Aluminum Alloy and Temper Designation Systems of the Aluminum Association, in *Introduction to Aluminum Alloys and Tempers*, ASM International (2000) 9-22. <https://10.1361/iaat2000p009>
49. K. Gao, S. Basak, M. Mondal, S. Zhang, S.T. Hong, S.Y. Boakye, H.H. Cho, Friction stir welding of AA3003-clad AA6013 thin sheets: Microstructural changes related to tensile properties and fatigue failure mechanism, *J. Mater. Res. Technol.* 17 (2022) 3221-3233. <https://doi.org/10.1016/j.jmrt.2022.02.073>
50. R.S. Mishra, Z.Y. Ma, Friction stir welding and processing, *Mater. Sci. Eng. R Rep.* 50 (2005) 1-78. <https://doi.org/10.1016/j.mser.2005.07.001>
51. S. Basak, M. Mondal, K. Gao, S.T. Hong, S.Y. Anaman, H.H. Cho, Friction stir butt-welding of roll clad aluminum thin sheets: effect of microstructural and texture changes on mechanical properties, *Mater. Sci. Eng. A* 832 (2022) 142490.

<https://doi.org/10.1016/j.msea.2021.142490>

52. M. Mondal, S. Basak, H. Das, S.T. Hong, H. Choi, J.W. Park, H.N. Han, Manufacturing of magnesium/aluminum bimetallic ring components by friction stir assisted simultaneous forging and solid-state joining, *Int. J. of Precis. Eng. and Manuf.-Green Tech.* 8 (2021) 1429-1438. <https://doi.org/10.1007/s40684-020-00244-0>
53. F. Khodabakhshi, A.P. Gerlich, On the correlation between indentation hardness and tensile strength in friction stir processed materials, *Mater. Sci. Eng. A* 789 (2020) 139682. <https://doi.org/10.1016/j.msea.2020.139682>
54. M. Imam, Y. Sun, H. Fuji, N. Ma, S. Tsutsumi, H. Murakawa, Microstructural characteristics and mechanical properties of friction stir welded thick 5083 aluminum alloy, *Metall. Mater. Trans. A* 48 (2017) 208-229. <https://doi.org/10.1007/s11661-016-3819-6>
55. T.A.N. Nguyen, S. Basak, S. Zhang, T.T. Do, M. Mondal, S.T. Hong, M.J. Kim, H.N. Han, Electrically assisted pressure joining of thin bi-layer aluminum-clad aluminum sheets, *Int. J. Adv. Manuf. Technol.* (2022). <https://doi.org/10.1007/s00170-022-09687-y>
56. X. Tao, Y. Chang, Y. Guo, W. Li, M. Li, Microstructure and mechanical properties of friction stir welded oxide dispersion strengthened AA6063 aluminum matrix composites enhanced by post-weld heat treatment, *Mater. Sci. Eng. A* 725 (2018) 19-27. <https://doi.org/10.1016/j.msea.2018.03.094>
57. G. Yi, B. Sun, J.D. Poplawsky, Y. Zhu, M.L. Free, Investigation of pre-existing particles in Al 5083 Alloys, *J. Alloys Compd.* 740 (2018) 461-469. <https://doi.org/10.1016/j.jallcom.2017.12.329>
58. J. Jang, Y. Choi, Y.H. Lee, D. Kwon, Instrumented microindentation studies on long-term aged materials: work-hardening exponent and yield ratio as new degradation indicators, *Mater. Sci. Eng. A* 395 (2005) 295-300. <https://doi.org/10.1016/j.msea.2004.12.033>
59. S.Y. Anaman, H.H. Cho, H. Das, J.S. Lee, S.T. Hong, Microstructure and mechanical/electrochemical properties of friction stir butt welded joint of dissimilar aluminum and steel alloys, *Mater. Charact.* 154 (2019) 67-79. <https://doi.org/10.1016/j.matchar.2019.05.041>
60. S. Basak, S.K. Sharma, M. Mondal, K.K. Sahu, S. Gollapudi, J.D. Majumdar, S.T. Hong, Electron beam surface treatment of 316L austenitic stainless steel: improvements in hardness, wear, and corrosion resistance, *Met. Mater. Int.* 27 (2021) 953-961. <https://doi.org/10.1007/s12540-020-00773-y>

61. S. Basak, S.K. Sharma, K.K. Sahu, S. Gollapudi, J.D. Majumdar, Surface modification of structural material for nuclear applications by electron beam melting: enhancement of microstructural and corrosion properties of Inconel 617, *SN Appl. Sci.* 1 (2019) 708. <https://doi.org/10.1007/s42452-019-0744-5>
62. S. Basak, K.K. Sahu, S.K. Sharma, J.D. Majumdar, studies on electron beam surface melting of AISI316 stainless steel and AISI 347 stainless steel, *Procedia Manuf.* 7 (2017) 647-653. <https://doi.org/10.1016/j.promfg.2016.12.096>
63. K.D. Ralston, N. Birbilis, Effect of grain size on corrosion: a review, *corrosion* 66 (2010) 075005-1-075005-13. <https://doi.org/10.5006/1.3462912>
64. F. Long, Q. Liu, G. Chen, M. Zhou, Q. Shi, Improved corrosion resistance achieved in a friction stir processed Mg-5Zn-0.3Ca alloy with fragmented precipitates, *Corros. Sci.* 208 (2022) 110675. <https://doi.org/10.1016/j.corsci.2022.110675>
65. M.K. Chung, Y.S. Choi, J.G. Kim, Y.M. Kim, J.C. Lee, Effect of the number of ECAP pass time on the electrochemical properties of 1050 Al alloys, *Mater. Sci. Eng. A* 366 (2004) 282-291. <https://doi.org/10.1016/j.msea.2003.08.056>

CHAPTER IV
FABRICATION OF ALUMINUM MATRIX COMPOSITE BY FRICTION STIR
PROCESSING

4.1 INTRODUCTION

In recent years, the manufacturing trend of Al matrix composites (AMCs) has increased due to their lightweight, exclusive mechanical/physical performances and widespread applications in the automotive industry [1,2]. Out of many reinforcing elements, graphene oxide (GO) has attracted much attention because of its superior strength and inherent thermal/electrical conductivity. Combining these advanced characteristics of GO with Al potentially enhanced the overall performance of the AMCs, making this composite more advantageous over the other MMCs [1,3]. Consequently, several manufacturing processes, mainly casting, sintering, powder metallurgy, and other melt-based techniques, have produced GO-reinforced AMC [4]. However, poor interfacial bonding, GO agglomeration, and other common melt defects could be common issues with these traditional processing methods [1,3]. Also, the amount of GO needs to be controlled to prevent the development of unwanted brittle metal carbide (mostly Al_2C or Al_4C_3) phases into the matrix during the above-mentioned processes [5-7]. Besides, a significant mismatch of atomic size (radius) between carbon and Al could cause significant mismatch strain in the microstructure and the corresponding poor mechanical performance of the composite [8,9].

Friction stir processing (FSP), a solid-state material processing technology inherited from the mechanism of friction stir welding (FSW), has already proven its worth in the manufacture of AMCs, regardless of the reinforcement materials used [3,10]. In FSP, a continuous rotational tool

helps to stir reinforcing materials inside the matrix while the operating temperature lies below the melting temperature of the substrate materials. This further helps to eliminate melting defects and minimize the possibility of getting brittle intermetallics in the metal matrix of the composites [3].

Almost all cases of making AMCs using FSP involved the fabrication of grooves on the substrate material surface or considering multiple passes to get proper reinforcement distributions within the matrix [1-4]. For example, Dixit et al. [3] fabricated Al/multi-layer graphene using seven-pass FSP with a groove to lay the reinforcements in the pure Al. Sharma et al. [11] presented the single/multiple micro channel technique to fabricate AA6061/CNT composites using FSP. They found an improvement in strength for both single and multiple micro-channels reinforcement conditions, but both cases revealed a loss in ductility compared to the base material (BM). Khodabakhshi et al. [1] produced Al-Mg/graphene nano-composites using a graphene-filled groove and five cumulative passes in FSP. They also reported higher strength of AMC with loss of ductility than BM. However, these approaches require additional steps that can be time-consuming and increase the overall cost of manufacturing AMCs. In their review article, Zhang et al. [4] clarified several aspects of the efficient fabrication of metal matrix composites (MMCs) using FSP. Among them, the optimization of FSP parameters and reinforcing methods stand out.

Therefore, the present study experimentally investigates GO-reinforced AMC manufactured by single-pass FSP, in which the reinforcement particles are adhesively attached to the surface of pure Al. The novelty of this research is related to the reinforcement strategy that demonstrates the presence of GO in the Al matrix and its interaction in the context of the microstructural changes to develop the mechanical properties of AMC.

4.2 MATERIALS AND EXPERIMENTAL PROCEDURES

4.2.1 Materials

This study used rectangular plates with $200 \times 75 \times 3$ (all dimensions are in mm.) made of commercially pure Al (AA1050-H14) as the BM substrate. The chemical compositions of the BM are presented in Table 4.1. The chemically synthesized powder GO-V50 (C: 40 - 50 wt.%, O: 40 - 50 wt.%, H, S: ≤ 3 wt.%, N: ≤ 1 wt.%, Standard Graphene, Republic of Korea) with an average particle size of $\sim 65 \mu\text{m}$ was used as reinforcing material.

Table 4.1 Chemical compositions of AA1050-H14 (wt.%)

Materials	Si	Fe	Cu	Mn	Ni	Ti	Al
AA1050 H14	0.25	0.30	0.004	0.01	0.02	0.02	Bal.

4.2.2 Experimental procedures

Before FSP, all the rectangular plates were cleaned with ethanol to remove dirt and other undesirable objects from the surface. Then, the GO particles were adhesively attached to a 180 mm long, 8 mm width marked rectangular area in the center of the rectangular plate. After the powder dried with adhesive, FSP was performed by positioning the tool in the center of the 8 mm GO-filled area. The weight of the Al plate was measured with graphene (121.86 ± 0.04 gm) and without graphene (121.36 ± 0.02 gm) to determine the maximum possible amount (~ 0.5 wt.%) of GO present in the manufactured AMCs. The custom-built FSW machine (RM-1, Bond Technologies, Elkhart, IN, USA) was used to manufacture GO-reinforced AMCs, and the process was named FSP with GO. Similarly, another processing was carried out on the surface of Al

without GO particles called FSP-only. The manufacturing steps of these processes are schematically represented in Fig. 4.1(a). The process parameters for FSP-only and FSP with GO were similar and mentioned in Table 4.2. During processing, an embedded data acquisition system was used to record process responses, including axial force and torque concerning the tool travel inside the material. In addition, temperature profiles were measured using a type K thermocouple fixed near the stir zone (SZ) of the retreating side (RS) of the specimen. The measurement point was positioned at 1 mm from the RS and 6 mm from the center to avoid thermocouple shearing during tool movements inside the materials. Please note that the FSP-only processing was performed first before the tool pin contacts the GO particles in FSP with GO processing condition. A commercially available H-13 steel-made tool with a concave shoulder (10 mm dia.) attached with a cylindrical threaded pin (3 mm dia.) was used throughout the experiments.

Table 4.2 FSP parameters

Conditions	Rotational speed (rpm)	Travel speed (mm/min)	Tool tilt angle (°)	No. of pass
FSP-only	400	50	1.80	1
FSP with GO				

After processing, the cross-sections of both FSP-only and FSP with GO specimens were machined perpendicular to the tool travel direction, followed by grinding, polishing to 1 μm diamond paste suspension, and etching with Keller's reagent for optical microscopy (OM, GX41, Olympus Corp., Tokyo, Japan). For characterizing the presence of GO inside the Al, the Raman spectroscopy analysis was carried out on the advancing side (AS) and retreating side (RS) of the

SZ using a confocal micro-Raman apparatus (alpha 300R, WITec, Germany). The scanning range was set from 1100 to 2100 cm^{-1} with an incident laser light at a wavelength of 532 nm. For a detailed understanding of the depth profile of GO (C) particles in the Al matrix, a secondary ion mass spectrometry (SIMS, CAMECA, IMS 7F, France) was performed on the polished (up to 1 μm diamond paste suspension) top surface of the produced AMC at 10 kV Cs^+ analysis beams. A scanning electron microscope (FE-SEM, SU5000, Hitachi High-Technologies Corp., Tokyo, Japan) was then used to confirm where GO particles could exist, followed by EDS live chemical imaging (X-Max, Oxford Instruments America Inc., Concord MA, USA). Transmission electron microscope (TEM) TEM sampling was attempted primarily using dual steps focused ion beam milling SEM (FIB-SEM, Nova NanoLab 200, FEI, Netherlands). The platinum (Pt) was deposited over the GO during this FIB milling in SEM. Later the milled specimen underwent a subsequent thinning process by another FIB operation (FIB-SEM, Helios NanoLab 600, FEI, Netherlands), and the desired specimen for transmission electron microscopy (TEM) analysis was prepared. During the final stage of TEM sampling, the Pt was successively redeposited on the existing Pt layer. Considering the complex geometry of the specimen and the chances of damage on the GO flake, tungsten (W) was purposely deposited on the Pt layers before the sample thinning operation was started. A TEM (Talos F200X G2, USA) was used to characterize GO and its interface with Al, followed by EDS elemental scanning. Electron backscatter diffraction (EBSD) analysis was performed on the cross-sections of the FSP-only and FSP with GO specimens to understand the effects of GO enhancement on the microstructural changes of the fabricated AMC. The cross-sections were further polished up to 0.25 μm diamond paste suspension, followed by 0.04 μm colloidal silica polishing to obtain the final surface for EBSD analysis. An FE-SEM equipped with EBSD (TSL Hikari Super, TSL, USA) was used to explain statistical microstructural changes of

FSP with GO compared to FSP-only and BM. The EBSD analysis includes inverse pole figure (IPF), grain boundary character distribution (GBCD), kernel average misorientation (KAM), grain orientation spread (GOS) maps, and microtexture (pole figures) analysis from the various sites of the SZs and BM. The step size of the EBSD scan was set at 0.80 μm for BM and 0.20 μm for the significant locations in SZs. Microtexture analysis by PFs was performed based on the standard texture fiber orientations in the $\{111\}$ crystallographic plane for FCC materials [12,13].

The mechanical performance of the manufactured AMCs was evaluated by surface microhardness mapping and uniaxial tensile testing. Vickers microhardness tester (HM-200, Mitutoyo Corp., Kanagawa, Japan) was used to perform 2D microhardness mapping on the cross-sections of the processed FSP-only and FSP with GO specimens. A total of 170 indents were measured with a load of 0.50 N at a dwell time of 15 secs. The indentation location started from the BM, traversed the SZ, and reached the BM opposite the starting position. The sub-size tensile specimen [14] was made from the SZ of both FSP-only and FSP with GO specimen along PD (Fig. 4.1(b)) for uniaxial tensile tests, using a universal testing machine (DTU900-MH, Daekyung Co., Ltd., Busan, South Korea). The BM tensile specimen was prepared along the RD of the Al plates. The design of the tensile specimen is also given in Fig. 4.1(b). A constant strain rate of 10^{-3} s^{-1} was maintained throughout the tensile tests until fracture. Four specimens of both FSP-only and FSP with GO were tested for the repeatability of the tensile results. Finally, fractography analyses on the fracture surfaces of the broken tensile specimens for BM, FSP-only, and FSP with GO were performed using SEM.

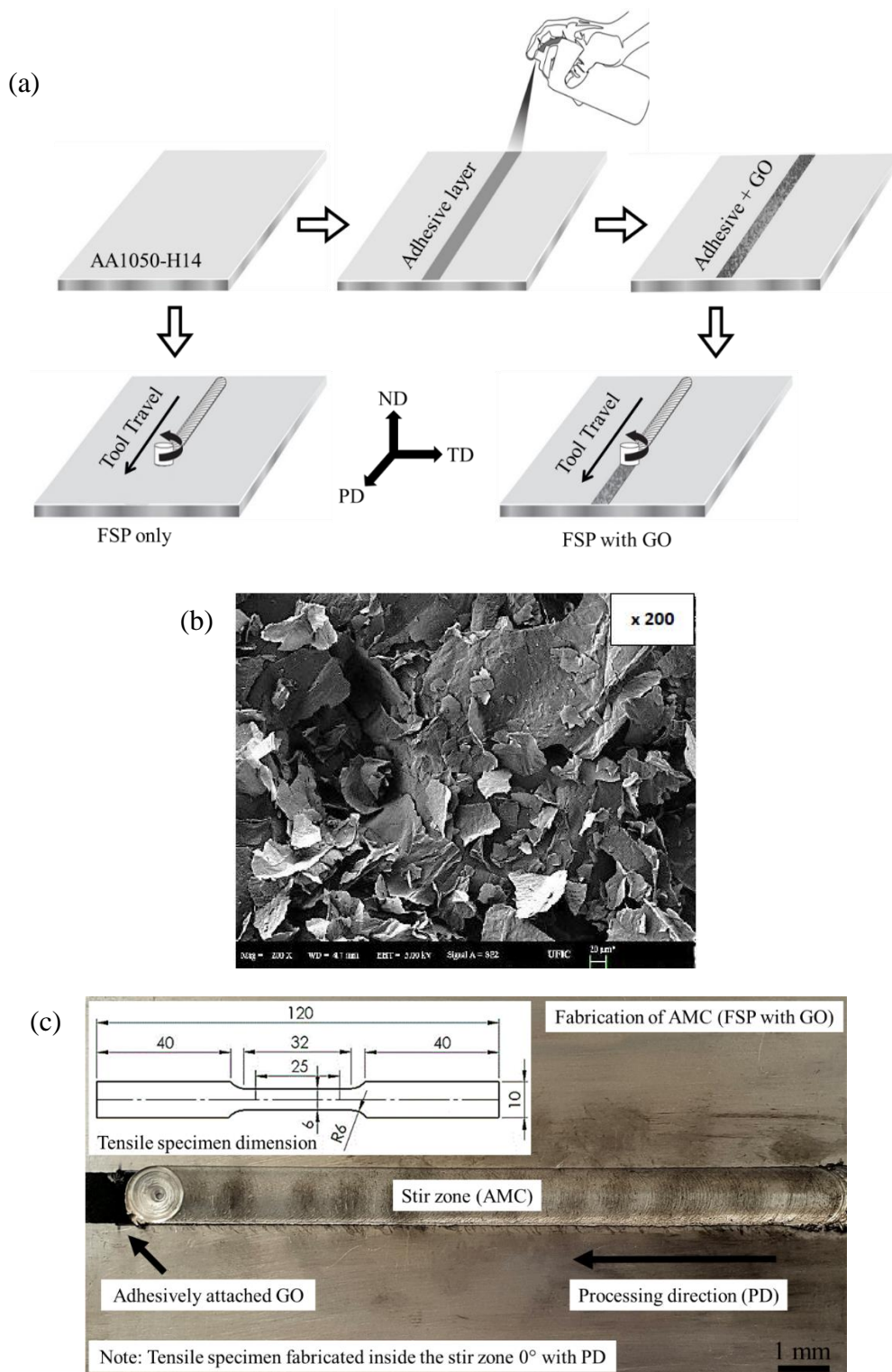


Figure 4.1 (a) Schematic of AMC fabrication using FSP, (b) SEM image of GO particles, (c) a detailed picture of the fabricated AMC.

4.3 RESULTS AND DISCUSSION

4.3.1 Process response and optical microscopy

The force and temperature profiles of FSP-only and FSP with GO are shown in Fig. 4.2. The forces appeared to be very high (Fig. 2(a)) in the initial stages of the tool plunging due to higher order of friction between the tool-workpiece interface. However, the force values dropped and became stable with minimal fluctuations as the tool pin reached the desired penetration depth and began to move along its defined path for both processing conditions. Also, at the transition phase between tool plunging and linear traversing, the force values for FSP with GO compared to FSP-only increased sharply (magnified inset in Fig. 4.2(a)) due to the presence of the GO layer between the tool and the substrate material. The peak temperature of FSP-only (280°C) was higher than the FSP with GO (193°C), as shown in Fig. 4.2(b). The GO having higher thermal conductivity can act as a nano-coolant at the tool-workpiece interface, lowering the peak temperature during processing [15,16]. Optical macrographs on the cross-section of the FSP-only and FSP with GO specimens are presented in Fig 4.3(a, b). In both cases, no such macroscopic defects are observed in the SZ. The yellow rectangles marked S₁ and S₂ represent sites of interest for a detailed microstructural analysis of the AS and RS of both SZs.

4.3.2 Raman spectroscopy analysis

The Raman spectra of the GO reinforcing particles (Fig. 4.4(a)) shows the presence of typical D and G band peaks at a Raman shift of ~1335 cm⁻¹ and ~1587 cm⁻¹ with an intensity ratio (I_D/I_G) of 0.53. The presence of the low-intensity D band refers to the lower defect density in the used GO powder [17,18]. Raman spectra of AS (blue), RS (red) in SZ of FSP with GO, and AS (black) in SZ of FSP-only are presented in Fig. 4.4(b, c). In the case of the FSP with GO, Raman spectra on the AS side reveal the presence of GO with particular vibrational modes of D and G

bands at the Raman shift of $\sim 1260\text{ cm}^{-1}$ and $\sim 1567\text{ cm}^{-1}$. In contrast, the RS side reveals a smooth D band at $\sim 1272\text{ cm}^{-1}$ with a hump in the G band at $\sim 1562\text{ cm}^{-1}$ Raman shift position.

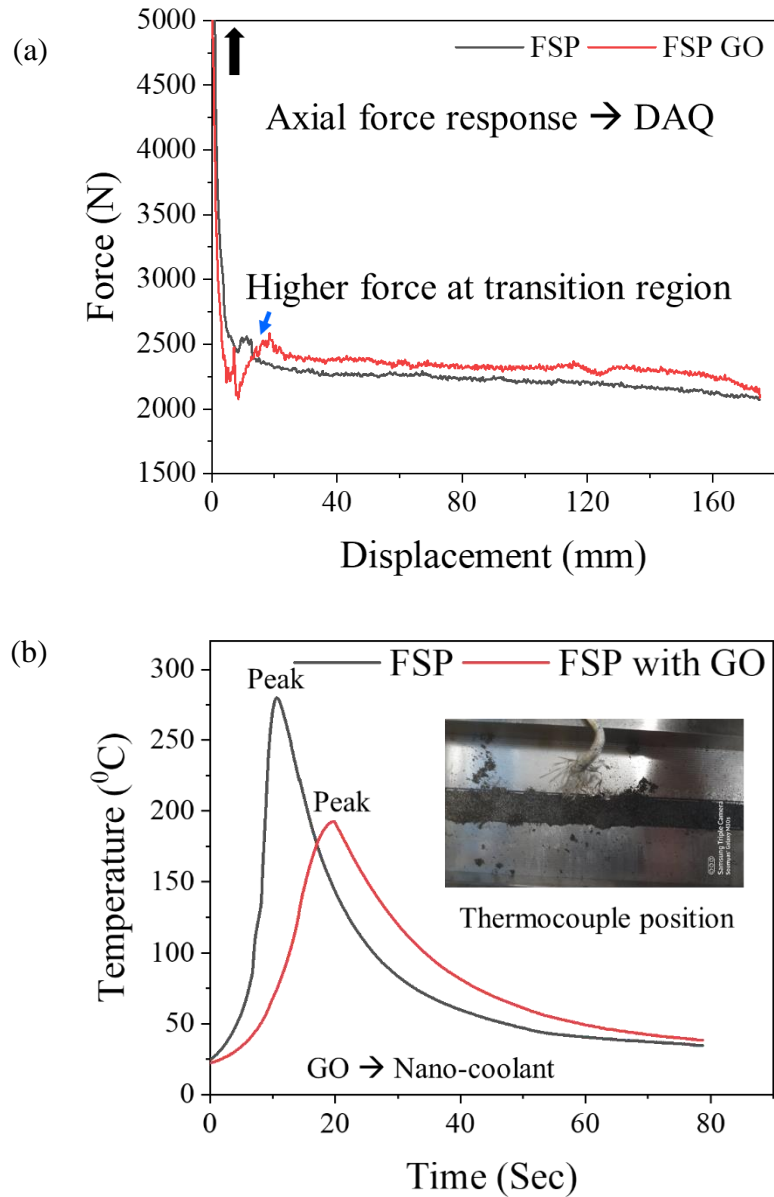


Figure 4.2 (a) Axial force distribution, (b) temperature curves obtained during FSP-only and FSP with GO conditions.

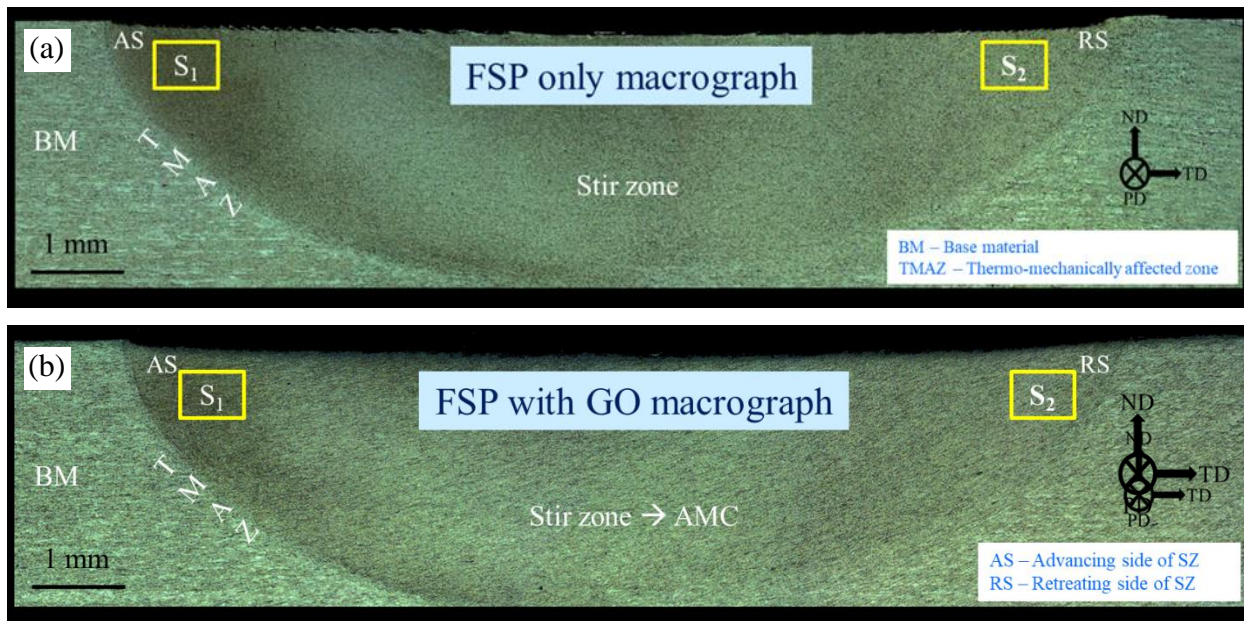


Figure 4.3 OM macrographs of the cross-sections of (a) FSP-only and (b) FSP with GO conditions.

The intensity ratio (I_D/I_G) was measured to be 1.13 for AS and 1.05 for RS of the fabricated AMC, notably higher than the as-received GO particles (0.53). The decrease in intensity of G bands for both sites (FSP with GO) further confirms the edge distortion of the GO particles, which were probably sheared by the continuous rotation of the tool pin during FSP [18]. For AS of the FSP-only SZ, the Al peak appeared at a Raman shift position of $\sim 1263 \text{ cm}^{-1}$, which was shifted by $\sim 60 \text{ cm}^{-1}$ compared to the ideal peak position of Al under Raman spectroscopy [19]. A similar observation also fits FSP with GO, where the Raman shift positions for the D and G bands of GO are shifted $\sim 75 \text{ cm}^{-1}$ and $\sim 20 \text{ cm}^{-1}$ from their actual positions in Fig. 4.4(a). The main reason for this observation is the extent of plastic deformation and mechanical straining caused by the process mechanism of FSP [11,20-21].

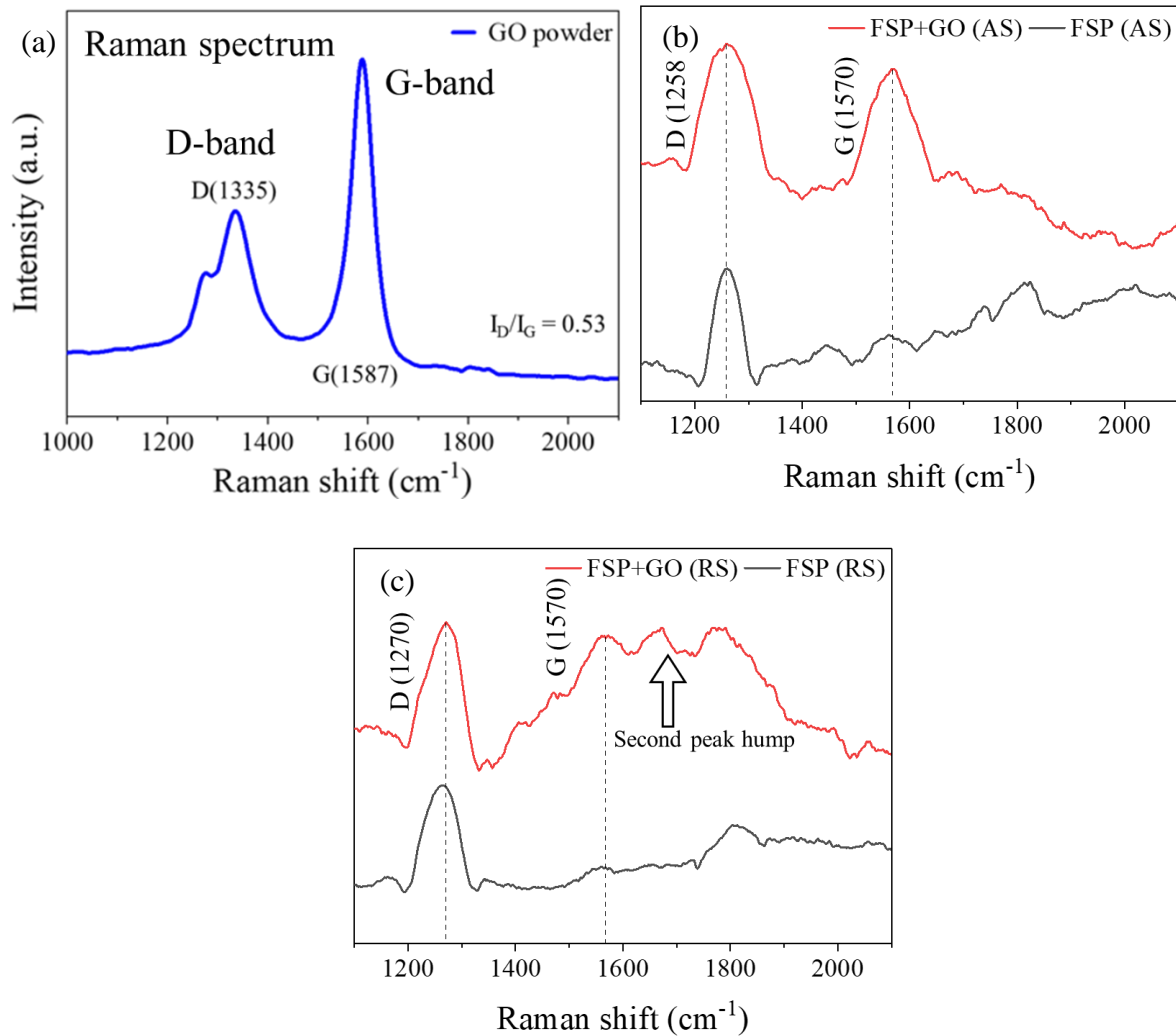


Figure 4.4 Raman spectrums of (a) GO, (b) AS, and (c) RS of FSP with GO and FSP-only SZ.

4.4.3 SIMS analysis on GO survivability in Al matrix

The SIMS analysis was performed to identify the presence of GO in a specific area of the Al matrix, as shown schematically in Fig. 4.5(a). An intense CS⁺ primary ion beam sputtered onto the target surface, removed Al and C (trace element) as secondary ions, and provided the depth profiles of each, as shown in Fig. 4.5(b). The linear profile of Al represents the matrix phase, while the intensity of the C profile shows continuous ups and downs until the scan stops.

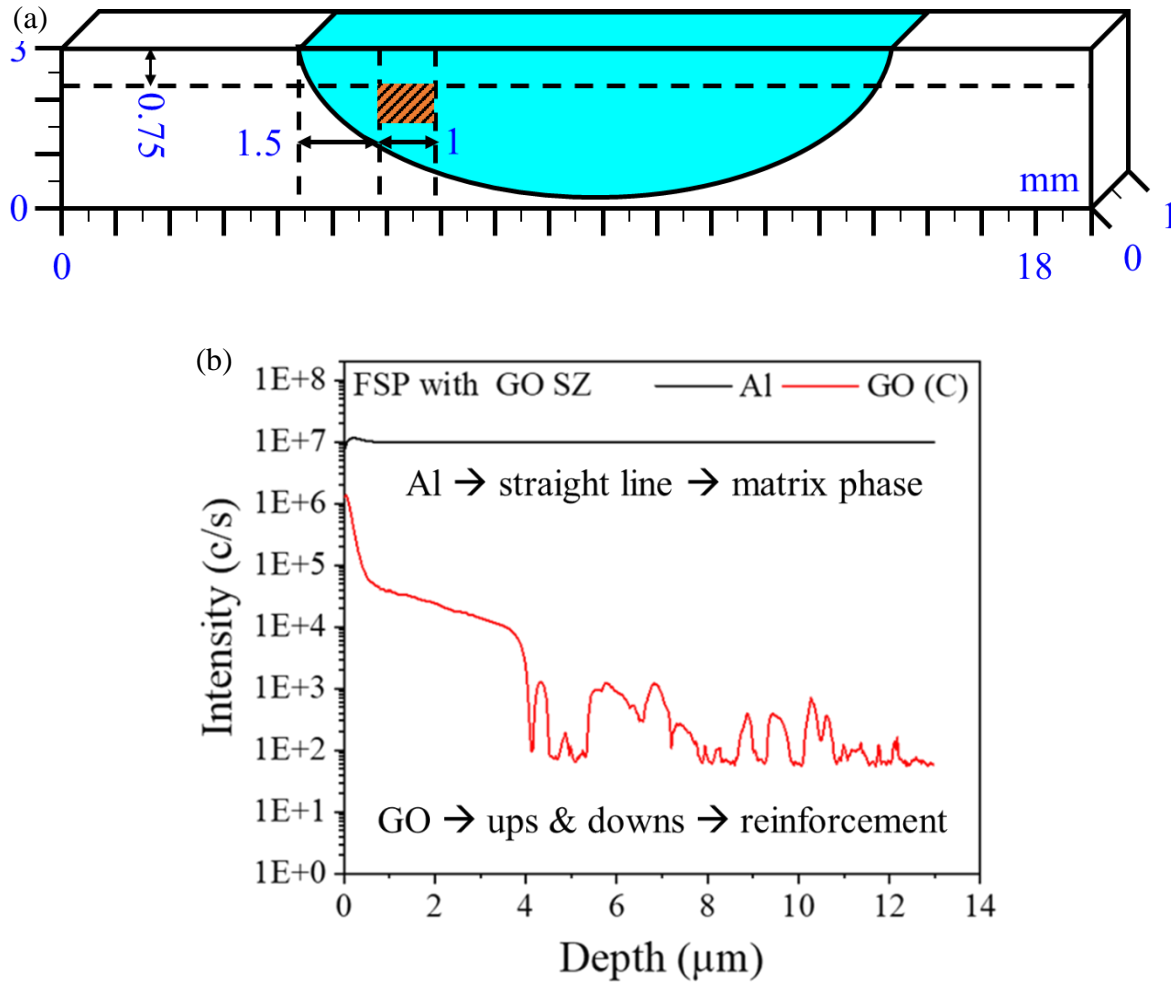


Figure 4.5 (a) Schematic of SIMS location, (b) Al and C depth profiles.

The total ion images of C at the initial and slightly deeper position within the SZ were acquired for both FSP-only and FSP with GO conditions, as shown in Fig. 4.6(a-d). The ion images taken from the slightly deeper position in the SZ of FSP with GO (Fig. 4.6(d)) expose the presence of GO particle, marked with a white dotted circle in Fig. 4.6(d). In comparison, no such presence of C within the SZ of the FSP-only condition is shown in Fig. 4.6(b). The SEM image on the SIMS analysis zone shows an ion-implanted surface separated from the other unprocessed region in Fig. 4.6(e). The presence of GO particle as an irregular shape (marked with a black dashed line) within

the Al matrix is observed in the magnified SEM image (Fig. 4.6(f)). EDS live chemical imaging in Fig. 4.6(g) further confirms its composition. The irregular shape of the GO particle is mainly caused by the shearing action of the FSP tool during the fabrication of the AMC [1,4].

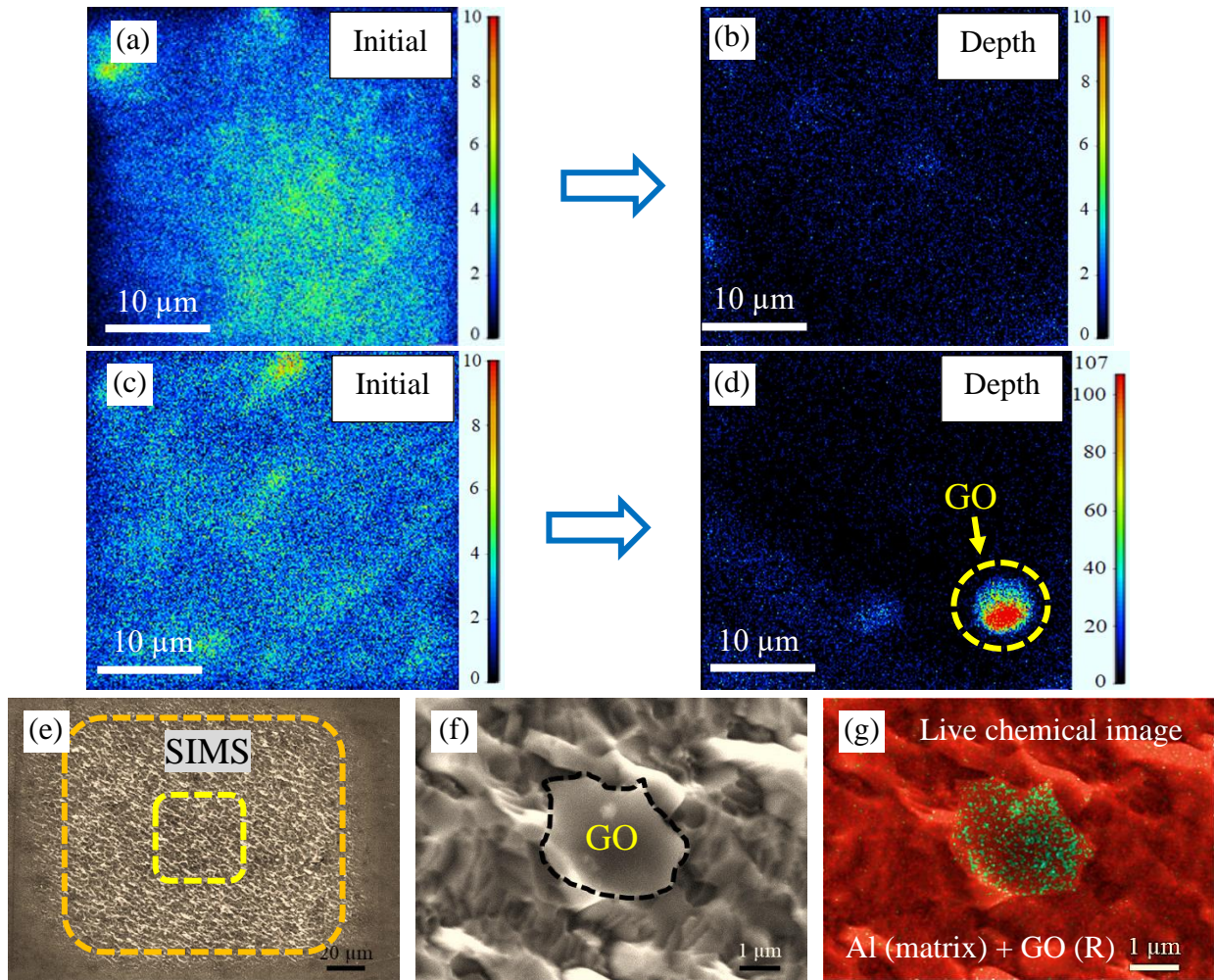


Figure 4.6 Microprobe Cs⁺ scanning beam induced total ion imaging of C in (a, b) FSP-only and (c, d) FSP with GO SZ. (e) SEM image on the SIMS site, (f) magnified SEM images from the mark locations (yellow), (g) EDS live chemical imaging of Al and C.

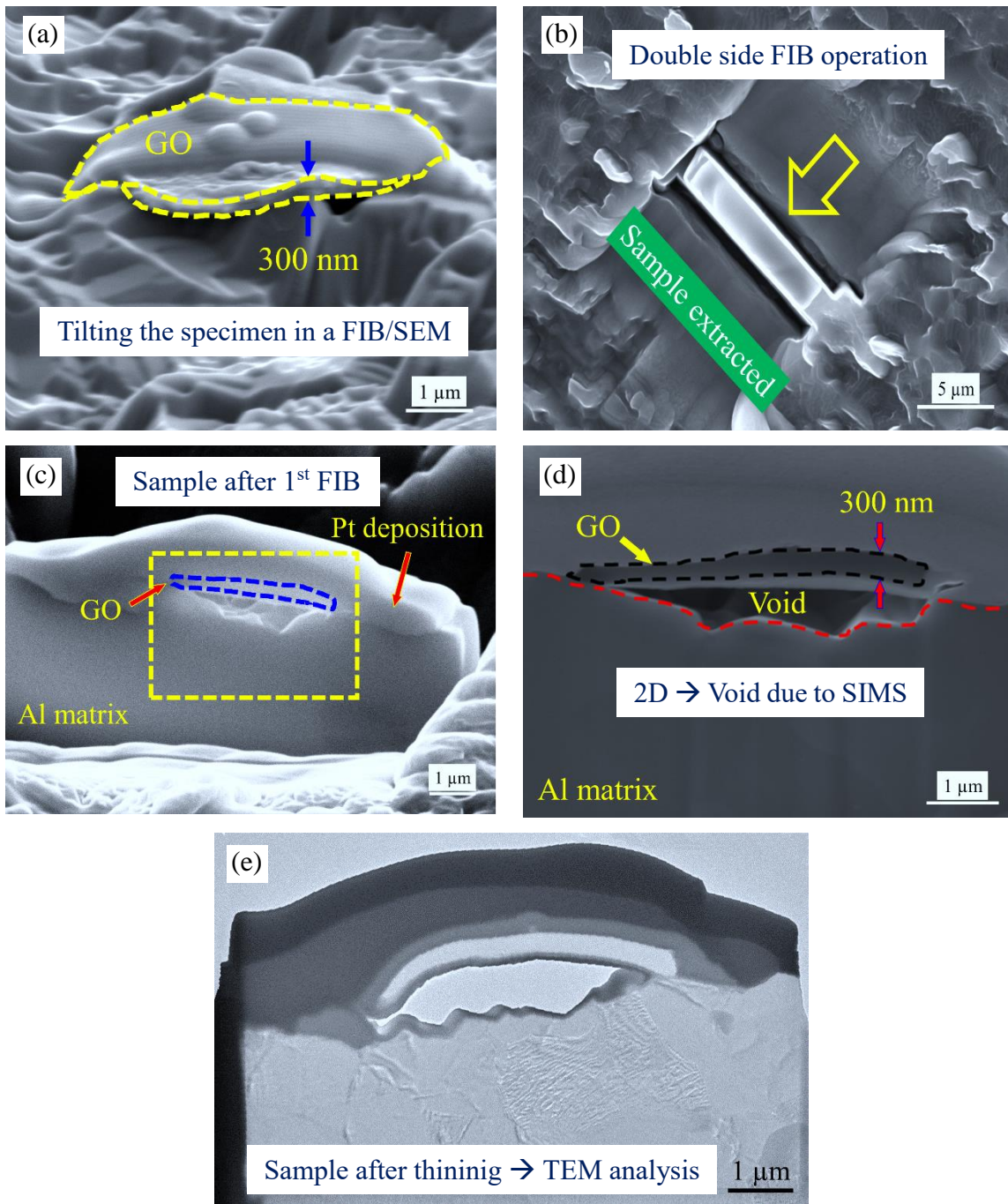


Figure 4.7 (a) Tilted view of GO at SIMS site under FIB-SEM, (b) Sample extraction (black arrow) using both sides of FIB, (c) SEM image of the extracted sample, (d) magnified image of the marked location (blue dotted rectangle) in Fig. (c), (e) sample prepared for TEM analysis.

4.3.4 Morphological characterization of GO using TEM

For a detailed understanding of the morphological presence of GO in the Al, the same location in Fig. 4.6(g) was tilted further using FIB/SEM, as shown in Fig. 4.7(a). The GO particle appeared as a nano-flake reinforcement in the Al matrix with a measured thickness of ~300 nm. Figure 4.7(b) shows the sample extracted using the first step of the FIB from a similar site in Fig. 4.7(a). The specimen extracted after the first FIB step is shown in Fig. 4.7(c). The magnified image of the marked location in Fig. 4.7(c) displayed the presence of GO flake on the Al matrix in Fig. 4.7(d). The GO flake was identified by the difference in its compositional contrast with Pt. The final sample for TEM analysis was prepared after multiple stages of FIB operations, shown in Fig. 4.7(e). The TEM micrograph of the entire specimen is shown in Fig. 4.8(a), where two locations are marked for a detailed analysis (blue and green dashed rectangles) and considered as Zone 1 and 2, respectively. The magnified image of Zone 1 (Fig. 4.8(b)) shows the consecutive elemental deposition of Pt and W over the GO flakes present in the Al matrix. Conversely, an interface boundary (marked with a red dashed line) between the GO and the Al is revealed in Zone 2, as shown in Fig. 4.8(c). Furthermore, the high-resolution TEM images (HR-TEM) of the GO particle (green square), Al matrix (blue square), and their interface (yellow rectangle) in Zone 2 are shown in Fig. 4.8(d-f). The HR-TEM image and the selected area electron diffraction (SAED) pattern (inset) acquired from the GO particle represent the amorphous nature of the GO in Fig. 4.8(d). Naturally, the GO particles represent both amorphous and crystalline carbon by D and G bands appearing in Raman spectra [17]. Multiple irradiations caused by different ion beams during SIMS and FIB methods can influence a possible transformation of GO into a typical amorphous carbon character [22,23]. On the other hand, the TEM image (Fig. 4.8(e)) and the SAED pattern (inset) of the Al matrix represent a single crystal FCC at a zone axis of [011] with a typical appearance of

grain boundaries and dislocations. The HR-TEM image at the interface shows the dislocation accumulation, marked with red arrows in Fig. 4.8(f). The dislocations are mostly clogged near GO particles at the interface, indicating that the reinforcing particles act as a barrier to dislocation movement in the Al matrix [18]. In addition, the EDS elemental area scan on the high-angle annular dark-field (HAADF) STEM image of the entire TEM sample and the corresponding maps of Al, C, N, O, S, Pt, and W are shown in Fig. 4.9.

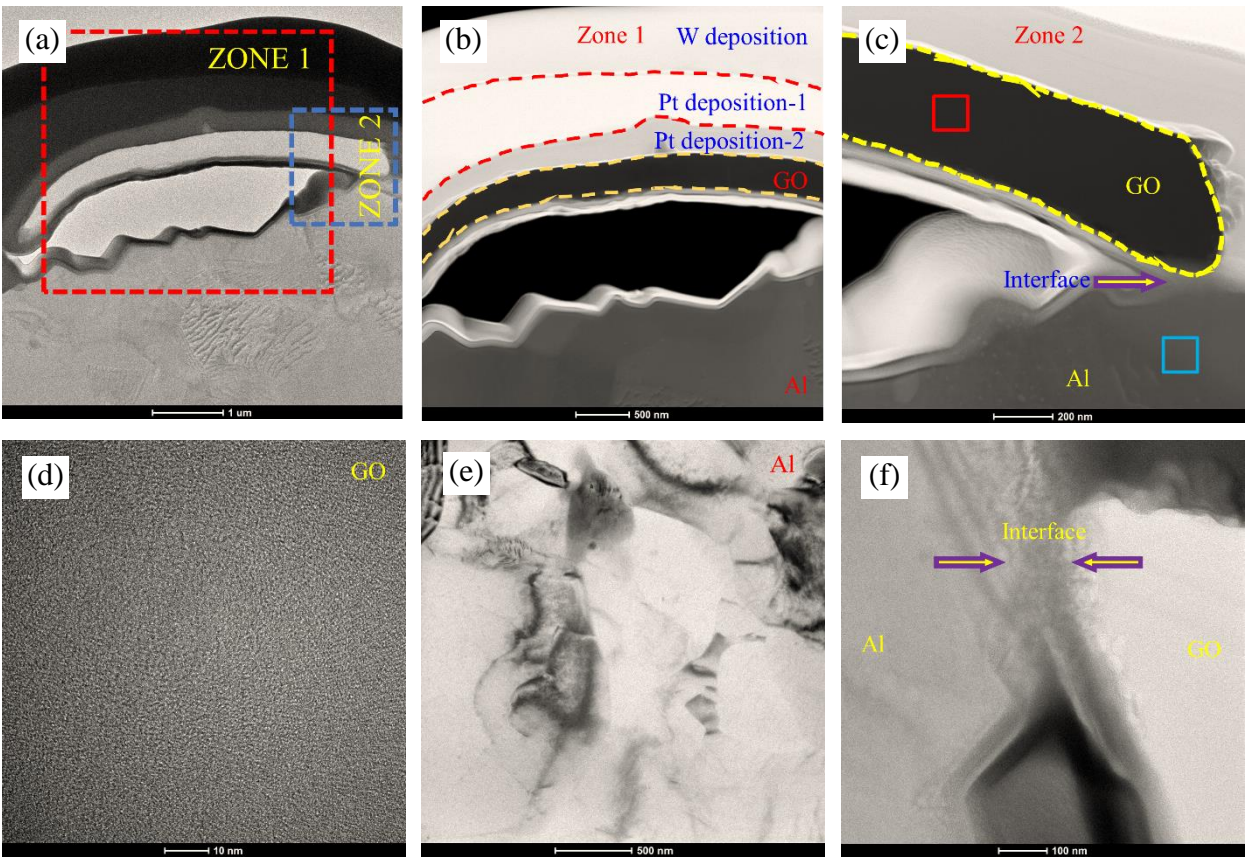


Figure 4.8 (a) TEM micrograph of the entire specimen focused for analysis, (b, c) magnified TEM images of Zone 1 and Zone 2, high-resolution TEM (HR-TEM) images of (d) GO reinforcement, (e) Al matrix, and (f) interface between GO and Al.

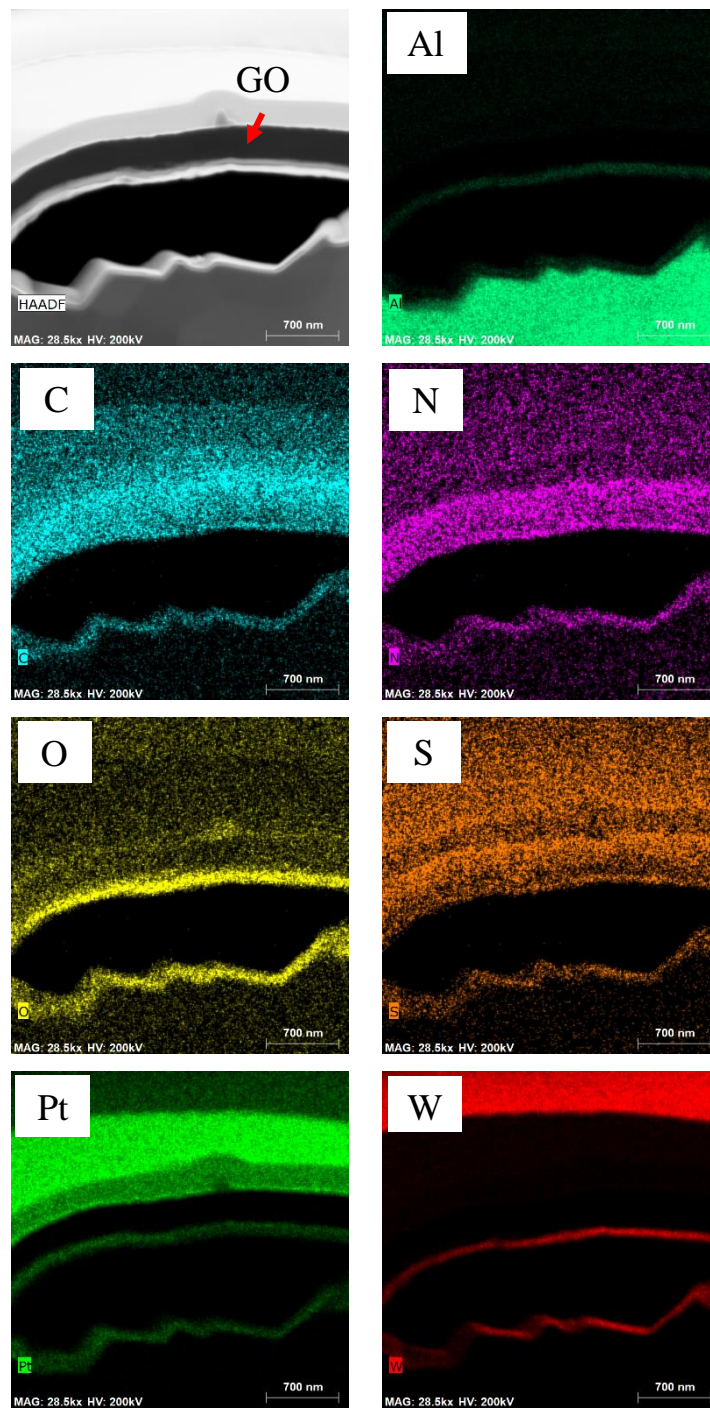


Figure 4.9 HAADF STEM image on the specimen and corresponding EDS elemental area mapping of Al, C, N, O, S, Pt, and W, respectively.

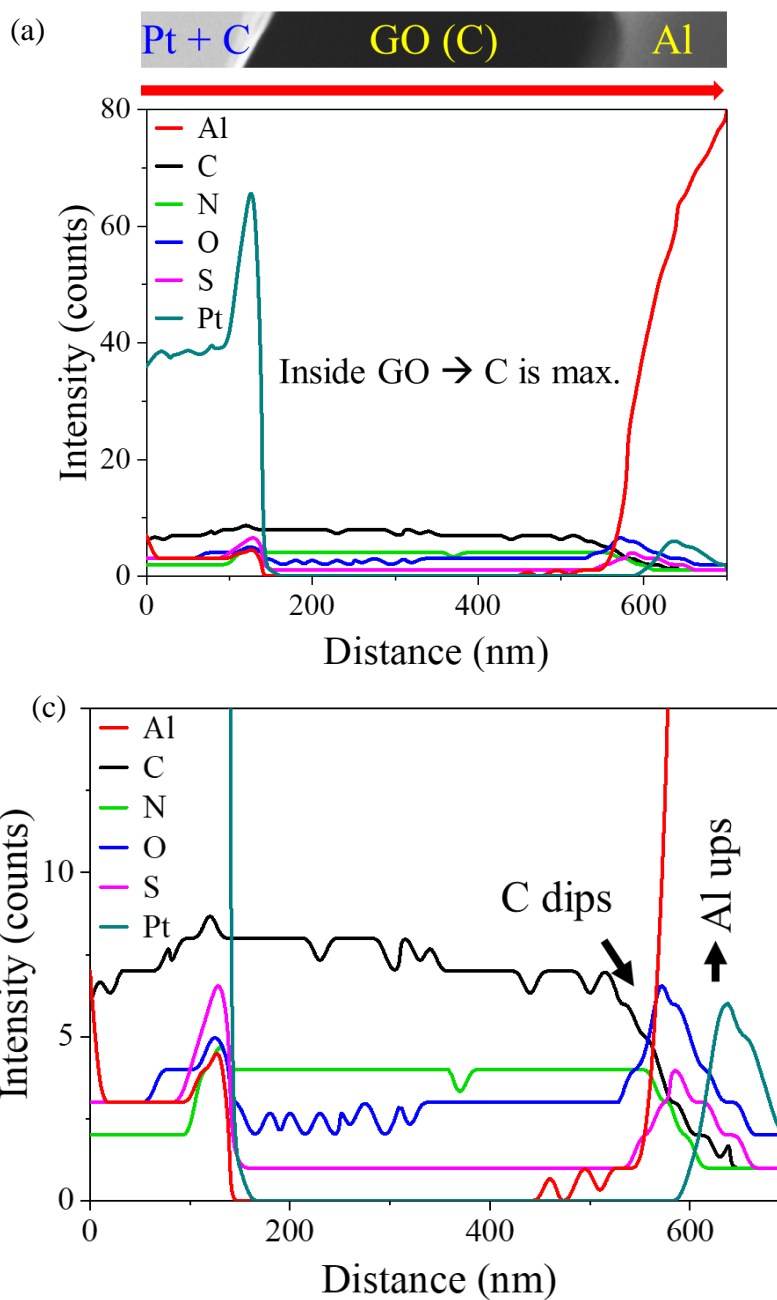


Figure 4.10 (a) line scanning spectra show the elemental profile of the present trace elements with Al and C, (b) Magnified view of the line scanning spectra C has a slightly higher concentration value among other elements present in GO.

The GO can be precisely identified from the appearance of C, S, O, and N element maps compared with its chemical composition. However, O does not appear strongly in GO due to the possible formation of metallic oxides, as Pt and W surrounded the GO flake. It has also been observed that Pt and W deposition layers also contain some amount of C since they cannot be deposited singularly by their deposition methods under FIB/SEM. The EDS line profile analyzed the elemental distribution across the interface (Fig. 4.10(a)) between the GO and Al -matrix at Zone 2, as shown in Fig. 4.10(b). The left side of the elemental distribution reveals a sharp peak (cyan color) of Pt with the highest intensity, which rapidly decays as the scan enters the GO region, followed by the Al matrix. The magnified view of the scan spectra (up to intensity counts 15) shows evident elemental distribution inside the GO in Fig. 4.10(c). Carbon (C) has a slightly higher intensity value than other elements present inside the GO. As the scan travels along the interface to some distance into the Al matrix, no significant elemental diffusion layer was found between the C and Al. The C intensity falls off sharply (Fig. 4.10(c)) after the scan has traveled ~500 nm, and from the same point, the intensity of Al rises steeply as the scan enters the Al region. This further suggests no possible formation of brittle intermetallic phases at the interface between GO and Al. The FSP technique can benefit AMC fabrication over the other technologies as it can limit intricate reaction layers between the reinforcement and matrix phases [1,4].

4.3.5 EBSD analysis of the produced AMC

The IPF map (Fig. 4.11(a)) of BM represents a coarse elongated grain structure with an average grain size of 42.86 μm , with most of the grains being severely strained, with 1.01 KAM_{avg} value, as shown in Fig. 4.11(b). The grain boundary characteristic of BM is dominated by the presence of LAGBs (63.50%), classifying an overall presence of a deformed (97.90%) microstructure as indicated by the GOS map in Fig. 4.11(d). These microstructural phenomena of

BM are primarily attributed to the significant strain hardening from cold rolling in its manufacturing stages. After the FSP, the microstructural appearance changes significantly without GO and with GO conditions, as depicted in Fig. 4.12 and 4.13.

For FSP-only, the AS (S_1) shows a fine equiaxed grain structure with a mean average grain size of $2.05\ \mu\text{m}$, as shown in Fig. 4.12(a). The KAM map (Fig. 4.12(b)) reveals less straining than the BM, with an average KAM value of 0.72. The grain boundary characteristics are mainly dominated by the formation of HAGBs (83.5%) in Fig. 4.12(c), with almost 90% of the total grains appearing as dynamically recrystallized grain structures, as shown in the GOS map in Fig. 4.12(d). In comparison, the AS of the FSP with GO reveals grain size reduction (Fig. 4.12(e)), with an average grain size of $1.83\ \mu\text{m}$. Overall, there is no difference in microstructural characteristics for FSP with GO than in the FSP-only condition. The changes exist only in values where GO reinforcement caused significantly more HAGBs (87.80%) and a higher amount of recrystallized grains (90.30%), as shown in Fig. 4.12(g, h). However, adding GO does not affect the average KAM value at the AS. There are some changes in the re-arrangement of straining during forming new grain boundaries, as observed in Fig. 4.12(f). The EBSD maps on RS (S_2) of FSP-only SZ are shown in Fig. 4.13(a-d), and for FSP with GO in Fig. 4.13(e-h). Similar to AS, the overall microstructural appearances for both regions represent dynamically recrystallized fine-grain structures. The average grain size was measured at $3.05\ \mu\text{m}$ without GO reinforcement, somewhat smaller than that of the FSP with GO ($3.30\ \mu\text{m}$). Adding GO remarkably decreased the average KAM value (0.42) on the RS than the FSP-only (0.71) condition. The number of HAGBs (87.10%) present in FSP with GO is higher than in the FSP-only (77.40%) condition. In addition, a higher proportion of dynamically recrystallized grains (93.60%) is also perceived for FSP with GO than without GO reinforcement (88.20%) condition.

For high stacking fault energy material such as Al, the overall appearance of an equiaxed fine-grained structure after FSP compared to the coarse-grained structure in BM is due to the continuous dynamic recrystallization (CDRX) [24,25]. In the case of FSP with GO, the grain structure on the AS of SZ appeared finer than the without reinforcing condition through the particle-stimulated nucleation (PSN) mechanism [1,26]. In addition, the reinforcement particles activate the pinning effect on the grain boundary in the Al matrix. These broken GO particles further influence the formation of higher numbers HAGBs to the extent of recrystallization, as they hinder grain boundary migration and increase the number of grain boundaries during FSP [26]. The KAM maps on the AS of FSP-only and FSP with GO conditions reveal significant changes in strain distributions through the grain average misorientation than the BM. The strains are well distributed through the grain boundaries in the case of FSP with GO, whereas there are still a few strained grains exhibited for FSP-only. This is due to the FSP-induced recrystallization in combination with the effect of fragmented GOs acting as a barrier in moving the strained energy in the Al matrix [26,27]. Comparing AS and RS of the SZ, the average grain size in RS is slightly larger than in AS for both FSP-only and FSP with GO conditions. Based on the FSP mechanism, the AS of the SZ always experiences a higher-order plastic deformation, and the high-speed material flow begins here [12]. Therefore, the GO particles in FSP with GO condition flow with the high-speed material and have higher possibilities of matrix-particle interactions at the AS of SZ. In contrast, the material flow ends at the RS, where comparatively less deformation and subsequent annealing show marginal grain coarsening with higher dynamic recrystallization than the AS of SZ [28]. In addition, GO particles increase the dynamic recovery rate, resulting in significant strain absorption across grain boundaries and the lowest average KAM value for RS of FSP with GO [26,27]. Microtexture analysis of the BM reveals a C-fiber dominant ideal rolling

texture with the formation of $A_1^*/A_2^* \{111\} \langle 112 \rangle$ texture components at 5.64 maximum intensity in Fig. 4.14(a). After FSP, the microtexture of the BM further transforms into a shear texture with the sheared components marked in black triangles. The A_1^*/A_2^* shear texture components with maximum intensities of 5.24 and 3.39 are observed for AS and RS of the processed FSP-only specimen, as shown in Fig. 4.14(b, d). For FSP with GO specimen, the shear texture components changed from A_1^*/A_2^* to $A_1^* (11\bar{1}) [2\bar{1}1]$ and $C \{001\} \langle 110 \rangle$ with maximum intensities of 4.29 and 3.04 for AS and RS of SZ in Fig. 4.14(c, e). The addition of GO significantly reduces the intensity of preferential orientation through a greater degree of recrystallization [29].

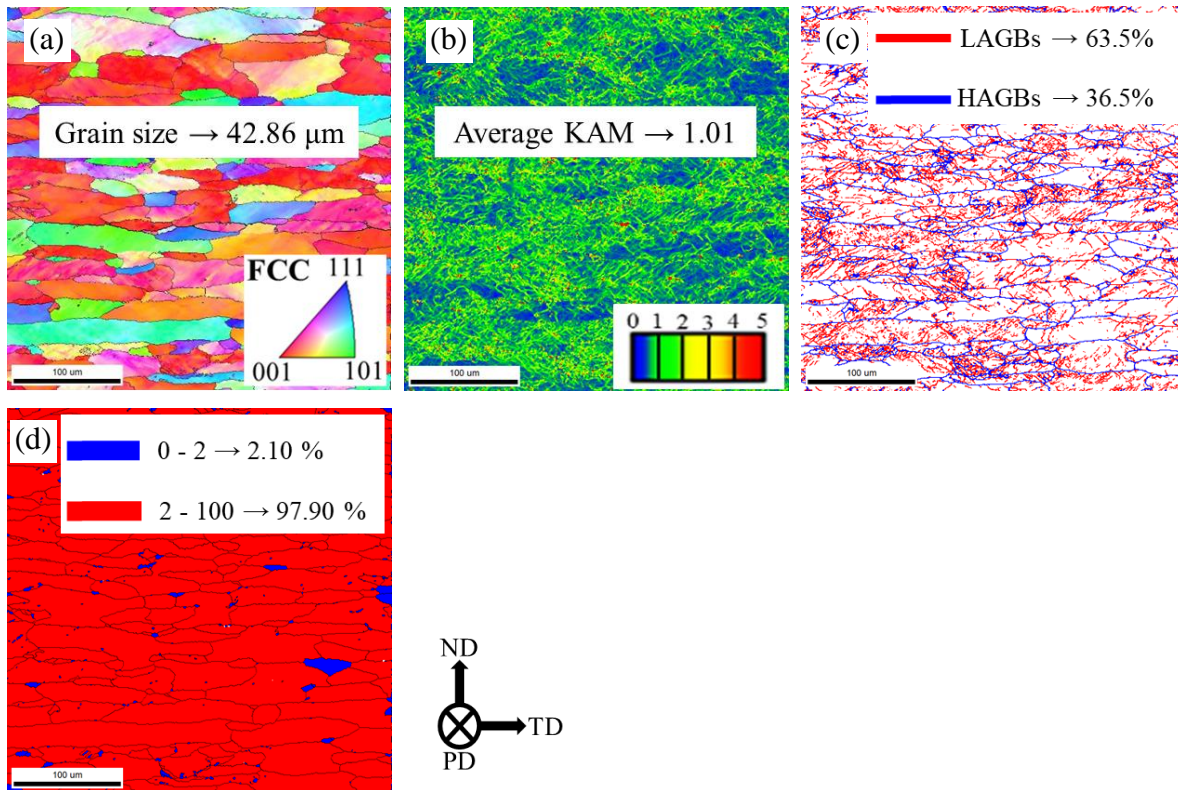


Figure 4.11 Microstructural analysis of AA1050 (BM) (a) IPF map, (b) KAM map, (c) GBCD map, and (d) GOS map, respectively.

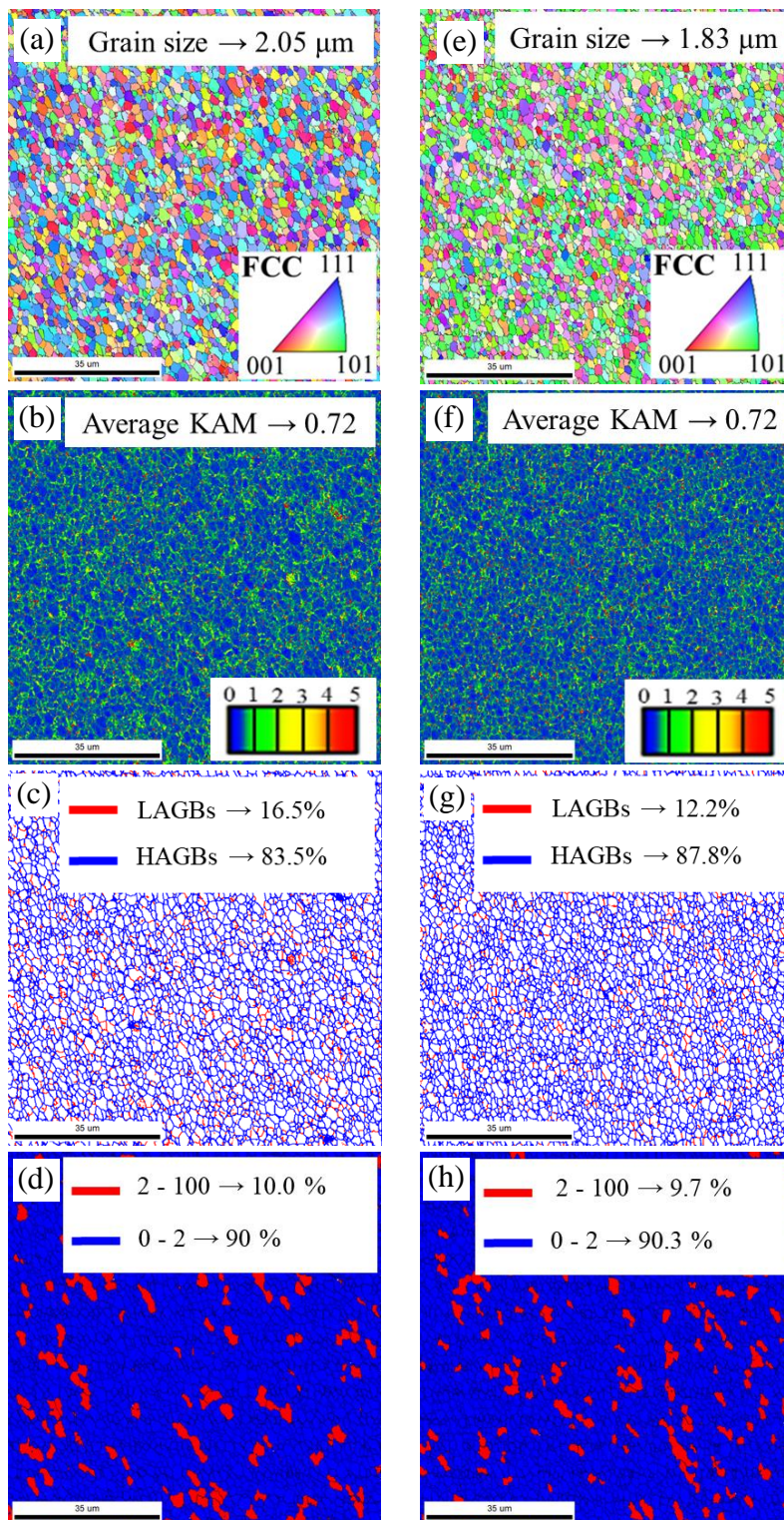


Figure 4.12 EBSD analysis on the SZ AS (S_1); IPF, KAM, GBCD, GOS maps for (a-d) FSP-only and (e-h) FSP with GO conditions.

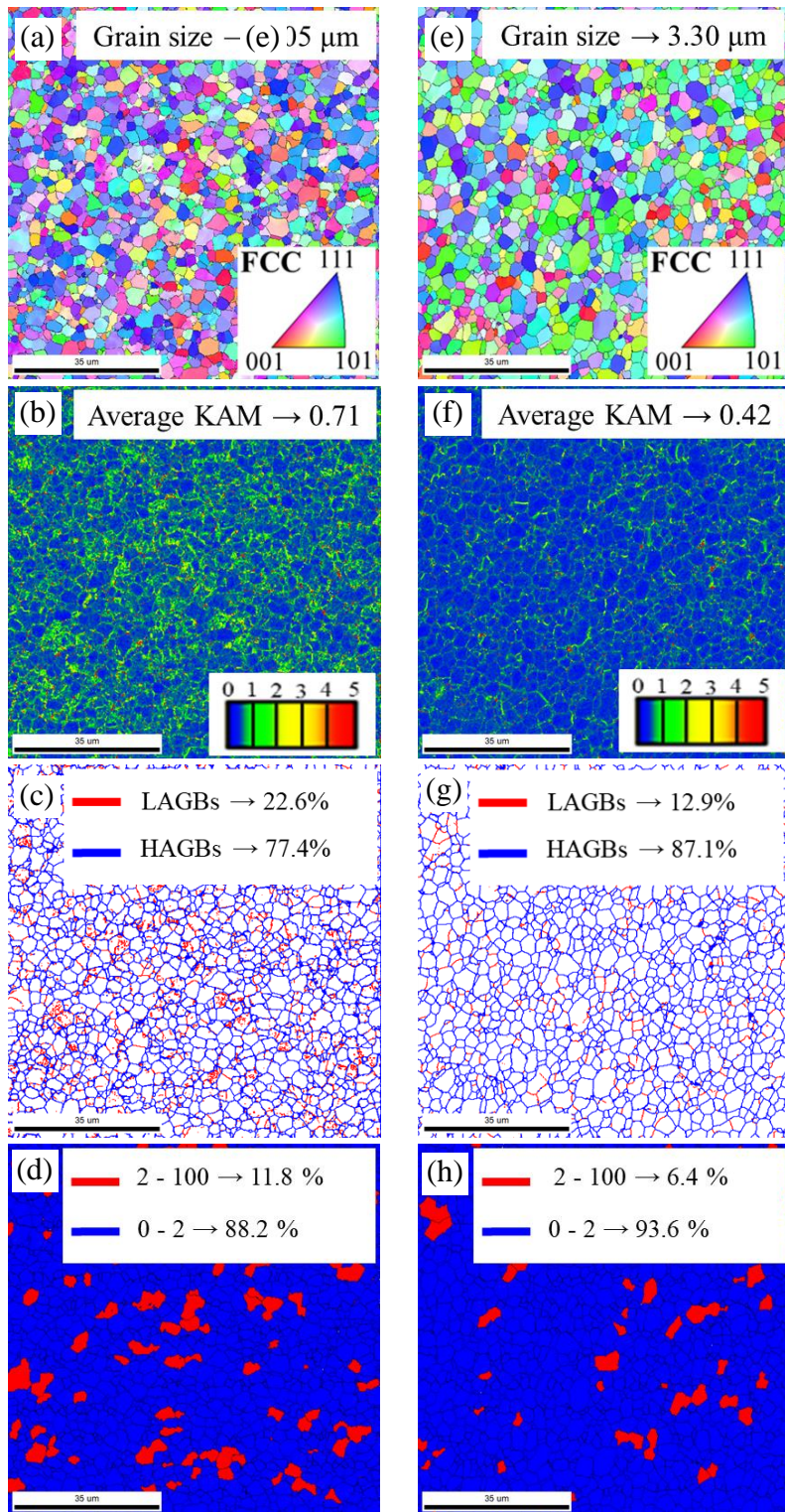


Figure 4.13 EBSD analysis on the RS (S_2) of the SZ; IPF, KAM, GBCD, GOS maps for (a-d) FSP-only and (e-h) FSP with GO conditions.

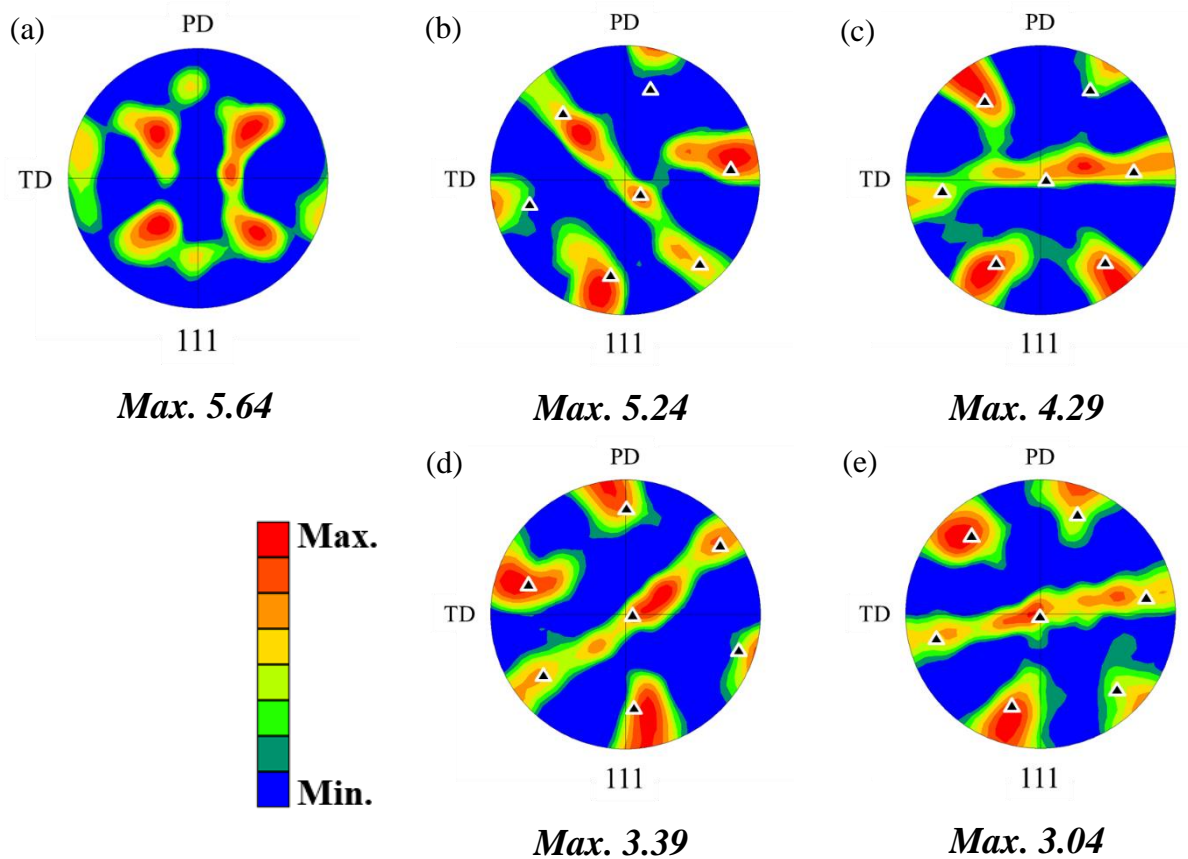


Figure 4.14 Microtexture analysis by {111} pole figures (a) BM; AS (S_1) and RS (S_2) of the SZs of (b, d) only FSP and (c, e) FSP with GO conditions.

4.3.6 Mechanical properties of the fabricated AMC

The surface microhardness mapping on the FSP-only and FSP with GO specimens are shown in Fig. 4.15(a, b). Without GO reinforcement, average microhardness decreased in SZ (32.25 ± 2.08) after FSP compared to BM (34.50 ± 2.75). In contrast, the average microhardness in SZ for FSP with GO (41.50 ± 3.83) condition was higher than both the FSP-only and BM. In Fig. 14(b), the most hardened region (43.00 ± 2.59) was measured on the AS of the SZ (marked with a black dotted line) of FSP with GO specimen. Compared to FSP-only SZ, the top of the SZ of FSP with GO showed a similar range of hardness values with BM.

The tensile test results for the BM, FSP-only, and FSP with GO specimens are shown in Fig. 4.16(a). The tensile test result of the BM shows a distinct yielding peak followed by rapid strain softening with the lowest ductility [30]. Comparatively, both the FSP-only and FSP with GO conditions reveal continuous work-hardening behavior with significant elongations. In addition, the tensile strength and ductility are enhanced in FSP with GO compared to the FSP-only and BM conditions. Conversely, the FSP-only condition reduces tensile strength compared to the BM. The data measured from the tensile test curves are presented in Table 4.3. In addition to an excellent strength-ductility synergy, the manufactured AMC has a significantly improved toughness value compared to the BM. The SEM images of the fracture surfaces of the broken tensile specimen show a typical ductile fracture, as shown in Fig. 4.16(a-c).

Despite the fine-grained structure in the SZ of the FSP-only specimen, the microhardness values were reduced due to lowering strain by dynamic recrystallization. The strain/dislocation, combined with the action of FSP, turns LAGBs into HAGBs [31,32]. Gan et al. [31] also reported a similar trend of hardness distribution after conducting FSP on the commercially available Al alloy. AA1050-H14 is almost pure strain-hardened Al. After FSP, removing strain (or decreasing the strains to compare with BM) is mainly responsible for this hardness drop. In contrast, the improvement in microhardness values for FSP with GO is primarily due to the very fine reinforcing elements in the Al matrix. Moreover, the particle-matrix interaction in the SZ causes direct strengthening along with higher dynamic recovery, which restricts the movement of the strains across the grain boundary by the PSN mechanism. The most-hardened region at AS is attributed to the maximum possible interactions between GO particles and the Al matrix due to higher compressive load and strong material flow due to the nature of the FSP mechanism [12,29].

Table 4.3 Measured data obtained from the tensile curves

Condition	Yield Strength (YS, MPa)	Ultimate Tensile Strength (UTS, MPa)	Elongation (%El)	Toughness (MPa)
BM	30.51± 0.14	94.19 ± 0.91	14.92 ± 0.23	10.49 (± 0.32)
FSP-only	40.62 ± 0.91	93.66 ± 1.49	47.70 ± 1.18	36.29 (± 1.83)
FSP with GO	44.42 ± 0.85	105.72 ± 1.36	53.60 ± 2.21	39.26 (± 0.75)

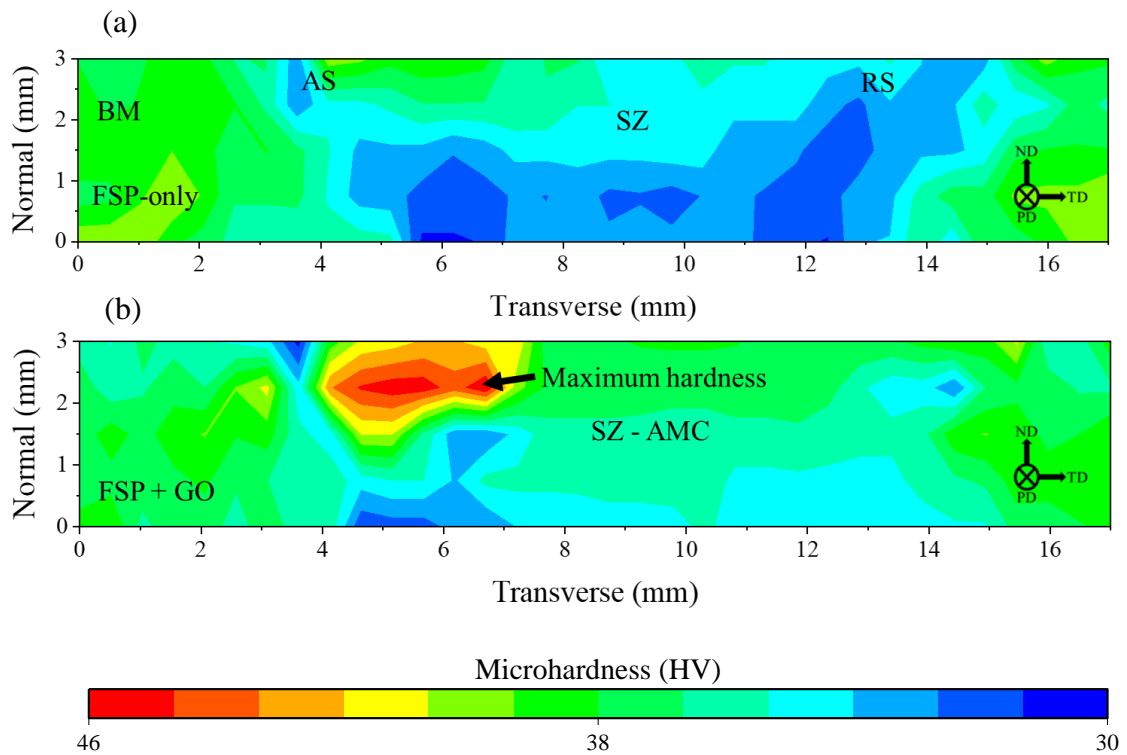


Figure 4.15 Microhardness mapping of (a) FSP-only and (b) FSP with GO conditions.

The above-explained reasons are also related to mechanical strength development for FSP with GO condition over the FSP-only and BM. Besides, the presence of a higher number of grain

boundaries by the preferential amount of dynamic recrystallization for FSP with GO obstructed the transmission of slip and caused the higher strength of the processed AMC [33,34]. In addition, the restricted form of any hard/brittle phase at the particle-matrix interface further developed a significant amount of ductility and toughness inside the manufactured AMC [1-3].

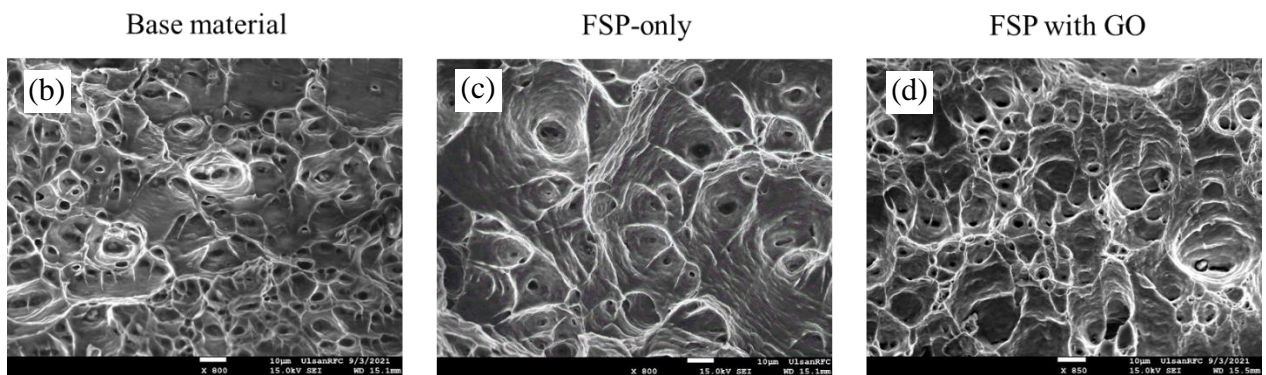
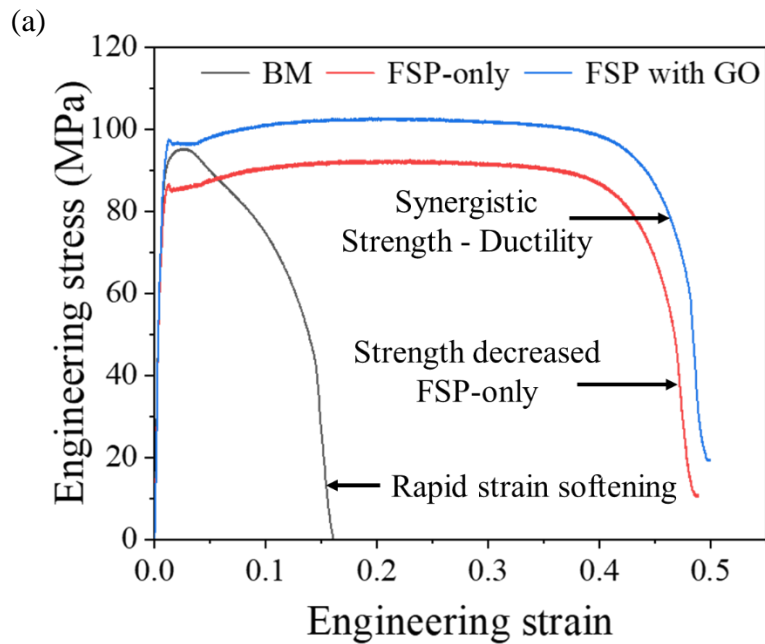


Figure 4.16 (a) Tensile tests curves of BM (in black color), FSP-only (in red color), and FSP with GO (in blue color) specimen merged, (b-d) Fractography of the fractured tensile specimen for BM, FSP-only, and FSP with GO, respectively.

4.4 CONCLUSIONS

FSP, solid-state processing technology, was successfully performed in the fabrication of AMC using GO particle reinforcement. OM image further confirmed no such presence of the defect. Raman spectroscopy results defined the GO (D and G bands) presence in the fabricated AMC. The presence of GO in the Al was specifically found and revealed by SIMS analysis followed by SEM/EDS study. Total ion imaging of C at some depth within the SZ further elucidated that the adhesively attached GO particles came down with the material flow induced by FSP. TEM micrograph and EDS line scanning from a similar site of interest successively revealed no hard/brittle intermetallic compound at the interface between the Al and GO. The microstructure of the fabricated AMC was characterized by the presence of a fine equiaxed grain structure compared to the coarse elongated grain structure of the BM. The surface microhardness map on the cross-section of the fabricated AMC revealed that the most hardened region in SZ for FSP with GO was found at AS. Tensile test results of the fabricated AMC showed a good strength-ductility synergy, as expected from the changes in microstructures of the produced AMC.

REFERENCES

1. F. Khodabakhshi, S.M. Arab, P. Švec, A.P. Gerlich, Fabrication of a new Al-Mg/graphene nanocomposite by multi-pass friction-stir processing: Dispersion, microstructure, stability, and strengthening, *Mater. Charact.* 132 (2017) 92-107.
<https://doi.org/10.1016/j.matchar.2017.08.009>
2. D. Yadav, R. Bauri, Processing, microstructure and mechanical properties of nickel particles embedded aluminium matrix compositemater, *Mater. Sci. Eng. A* 528 (2011) 1326-1333. <https://doi.org/10.1016/j.msea.2010.10.035>
3. S. Dixit, A. Mahata, D.R. Mahapatra, SV Kailas, K. Chattopadhyay, Multi-layer graphene reinforced aluminum – Manufacturing of high strength composite by friction stir alloying, *Compos. Pt. B. Eng.* 136 (2018) 63-71. <https://doi.org/10.1016/j.compositesb.2017.10.028>
4. H. Zhang, B. Zhang, Q. Gao, J. Song, G. Han, A review on microstructures and properties of graphene-reinforced aluminum matrix composites fabricated by friction stir processing, *J. Manuf. Process.* 68 (2021) 126-135. <https://doi.org/10.1016/j.jmapro.2021.07.023>
5. X. Chen, F. Qian, X. Bai, D. Zhao, X. Zhang, J. Li, C. He, C. Shi, J. Tao, N. Zhao, Formation of the orientation relationship-dependent interfacial carbide in Al matrix composite affected by architected carbon nanotube, *Acta Mater.* 228 (2022) 117758.
<https://doi.org/10.1016/j.actamat.2022.117758>
6. S.E. Shin, Y.J. Ko, D.H. Bae, Mechanical and thermal properties of nanocarbon-reinforced aluminum matrix composites at elevated temperatures, *Compos. Pt. B. Eng.* 106 (2016) 66-73. <https://doi.org/10.1016/j.compositesb.2016.09.017>
7. Y. Huang, Y. Su, S. Li, Q. Ouyang, G. Zhang, L. Zhang, D. Zhang, Fabrication of graphite film/aluminum composites by vacuum hot pressing: Process optimization and thermal conductivity, *Compos. Pt. B. Eng.* 107 (2016) 43-50.
<https://doi.org/10.1016/j.compositesb.2016.09.051>
8. Q. Li, J. Wang, H. Wang, X. Zhang, Achieving strong and stable nanocrystalline Al alloys through compositional design, *J. Mater. Res.* 37 (2022) 183–207.
<https://doi.org/10.1557/s43578-021-00363-7>
9. A. Mohammadi, N.A. Enikeev, M.Y. Murashkin, M. Arita, K. Edalati, Examination of inverse Hall-Petch relation in nanostructured aluminum alloys by ultra-severe plastic deformation, *J. Mater. Sci. Technol.* 91 (2021) 78-89.
<https://doi.org/10.1016/j.jmst.2021.01.096>

10. S.Y. Anaman, S. Ansah, H.H. Cho, M.G. Jo, J.Y. Suh, M. Kang, J.S. Lee, S.T. Hong, H.N. Han, An investigation of the microstructural effects on the mechanical and electrochemical properties of a friction stir processed equiatomic CrMnFeCoNi high entropy alloy, *J. Mater. Sci. Technol.* 87 (2021) 60-73. <https://doi.org/10.1016/j.jmst.2021.01.043>
11. A. Sharma, H. Fuji, J. Paul, Influence of reinforcement incorporation approach on mechanical and tribological properties of AA6061- CNT nanocomposite fabricated via FSP, *J. Manuf. Process.* 59 (2020) 604-620. <https://doi.org/10.1016/j.jmapro.2020.10.016>
12. S. Basak, M. Mondal, K. Gao, S.T. Hong, S.Y. Anaman, H.H. Cho, Friction stir butt-welding of roll clad aluminum thin sheets: effect of microstructural and texture changes on mechanical properties, *Mater. Sci. Eng. A* 832 (2022) 142490. <https://doi.org/10.1016/j.msea.2021.142490>
13. R.W. Fonda, J.F. Bingert, Texture variations in aluminium friction stir weld, *Scr. Mater.* 57(11) (2007) 1052-1055. <https://doi.org/10.1016/j.scriptamat.2007.06.068>
14. ASTM E8 / E8M-21, Standard Test Methods for Tension Testing of Metallic Materials, ASTM International, West Conshohocken, PA, 2021. https://doi.org/10.1520/E0008_E0008M-21
15. H. Ijaz, H. Raza, G.A. Gohar, S. Ullah, A. Akhtar, M. Imran, Effect of graphene oxide doped nano coolant on temperature drop across the tube length and effectiveness of car radiator – A CFD study, *Therm. Sci. Eng. Prog.* 20 (2020) 100689. <https://doi.org/10.1016/j.tsep.2020.100689>
16. S. Mo, J. Ye, L. Jia, Y. Chen, Properties and performance of hybrid suspensions of MPCM/nanoparticles for LED thermal management, *Energy* 239 (2022) 122650. <https://doi.org/10.1016/j.energy.2021.122650>
17. F. Ferreira, I. Ferreira, E. Camacho, F. Lopes, A.C. Marques, A. Velhinho, Graphene oxide-reinforced aluminium-matrix nanostructured composites fabricated by accumulative roll bonding, *Compos. Pt. B. Eng.* (164) 2019 265-271. <https://doi.org/10.1016/j.compositesb.2018.11.075>
18. A. Sharma, V.M. Sharma, J. Paul, A comparative study on microstructural evolution and surface properties of graphene/CNT reinforced Al6061–SiC hybrid surface composite fabricated via friction stir processing, *Trans. Nonferrous Met. Soc. China* 29 (2019) 2005-2026. [https://doi.org/10.1016/S1003-6326\(19\)65108-3](https://doi.org/10.1016/S1003-6326(19)65108-3)
19. S. Pahlow, T. Mayerhöfer, M.V.D. Loh, U. Hübner, J. Dellith, K. Weber, J. Popp, Interference-enhanced Raman spectroscopy as a promising tool for the detection of biomolecules on Raman-compatible surfaces, *Anal. Chem.* 90 (2018) 9025–9032.

<https://doi.org/10.1021/acs.analchem.8b01234>

20. Y. Xie, X. Meng, Y. Chang, D. Mao, Z. Qin, L. Wan, Y. Huang, Heteroatom modification enhances corrosion durability in high-mechanical performance graphene-reinforced aluminum matrix composites, *Adv. Sci.* 9 (2022) 2104464.
<https://doi.org/10.1002/advs.202104464>
21. K. Gao, S. Basak, M. Mondal, S. Zhang, S.T. Hong, S.Y. Boakye, H.H. Cho, Friction stir welding of AA3003-clad AA6013 thin sheets: Microstructural changes related to tensile properties and fatigue failure mechanism, *J. Mater. Res. Technol.* 17 (2022) 3221-3233.
<https://doi.org/10.1016/j.jmrt.2022.02.073>
22. J. Chen, G. Zhang, B. Luo, D. Sun, X. Yan, Q. Xue, Surface amorphization and deoxygenation of graphene oxide paper by Ti ion implantation, *Carbon* 49 (2011) 3141-3147. <https://doi.org/10.1016/j.carbon.2011.03.045>
23. G. Compagnini, F. Giannazzo, S. Sonde, V. Raineri, E. Rimini, Ion irradiation and defect formation in single layer graphene, *Carbon* 47 (2009) 3201-3207.
<https://doi.org/10.1016/j.carbon.2009.07.033>
24. M. Mondal, S. Basak, H. Das, S.T. Hong, H. Choi, J.W. Park, H.N. Han, Manufacturing of magnesium/aluminum bimetallic ring components by friction stir assisted simultaneous forging and solid-state joining, *Int. J. Precis Eng Manuf-Green Technol.* 8 (2021) 1429-1438. <https://doi.org/10.1007/s40684-020-00244-0>
25. K. Gao, S. Basak, S. Zhang, S.T. Hong, S.Y. Boakye, H.H. Cho, Effects of the microstructure on the fatigue fracture of friction stir lap welded Al-clad Al and Al-clad steel sheets, *J. Mater. Res. Technol.* 22 (2022) 2518-2531.
<https://doi.org/10.1016/j.jmrt.2022.12.103>
26. A. Sharma, Y. Morisada, H. Fuji, Influence of aluminum-rich intermetallics on microstructure evolution and mechanical properties of friction stir alloyed Al-Fe alloy system, *J. Manuf. Process.* 68 (2021) 668-682.
<https://doi.org/10.1016/j.jmapro.2021.05.073>
27. R. Bauri, D. Yadav, C.N.S. Kumar, B. Balaji, Tungsten particle reinforced Al 5083 composite with high strength and ductility, *Mater. Sci. Eng. A* 620 (2015) 67-75.
<https://doi.org/10.1016/j.msea.2014.09.108>
28. X. Liu, Y. Sun, T. Nagira, K. Ushioda, H. Fuji, Effect of stacking fault energy on the grain structure evolution of FCC metals during friction stir welding, *Acta Metall. Sin. (Engl. Lett.)* 33 (2020) 1001–1012. <https://doi.org/10.1007/s40195-020-01064-6>

29. F. Khodabakhshi, M. Nosko, A.P. Gerlich, Effects of graphene nano-platelets (GNPs) on the microstructural characteristics and textural development of an Al-Mg alloy during friction-stir processing, *Surf. Coat. Technol.* 335 (2018) 288-305.
<https://doi.org/10.1016/j.surfcoat.2017.12.045>
30. B.B. Wang, G.M. Xie, L.H. Wu, P. Xue, D.R. Ni, B.L. Xiao, Y.D. Liu, Z.Y. Ma, Grain size effect on tensile deformation behaviors of pure aluminum, *Mater. Sci. Eng. A* 820 (2021) 141504. <https://doi.org/10.1016/j.msea.2021.141504>
31. W.Y. Gan, Z. Zhou, H. Zhang, T. Peng, Evolution of microstructure and hardness of aluminum after friction stir processing, *Trans. Nonferrous Met. Soc. China* 24 (2014) 975-981. [https://doi.org/10.1016/S1003-6326\(14\)63151-4](https://doi.org/10.1016/S1003-6326(14)63151-4)
32. M.J. Starink, A. Deschamps, S.C. Wang, The strength of friction stir welded and friction stir processed aluminium alloys, *Scr. Mater.* 58 (2008) 377-382.
<https://doi.org/10.1016/j.scriptamat.2007.09.061>
33. P.S. De, R.S. Mishra, Microstructural evolution during fatigue of ultrafine grained aluminum alloy, *Mater. Sci. Eng. A* 527 (2010) 7719 – 7730.
<https://doi.org/10.1016/j.msea.2010.08.047>
34. HJ Aval, S. Serajzadeh, A.H. Kokabi, Evolution of microstructures and mechanical properties in similar and dissimilar friction stir welding of AA5086 and AA6061, *Mater. Sci. Eng. A* 528 (28) (2011) 8071-8083.<https://doi.org/10.1016/j.msea.2011.07.056>

CHAPTER V

SUMMARY AND FUTURE WORKS

5.1 RESEARCH SUMMARY

Friction stir welding was used productively as a solid-state joining and manufacturing technique in various exotic areas of industrial applications. The results conquered from each work recommend FSW as a possible replacement for fusion technologies in modern manufacturing sectors. Simultaneously generated mechanical straining and frictional heat from tool rotation and tool-material interaction in FSW caused dynamically recrystallized fine-grain structures within the joint or fabricated components. Besides, this technology efficiently offered a defect-free processed region, as the temperature in FSW always lay under the melting temperature of substrate materials. Therefore, these characteristics of FSW enhanced the repeatability of efficient fabrication of weld joints, regardless of their critical designs and the advanced grades of structural materials used. The various tool developments also helped FSW to work with almost every possible combination of materials, from light non-ferrous metals to ferrous alloys and other materials. This again demonstrated the extensive practice of FSW and its related technology, such as FSP, in the various critical sectors, including energy, automotive, and aerospace industries.

In Chapter 2, the Al-clad-Al sheets joining was conducted by FSW without any defects. During FSW, there was an intermixing at the AS between the clad and core, but it persisted at RS of SZ. EPMA analysis clarified the diffusion/displacement of Si and its scattered distribution in the SZ. EPMA and SEM-EDS mapping well explained the deformed clad layer and Si particle distribution within SZ. The mechanism behind the precipitation was established, whereby the Si particle diffusion produced various precipitations within SZ. A fine-grained microstructure within

the SZ appeared due to adequate heat generation and substantial plastic deformation during FSW. The measured microhardness and joint strength were found to be developed. The summary of Chapter 2 is photographically represented in Fig. 5.1.

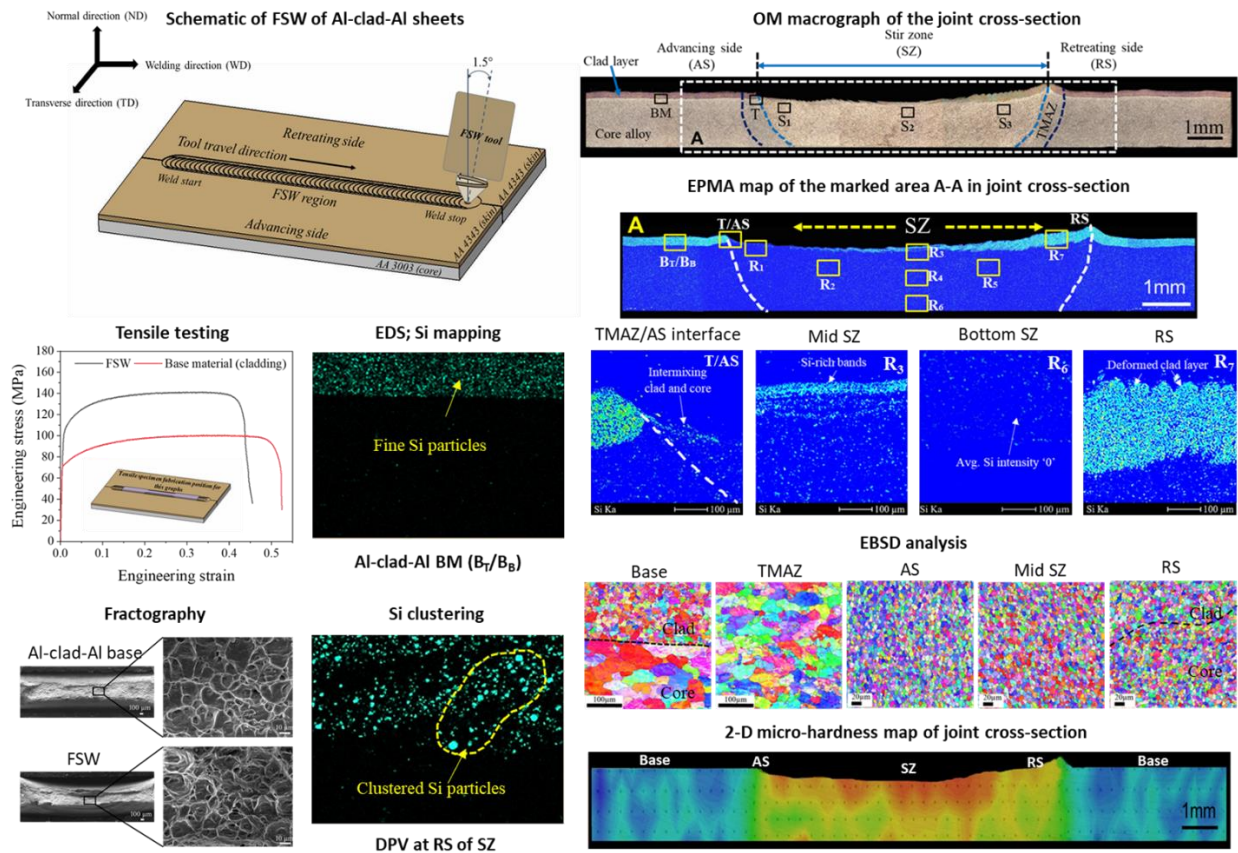


Figure 5.1 Photographic representation of the summary of Chapter 2.

Chapter 3 demonstrated the feasibility of gas-pocket-assisted underwater friction stir solid-state welding (GAFSSW) as a newly developed UWW technique. The gas pocket stability was controlled using the adapter attached to the region of operation on the workpiece and a constant inert gas (Ar) flow. Furthermore, the microstructural changes related to the development of mechanical properties of the GAFSSW were studied and compared with UFSSW and FSSW in

the air. The research findings were aligned with the perspective of developing FSW as an efficient UWW technique. The challenges of diverting seawater from the weld area and fusion defects were addressed with the developed GAFSSW technique. The summary of Chapter 2 is photographically represented in Fig. 5.1.

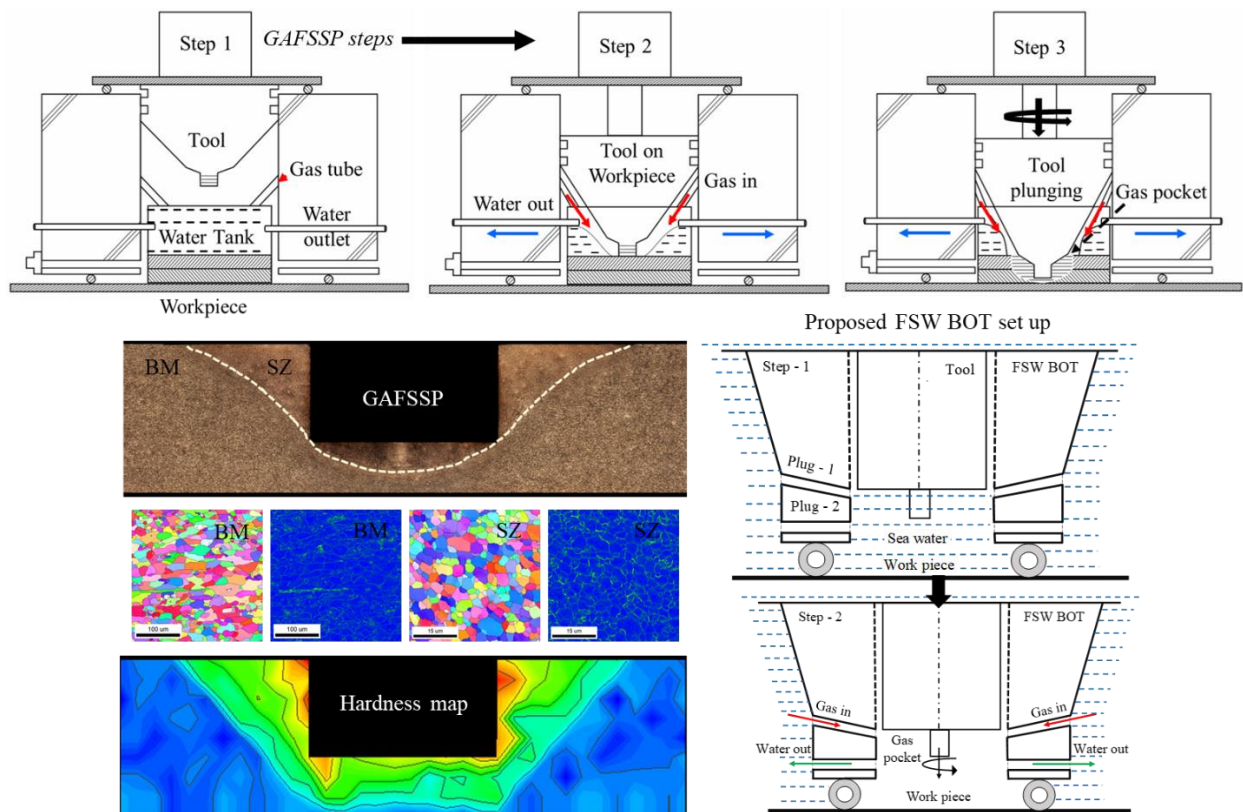


Figure 5.2 Photographic representation of the summary of Chapter 3.

Chapter 4 examined the effect of GO on the microstructure and mechanical properties of AMC fabricated by single-pass FSP. The Raman spectroscopy and SIMS analyses successfully confirmed the survivability of GO particles inside the Al. Furthermore, the morphology of the GO-

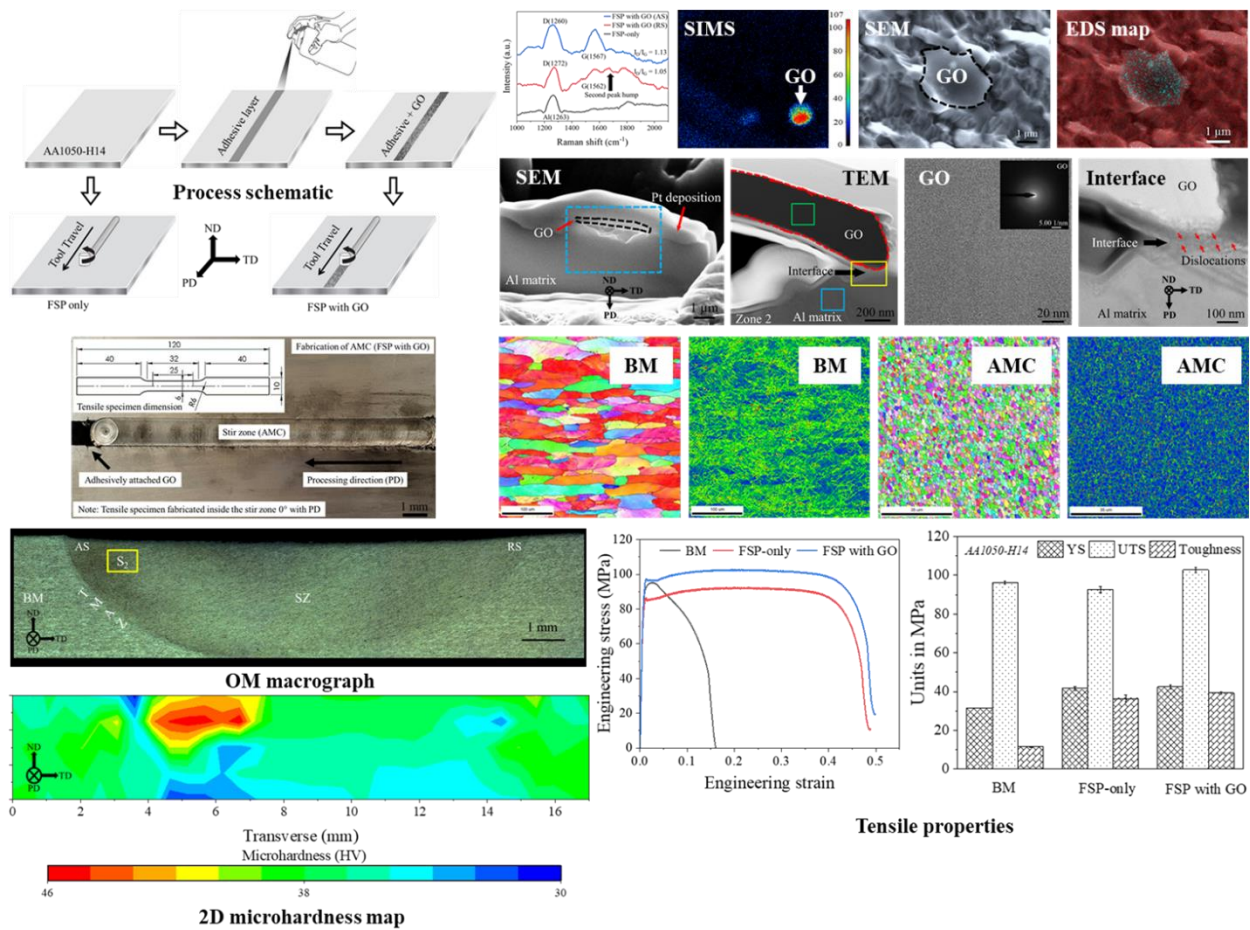


Figure 5.3 Photographic representation of the summary of Chapter 4.

-particles was changed and turned into nano-flakes during FSP and bonded with the Al matrix, as confirmed by TEM analysis. EBSD microstructural analysis revealed a significant grain refinement for the fabricated AMC. Also, the advancing side (AS) of the FSP with GO specimen showed more refined grain structures than the retreating side (RS) of the SZ. Furthermore, significant increases of high angle grain boundaries and lower kernel average misorientation revealed the occurrence of dynamic recrystallization caused by FSP. The advancement of mechanical properties was found primarily due to GO particles and their interaction with the pure Al matrix. The strength and ductility were improved in the fabricated AMC compared to the BM.

Besides, the microhardness map of FSP with GO indicated an overall improved hardness value and showed the maximum hardness zone at the AS of the SZ of the processed AMC.

5.2 FUTURE WORK

This thesis presents the new application possibilities of the solid-state FSW technology apart from its typical joining applications by changing different material combinations. The process can be applied more efficiently, and ways to conduct future work on individual chapters are given below:

- Regarding clad materials joining, FSW could be carried out in various configurations, including spot welding. The performance of the joint can be evaluated with fatigue testing concerning the measured tensile properties in this work. Also, analysis of corrosion properties can be another research direction, where mixing clad and core of different materials can provide higher corrosion resistance than their base material properties.
- The ability to perform GAFSSW is indicated in this research. But, this technology needs to be executed in a linear joining of the materials. This will offer the possibility to perform an in-depth analysis of the joint mechanical properties regarding the microstructural changes achieved. In addition, a study of the fretting wear behavior of the joint surface can be considered for future research in GAFSSW.
- A more detailed TEM analysis can be done for AMC as future work of this research. In addition, performing temperature variable fatigue tests and detailed studies on corrosion properties, including stress corrosion cracking and how the crack path moderates during passage through the reinforcement particles, can be considered a future perspective of this work.